Contents

1 Introduction **1**

2 Executive Summary **3**
2.1 Overview 3
2.2 Scientific goals 3
2.3 Beam 5
2.4 Detector 5
2.5 Civil construction 6
2.6 Rates, trigger and DAQ 7
2.7 Other considerations 7

3 Scientific Goals **9**
3.1 Introduction 9
3.1.1 QCD mesons and confinement 9
3.1.2 Conventional and non-conventional mesons 10
3.1.3 Photoproduction of mesons 12
3.2 Theoretical considerations 13
3.2.1 Overview 13
3.2.2 Forms of confinement : gluons and confinement 14
3.2.3 Phenomenology and confinement 15
3.2.4 Conventional light quark mesons - theory 16
3.2.5 Glueballs - theory 17
3.2.6 Hybrids - theory 18
3.2.7 Multiquark systems - theory 20
3.2.8 $s\bar{s}$ states - theory 20
3.3 Physics with ϕ mesons 23
3.3.1 S/P interferometry 24
3.3.2 Rare decays 25
3.3.3 Future plans 27

4 Photon Beam **29**
4.1 Choice of technique . . . 29
4.2 Energy requirements . . . 30
4.3 Polarization requirements . . . 34
4.4 Compton backscattered beams . . . 36
4.5 Bremsstrahlung beams . . . 38
4.6 Photon Source . . . 41
4.6.1 Use of collimation . . . 44
4.6.2 Choice of radiator . . . 48
4.6.3 Crystal thickness . . . 50
4.6.4 Crystal mount . . . 52
4.6.5 Crystal quality and lifetime . . . 53
4.7 Electron Beam Line . . . 53
4.7.1 Beam emittance requirements . . . 54
4.7.2 Electron beam line optics . . . 56
4.7.3 Electron beam dump . . . 57
4.7.4 Possibility of hadron beams . . . 58
4.8 Tagging Spectrometer . . . 59
4.8.1 Magnet . . . 59
4.8.2 Focal-plane hodoscope . . . 60

5 The Detector **63**
5.1 Overview . . . 63
5.2 The solenoid region . . . 65
5.2.1 Superconducting solenoid . . . 65
5.2.2 Target . . . 67
5.2.3 Start counter . . . 67
5.2.4 Cylindrical tracking chambers . . . 68
5.2.5 Barrel calorimeter . . . 68
5.2.6 Forward tracking system . . . 68
5.3 The forward region . . . 69
5.3.1 Forward tracking system . . . 69
5.3.2 Čerenkov counter . . . 69
5.3.3 Forward calorimeter . . . 70
5.4 Barrel calorimetry . . . 70
5.4.1 Design considerations . . . 71
5.4.2 Pb/SciFi barrel calorimeter . . . 71
5.4.3 Crystal options . . . 74
5.5 Tracking chambers . . . 75
5.5.1 Central drift chamber . . . 83

5.5.2 Central vertex chamber 83
5.5.3 Forward drift chambers 84
5.5.4 The beam vertex trackers 85
5.5.5 Electronics 85
5.6 Particle identification 86
5.6.1 Introduction 86
5.6.2 Event simulation 86
5.6.3 PID for forward particles ($\theta \leq 14.5°$) 88
5.6.4 PID for particles within the solenoid ($\theta \geq 14.5°$) 91
5.7 Forward calorimetry 92
5.7.1 Performance 93
5.7.2 Mechanical description 95
5.7.3 Radphi experience 99

6 Civil Construction **103**
6.1 Site Work 103
6.2 HALL D 104
6.3 Tagger Building 105
6.4 Control Room 106
6.5 Service building 106
6.6 Beam Dump 107
6.7 Concrete tunnel 107
6.8 Permissible Settlements 108
6.9 Beam Pipe 108
6.10 LCW System and Cooling water Tower 108
6.11 Power Requirement 108
6.12 Communication Conduits 108
6.13 Items not Included Here 109
6.14 Environmental and Radiation Concerns 109

7 Rates, Trigger and Data Acquisition **113**
7.1 Expected Rates 113
7.1.1 Overview 113
7.1.2 Trigger Elements 114
7.1.3 Accidental Rates 115
7.2 HALL D Trigger 117
7.2.1 Overview 117
7.2.2 Level 1 Trigger 119
7.3 Data Acquisition 120
7.3.1 Hardware, Data Volume, and Readout 121

7.3.2 Data Transport, Event Building and Archiving 122
7.3.3 Monitoring and Control 123

8 Data handling plan **125**

9 Monte Carlo simulations **127**
9.1 Introduction 127
9.2 Monte Carlo Framework 127

10 Data Analysis **131**
10.1 Introduction 131
10.2 Beam and final state normalizations 132
10.2.1 Photon beam flux 133
10.2.2 Particle detection efficiency and acceptance 134
10.3 The Role of photon linear polarization 135
10.4 Description of the partial wave analysis 137
10.4.1 General description 137
10.4.2 Decay amplitudes 139
10.4.3 Initial state polarization 140
10.4.4 Joint production of excited baryons and mesons 140

11 Milestones **143**

12 Costs **145**

13 Management plan **151**

Chapter 1

Introduction

This is a Preliminary Design Report from the HALL D collaboration to build a 4π hermetic detector with the purpose of studying the photoproduction of unusual mesons and gluonic excitations at Jefferson Lab. This HALL D project also includes a beamline and an above-ground tagger building and detector building to be located off the stub at the east end of the north linac of the CEBAF accelerator. This project assumes that the energy of CEBAF will be increased to 12 GeV by the early part of the next decade.

These plans have evolved over the last 18 months, starting with a workshop held in July, 1997 at Indiana University and the formation of a working group (HALL D collaboration or *Eightplus* working group). There then followed workshops at North Carolina State University (November, 1997), Carnegie Mellon University (March, 1998) and at Florida State University (October, 1998). The Jefferson Lab Users Community was given a status report at the Users Workshop in June, 1998. Another workshop is planned for March, 1999 at Rensselaer Polytechnic Institute during which parts of this Design Report will be expanded on. During 1998, there also were several meetings involving principals of the Hall D collaboration with the management, accelerator division and personnel from the civil construction group. Negotiations with Los Alamos National Lab and Fermilab indicate that we will be able to transfer the MEGA superconducting solenoid (also used in the LASS spectrometer at SLAC) and a dipole magnet to Jefferson Lab for use in the proposed detector. It is the expectation and hope of the HALL D collaboration that this Preliminary Design Report will be updated and expanded in the coming months and that this project will be formally reviewed by mid-1999. The HALL D collaboration activities and workshops are summarized here:

http : //dustbunny.physics.indiana.edu/ $\sim$ dzierba/Eightplus/.

Chapter 2

Executive Summary

2.1 Overview

This Preliminary Design Report describes a plan to build a hermetic 4π detector to search for unusual mesons and gluonic excitations in photon induced reactions. In order to photoproduce the desired states over the mass range of interest ($< c\bar{c}$ threshold or < 3 GeV/c^2) requires an incident photon beam of 12 GeV . The plan further calls for a new beamline at Jefferson Lab with a photon tagger and a new experimental building (HALL D) to house this detetector. The tagger building and the proposed HALL D will be above ground and the beamline will come off the stub located at the east end of the north linac. All this assumes the planned energy upgrade for the CEBAF accelerator.

This Preliminary Design Report is submitted by a collaboration of over 60 physicists from 19 institutions. This collaboration will grow as the plans for the HALL D project mature. A key feature of this collaboration is the close and explicit cooperation of theorists and experimentalists to define the goals within the context of the progress of the field of light quark spectroscopy on theoretical, phenomenological and experimental fronts and to develop and refine analysis techniques, especially with regard to extracting information on the quantum numbers of observed mesons.

This chapter provides an overview and summary of what appears in this Design Report.

2.2 Scientific goals

That QCD mesons outside the naive quark model ($q\bar{q}$) have been found is an experimental certainty. The light quark meson spectrum (below charm

threshold) has more states than can be accommodated within the $q\bar{q}$ model. Furthermore, there seems to be evidence for at least one glueball state and at least one state with so-called exotic J^{PC} quantum numbers, that is, quantum numbers which cannot be formed in a $q\bar{q}$ system. In parallel, lattice gauge calculations and QCD-inspired models (e.g. flux-tube model, bag model) are starting to converge on the prediction of the masses of unconventional mesons.

The challenge for theorists and experimentalists in the next decade will be to carefully map out the spectrum of these gluonic excitations and the $q\bar{q}$ mesons with which they mix, gathering information about their quantum numbers and their decay modes, and using this to gain an understanding of mesonic structure and the low energy degrees of freedom of QCD. The ultimate goal is insight into the nature of confinement in QCD.

During the next few years, analysis of data already gathered in hadron-induced fixed target experiments, in $\bar{p}p$ annihilations, e^+e^- and $\gamma\gamma$ collisions, and decays of the J/ψ, Υ and Z° will add to our knowledge base. However, in order to make the next significant addition to our storehouse of experimental information, we must gather high-quality and high-statistics data using the photon as a probe. For technical reasons, there is a dearth of data on the photoproduction of meson states below charm threshold. Photon beams of unprecedented quality (intensity, size, resolution and duty factor) are now available at Jefferson Lab. With an energy upgrade of CEBAF to 12 GeV and with the construction of a beamline and hermetic 4π detector, we can expect to add rich new information on the spectrum of gluonic excitations.

The photon is distinct from hadronic probes (π or K) which have been used to date. In contrast to the $q\bar{q}$ system of the π or K, with quark spins anti-aligned, the photon is a virtual vector meson, a $q\bar{q}$ system with quark spins aligned. Within the flux tube model, before the interaction, this spin-1 $q\bar{q}$ has its flux tube in the ground state. After interaction with the target, the flux tube can be excited to its first excited state giving rise to states which include those with exotic J^{PC} : 0^{+-}, 1^{-+} and 2^{+-}. Since the photon can also be viewed as an $s\bar{s}$ system, photoproduction will also yield important new information on $s\bar{s}$ spectroscopy. The $s\bar{s}$ nature of the photon at the energies of the proposed upgrade is also relevant to providing the bridge between the light quark (u and d) sector and the heavy quark (c and b) sector. Another important aspect of the nature of the photon beam is polarization, which will be used as an important new tool for identifying gluonic excitations.

The vector photon is very efficient at producing massive vectors, ρ, ω and ϕ via diffractive scattering with relatively high cross sections in the forward direction. We can view CEBAF as a factory for these mesons to study their rare decays. Of particular interest is the ϕ meson, whose decays are relevant

for studies of the nature of the mesons into which the ϕ can radiatively decay. The boost of these ϕ's in the lab frame offers some important advantages over producing them at rest. The advantages this boost might offer in exploring the physics of the ϕ as a source of correlated $K_L K_S$ (CP and/or CPT studies) are also being investigated.

2.3 Beam

The goal of the HALL D project is the investigation of the meson spectrum up to masses of approximately 3 GeV/c^2. The requirement that we observe states up to this mass limit with sufficient boost so that their decay products can be observed with excellent acceptance and resolution implies that the photon beam energy be at least 12 GeV.

Three major methods have been considered for producing photons of the highest possible energy, flux and polarization from electrons in the energy range 8-12 GeV. The methods are ordinary bremsstrahlung, coherent bremsstrahlung and Compton backscattering of light. None of the methods are new and calculation of the basic cross sections that underlie them are presented in most textbooks on applications of QED.

Each of these techniques has its own limitations and advantages. This, taken together with the requirements of the experimental program determine the method used to generate the photon beam. The experimental requirements imposed on the HALL D project are sufficient energy, flux and linear polarization. The Compton backscattered technique has the virtue of cleanliness and high degree of linear polarization. However, even using the best available mirrors and with technically challenging beam focusing, the photon energy is limited to 30% of the endpoint energy. Frequency doubling the laser only achieves 50% of the endpoint energy. Ordinary bremsstrahlung has no flux limitations and the photon energies up to 95% of the endpoint can be achieved. However no linear polarization is available. The coherent bremsstrahlung technique is clearly the best choice to satisfy the requirements of the experimental program since it provides enhanced flux at desired energies and makes possible linearly polarized photons.

2.4 Detector

The physics goals of the HALL D project require a full partial wave analysis of kinematically identified exclusive reactions producing mesons. The decay

products of produced mesons must be identified and measured with good resolution and with full acceptance in decay angles. In many cases, the decays of mesons involve a chain of particle decays. The HALL D detector must therefore be hermetic with 4π coverage with the capability of measuring energies of neutral particles (γ, π^0, η) and momenta of charged particles with good resolution. Particle identification is also required.

The HALL D detector will be built in two stages. The STAGE 1 detector will be used with incident photons in the energy range from 6 to 8 GeV - assuming that HALL D and the beamline are in place before the 12 GeV energy upgrade.

The STAGE 1 detector will consist of a large aperture superconducting solenoid filled with a target, tracking chambers and calorimetry. The calorimetry will also provide time-of-flight information for particle identification. The solenoid will be followed with a threshold Čerenkov counter, particle tracking and a lead glass electromagnetic calorimeter.

The STAGE 2 HALL D detector will likely have the same *solenoid region* since the kinematics of the particles produced as part of the recoil system does not change appreciably with the increased beam energy. However, in STAGE 2 the forward particles will have higher energies and momenta requiring a modification of the *forward region*. A dipole magnet will be added with more forward tracking. The forward calorimetry will also need modification.

The superconducting solenoidal magnet is the LASS/MEGA magnet. This magnet was built for the Large Aperture Superconducting Solenoid Spectrometer (LASS) and SLAC and later transferred to LANL for use in the MEGA experiment. It will be transferred to Jefferson Lab for use in HALL D . A dipole magnet used in the tagged photon laboratory at Fermilab will be transferred to Jefferson Lab for the STAGE 2 detector. The STAGE 1 electromagnetic calorimeter is the 3000-element detector used in E852 at Brookhaven Lab.

2.5 Civil construction

The plan is to site the meson spectrometer in a new experiment hall (HALL D) to be located at the end of the HALL D beamline which would come off the stub at the east end of the North Linac. The civil construction includes work associated with breaking through the stub, delivering beam above ground to a tagger, a tagger building, HALL D, the counting house, roads, and a parking area. Members of the HALL D collaboration have been meeting with members the JLab civil construction team to arrive at a cost estimate for civil construction sometime in February, 1999.

2.6 Rates, trigger and DAQ

Initially the HALL D detector will run with tagged photon fluxes of 10^7 photons/sec which leads to a tagged hadronic rate of 5 KHz. Estimates of the hadronic and electromagnetic tagged and untagged rates have been made along with estimates of accidental rates. These rate estimate calculations are backed by measurements made in Hall B and do not present a technical challenge for the HALL D detectors and electronics.

With photon fluxes of 10^7 photons/sec, current statistics on light quark meson production collected in hadron experiments will be exceeded by two orders of magnitude in the first 1-2 years of HALL D running.

The trigger system will be designed from the outset in a pipeline fashion to provide maximum flexibility for sophisticated triggers. This will allow us to gradually increase the incident flux to 10^8 photons/sec – greatly opening the scope of physics, in meson spectroscopy and rare decays.

The proposed DAQ system is based on an upgrade of the exisiting DAQ system already in use at Jefferson Lab.

2.7 Other considerations

In the coming months, the HALL D collaboration will work with JLab management, the accelerator division and the civil construction group to develop a realistic cost estimate, timeline, and collaboration management plan. All this is needed for the WBS for this project. The next version of this Design Report should be completed by May, 1999.

Chapter 3

Scientific Goals

3.1 Introduction

The scientific goal of the HALL D project is a high-statistics study of the photoproduction of mesons, with masses below $c\bar{c}$ threshold, using a hermetic 4π detector with sensitivity to a wide variety of decay modes of these mesons. Photoproduction of these light mesons is expected to yield important new information on the spectrum of mesons beyond the naive $q\bar{q}$ model. The discussion below will show how this study impacts on our understanding of Quantum Chromodynamics (QCD), especially on the issue of *confinement*. The HALL D spectrometer also has the potential for the study of physics associated with the high statistics production of the light vector mesons: ρ, ω and ϕ. This physics includes rare decays and symmetry tests.

3.1.1 QCD mesons and confinement

QCD is the *standard* theory of quarks and gluons which has successfully met experimental tests in the perturbative regime where calculational techniques have made possible comparison with collider experiments and fixed-target experiments at high energy and high Q^2. The same situation does not hold in the non-perturbative regime – but important progress is being made on both theoretical and experimental fronts. The comparison between theory and experiment, in this non-perturbative regime, will lead to an understanding of *confinement*, which along with *asymptotic freedom*, gives QCD its distinct character. The focus of much of this recent progress is in the understanding of the spectrum of mesons. Theoretical advancement is being made on two fronts, lattice gauge theories (LGT) and QCD-inspired models, resulting in a prediction of the spectrum of mesons and their decays. Information to date coming

from experiments with incident π and K beams, from $\bar{p}p$ annihilations, e^+e^- collisions and J/ψ, Υ, τ and Z^o decays has indicated that the meson spectrum is rich indeed but our information is incomplete. High statistics data on the photoproduction of mesons is needed to complete the picture.

Within QCD, the spectrum of light mesons includes not only the *conventional* mesons of the naive $q\bar{q}$ model, but of other mesons as well, including (1) *glueballs* – states of pure glue with no quark content (gg or ggg), (2) *hybrids* – which carry valence glue in addition to quarks ($q\bar{q}g$) and (3) *molecular* or *four quark* states – which include, for example, $K\bar{K}$ or $\rho\rho$ molecules and combinations of diquark and anti-diquark ($q\bar{q}q\bar{q}$). We collectively refer to categories (1) and (2) above as *gluonic mesons*. Within the *flux tube* model, mesons of category (2) are referred to as *gluonic excitations*. In this model, the q and $\bar{q}$ are bound by a flux tube. Conventional $q\bar{q}$ mesons correspond to the flux tube being in the ground states whereas for hybrid mesons the flux tube is in an excited state. Figure 3.1 shows a level diagram giving the range of masses for the conventional $q\bar{q}$ nonets and estimates of the mass range for glueballs, hybrids and thresholds for molecular states.

There are a number of excellent reviews of light quark mesons. Two of the more recent reviews [1, 2] also give references to earlier reviews.

3.1.2 Conventional and non-conventional mesons

Conventional $q\bar{q}$ mesons, made of u, d and s quarks are grouped in nonets, each characterized by a given J^{PC}. The rules for allowed values of J^{PC} follow from the requirements of a fermion-antifermion system: the quark spins can be parallel ($S = 1$) or antiparallel ($S = 0$) with relative orbital angular momentum (L), $\vec{J} = \vec{L} + \vec{S}$, $P = (-1)^{L+1}$ and $C = (-1)^{L+S}$. For a $q\bar{q}$ meson, $J^{PC} = 0^{+-}$, 0^{--}, 1^{-+}, 2^{+-}, ... are not allowed and are referred to as *exotic* quantum numbers. These restrictions do not apply to gluonic mesons. In addition to the ground state nonets, radial excitations are expected and observed as well. Association of observed meson states with particular $q\bar{q}$ states within a nonet often depends on a good understanding of the various decay modes of the meson as well as its production characteristics.

It is now clear that the observed meson spectrum includes states which cannot be accomodated within the naive quark model. For example, there are at least five scalar states reported with masses below 2 GeV/c^2 suggesting that among these may be a glueball. LGT calculations indicate that the lightest salar glueball should have a mass in the range from 1.5 to 1.7 GeV/c^2. There is also strong evidence that at least one exotic hybrid has been observed as well as possible evidence for molecular states.

Figure 3.1: A level diagram showing conventional nonets and expected masses of glueballs, hybrids and molecular thresholds.

3.1.3 Photoproduction of mesons

Photon beams at Jefferson Lab are and will be of unprecedented quality with regard to intensity, emittance and duty factor. New physics will be uncovered starting with initial photon energies of about 6 GeV, culminating in energies of 12 GeV, which will allow examination of the meson spectrum up to masses of ≈ 3 GeV/c^2.

Production of mesons using beams of photons is expected to add much to our knowledge of light quark mesons. For reasons which are partly technical and partly historical, there is little known about the photoproduction of light mesons. In contrast, there is a wealth of data from fixed target experiments using π and K beams and from $\bar{p}p$ annihilations. Experience has shown that information from new probes has led to an increased understanding of the meson spectrum and that is expected to especially true of the photon.

The photon is a very different probe compared to the π or K. The quark content of these pseudoscalar beams consists of a q and $\bar{q}$ with spins antiparallel ($S = 0$) whereas the photon, via vector dominance, can be viewed as a vector $q\bar{q}$ with spins aligned ($S = 1$). Within the flux tube picture, the incident probe has spins aligned with the flux tube in its ground state. After scattering, if the flux tube is excited to its first excited state, with quark spins still aligned, the resulting system can have $J^{PC} = 0^{-+}$, 1^{+-}, 2^{-+} or $J^{PC} = 0^{+-}$, 1^{-+}, 2^{+-} – the latter three possibilities are exotic combinations of J^{PC}. Since the photon can also viewed as a virtual $s\bar{s}$ system, the photon can be expected to be a rich probe for production of meson states with an $s\bar{s}$ component. The identification of $s\bar{s}$ members of the nonets has been and will be important in assignment of mesons to the nonets. The $s\bar{s}$ nature of the photon provides us with an important bridge between the very light quark sector of u and d quarks and the heavy quark sector starting with the c quark. Finally, photon polarization will be a powerful tool in the spin analysis of the produced meson systems and may lead to an additional method for distinguishing hybrid states from conventional mesons.

Meson photoproduction proceeds by three dominant mechanisms, diffraction, t- channel exchange, and s-channel baryon production. The first two are the most interesting for our purposes, and it is useful to distinguish these because they can be separated to a large extent kinematically, and in some reactions they populate different meson sectors.

At the highest energies, the dominant mechanism of meson photoproduction is vector dominance, followed by diffraction. The incident photon converts directly into a 1^{--} vector meson, which then undergoes diffractive scattering off the nucleon target. The intermediate vectors $\rho : \phi : \omega$ are theoretically

produced in the intensity ratios 9:2:1, due to their flavor factors. Although diffractive scattering is poorly understood in terms of elementary QCD interactions, it is well known that it can be treated as vacuum quantum number exchange in t-channel. This leads to the production of $C = -$ neutral hadronic states with all possible J^P. Since the nature of the pomeron is not well understood, it is difficult to anticipate which $C = -$ states will be produced with large amplitudes, and what the relative amplitudes will be. Indeed, a systematic survey of the diffractive photoproduction amplitudes may give us interesting new information about the nature of the pomeron.

At lower energies, nondiffractive mechanisms with nonvacuum t-channel exchanges become important and even dominant. One π exchange is especially interesting, because it can be isolated by cuts in t and by choice of final state flavor, and this provides a filter for $G = -$ and (for neutrals) $C = -$ states. Since the couplings of quarkonia to $\rho\pi$ have been calculated in detail in the $^3P_0$ model [3] we have an expected list of states such as $\omega_3(1667)$, $\pi_2(1670)$ and $\omega_1(1649)$ that should be clearly evident in one π exchange photoproduction. A systematic survey of the same states in the other allowed two-body modes would be extremely useful as a test of the $^3P_0$ decay model, and should also indicate which states do not decay as expected were they $q\bar{q}$.

3.2 Theoretical considerations

3.2.1 Overview

Understanding the low energy aspects of QCD remains as one of the most important goals for the intermediate energy physics in the turn of the millennium. At low energies, QCD describes a relativistic, many body system of strongly interacting quarks and gluons. The two fundamental features of QCD whose dynamic origin remain to be resolved are, the dominance of weakly interacting light quasiparticles which is a consequence of spontaneous chiral symmetry breaking and the phenomenon of quark confinement. It is believed that confinement and chiral symmetry breaking are related, for example, the chiral phase transition and 'deconfinement' occur at the same temperature in lattice gauge theory simulations.

The loss of chiral symmetry is signaled by the absence of parity-degenerate multiplets in the hadron spectrum and by the presence of low-lying pseudo Goldstone bosons. Confinement precludes the existence of isolated color charges and it is tied to the underlying local color-gauge invariance of the theory. Confinement is thus believed to arise from nonlinear gluodynamics which causes

chromoelectric field to collapse into a 'flux tube' whose linearly rising energy density forces quarks and gluons to remain in color singlet states. Similarly, spontaneous chiral symmetry breaking can be generated dynamically by letting quarks propagate in a vacuum, which is non-trivial due to a condensate of $q\bar{q}$ pairs. It is therefore clear that both of these properties of QCD are ultimately driven by the dynamics of soft gluons and a thorough study of low energy gluodynamics provides the only hope for understanding the phenomena of chiral symmetry breaking and confinement.

Learning about how glue behaves at low energy will require the collection and assimilation of a large body of spectroscopic and dynamical information. It is only through this process that we can hope hope to address such basic issues as what the effective degrees of freedom are which best describe glue at low energy.

3.2.2 Forms of confinement : gluons and confinement

Eliminating quark degrees of freedom in principle allow to focus on gluon dynamics. To date the main source of information about confinement are the phenomenology and lattice analysis of heavy (static) quark systems. However the light quark systems are particularly useful for studies of soft QCD. The enormous success of the quark model indicates that after dynamical chiral symmetry breaking the effective, constituent quarks behave as heavy, non-relativistic particles. Spectroscopy and data on the residual interactions of ordinary, and in particular light gluonic mesons, will therefore provide with crucial information about the connection between the two main features of low energy QCD.

We note that conventional mesons and baryons can only supply information on the static properties of the ground state gluonic flux tube. One must explore the properties of hybrids and glueballs to obtain information on the *dynamics* of soft glue. In addition, molecular states are the simplest hadrons which probe the *color structure* of this dynamics.

As stated above, the nature of the appropriate effective degrees of freedom for glue can only be determined by a long process of calculation and comparison with experimental and lattice data. There are two broad theoretical ideas in this regard: it is some sort of string or flux tube[4, 5, 6] or it is an effective constituent confined by a bag[7, 8] or potential[9, 10, 11]. Perhaps the most compelling indications that low energy glue is string-like come from lattice calculations of energy, action, or field densities between static color sources which are reminiscent of flux tubes[12]. An intriguing clue is also provided by the spin splittings of heavy quarkonia. It is known that an effective interaction

free of long range exchange spin-orbit coupling is needed to reproduce the mass splitting of the ^3P_J heavy quarkonium multiplets. However, an analysis of QCD in the heavy quark limit convincingly demonstrates that obtaining such an effective potential requires that low energy glue must be string-like[13].

Alternatively, pointlike models of low energy glue have a long history, originating with MIT bag model calculations of Barnes[7] and others[8, 14, 15]. Horn and Mandula[9] were the first to consider a potential constituent glue model of hybrids. Their hybrids consisted of constituent quarks and pointlike, massless, spinless, and colorless glue in a nonrelativistic potential model. The confining potential was taken to be linear with a string tension given by the ratio of color Casimir operators: $b_{qg} = 9/8 b_{q\bar{q}}$.

It is clear that flux tube and constituent glue models present very different concepts of the behavior of soft glue. An extensive and high quality experimental effort will be needed to clarify this situation.

3.2.3 Phenomenology and confinement

With a few exceptions, such as spin splitting of quarkonia, and the phenomenology of strong two body decays, we have had to rely on lattice calculations to provide indormation on confinement. Most notable are predictions for hybrid masses [16, 17, 18, 19, 20], convergence in the low lying glueball spectrum [21, 22, 23, 24], and the calculation of the potential surfaces for excited glue configurations with static quarks[19]. The latter is especially useful for comparison with model predictions. For example it has recently been compared to the bag model [25], the flux tube model [26], Nambu-Goto inspired models [27], and to a relativistic constituent glue model[28].

Several interesting features have emerged. Although it is believed that glue must behave in a string-like fashion at large quark separation, this behavior is not being seen on the lattice (there are now indications that it may be occurring at very large distances[26]). Alternatively, constituent models have been shown to either contain the wrong degrees of freedom (and so are unable to describe all of the possible gluonic excitations seen on the lattice) or to approach the linear confining regime too quickly[28]. The latter is interesting because it implies that more degrees of freedom than a single constituent gluon are required to describe hybrids at moderate to large interquark separation.

Although the lattice is useful for obtaining static information about hadrons, it is very difficult to calculate hadronic decays or interactions numerically. Thus the experimental explication of this important area of hadronic physics is crucial. At present there are very few models of hybrid decays. These comprise older perturbative gluon-based models[29, 30, 31], the well-known flux

$\hat{\rho} \to (b_1\pi)_L$	Γ MeV/c^2	
	Ref. [35]	Ref. [32]
$L = 1$	78,40,37	51
$L = 2$	2,3,1	11

Table 3.1: Predicted partial widths of the 1^{-+} exotic hybrid at 1.6 GeV/c^2 decaying into $b_1\pi$. The three sets of numbers in the second column show the sensitivity to different model parameters.

tube decay model[32, 33], and a new flux tube-based decay model[34, 35]. The importance of understanding this aspect of hybrids cannot be overstated. For example, simply detecting hybrids will be difficult without some guidance as to how they decay. We stress that models of hybrid decays are built upon assumptions of hybrid structure and decay mechanisms. As an example of this point we note that in the flux tube model vector hybrids contain quarks in a spin singlet. In constituent models; however, the quarks may be in a spin triplet. This simple difference in structure may lead to large differences in the decay characteristics of vector hybrids because it is widely held that states with quarks in a singlet cannot decay to mesons which also have their quarks in spin singlets (the $S = 0 \not\to (S = 0) + (S = 0)$ rule).

Although the prospects of constructing a reliable model of hybrid decay seems daunting without extensive input from experiment, an interesting phenomenon has been observed in all hybrid decay models considered to date: hybrids couple weakly to identical S-wave mesons[1]. Thus for example a hybrid with the quantum numbers of the ρ will not decay to $\pi\pi$ and only weakly to $\omega\pi$ but strongly to πa_1. This observation can be used to distinguish hybrids from the conventional spectrum. Even though the hierarchy of hybrids decays have been found to be rather insensitive to the details of the underlying dynamics, as illustrated in Table 3.2.3 if there is more than one wave present in a given decay mode the relative strengths are highly sensitive probes of hybrid structure. It is apparent that a detailed partial wave analysis will be crucial in discriminating between models of soft glue.

3.2.4 Conventional light quark mesons - theory

The conventional light meson spectrum is reasonably well understood theoretically as regards the spectrum of states and their approximate masses. Electro-

[1]The model of Ref.[34] generalizes this: hybrids couple weakly to all pairs of identical mesons.

magnetic transitions, which are clearly relevant to studies of photoproduction, are known for many of the light S-wave mesons and for several P- wave states, and are in good agreement with simple electric and magnetic dipole transition rate formulas. Strong decays are much less well understood, indeed the mechanism of strong decays may be the most important open question in the field of light conventional hadron spectroscopy. There is a phenomenological model of light meson decays, known as the $^3P_0$ model, which assumes that meson decay takes place through pair production of a $q\bar{q}$ pair from the vacuum, with $S = 1$, $L = 1$, $J = 0$ quantum numbers. Other decay models are generally simple modifications of the spatial strength of pair production that do not change this decay mechanism. Although the complete relation between this decay model and QCD dynamics of light quarks has not been established, it can be related to QCD in the case of production of nonrelativistic quarks in the strong coupling limit [36]. It is sufficiently accurate that it gives a fair description of partial widths and relative decay amplitudes for decays of well established $q\bar{q}$ states. An accurate description of decay amplitudes of conventional $q\bar{q}$ mesons is important in part because we expect the anomalous strong decay amplitudes of nonexotic glueballs and hybrids to distinguish them from nonexotic $q\bar{q}$ states with identical quantum numbers and similar masses. Indeed the strong decay amplitudes may be the only information we have for new strongly unstable meson resonances at higher masses. The spectrum of conventional light $q\bar{q}$ resonances is discussed in detail in the work of Godfrey and Isgur [37] and Mukhopadhyay [38, 39] , and more recent addenda regarding decays of $s\bar{s}$ states have been given by Godfrey *et al.* [40, 41]. An exhaustive calculation of all allowed quasi-two-body strong decay amplitudes in the $^3P_0$ model for all $n\bar{n}$ (where n refers to u or d quarks) mesons expected up to 2.1 GeV/c^2 has been published recently by Barnes, Close, Page and Swanson [3]. These theoretical results should suffice to distinguish between plausibly $q\bar{q}$ and non-$q\bar{q}$ mesons in the mass regime of greatest current interest, provided that the $^3P_0$ model remains accurate for these higher-mass states.

3.2.5 Glueballs - theory

There has been tremendous interest in finding glueballs, as they are conceptually the furthest removed from the conventional $q\bar{q}$ of all the mesons expected in QCD. Although many anticipated properties of glueballs may be strongly model dependent, there are reliable LGT predictions [21, 22, 23, 24] of a lightest scalar glueball mass of 1.5 to 1.7 GeV/c^2. The next glueballs found above this scalar in LGT studies are 0^{-+} and 2^{++}, both expected at a mass of about 2.2 to 2.3 GeV/c^2, with all other J^{PC} found at higher masses.

Since these lighter glueballs are nonexotic, one can hope to identify them through *overpopulation*, as anomalous extra states in the background of conventional $I = 0$ $q\bar{q}$ mesons. Here we are unfortunate, since $I = 0$ 0^{++} is probably the most obscure sector in the entire light meson spectrum, with broad states $f_0(1300)$, $f_0(1590)$, $f_0(1700)$ and the narrow $K\bar{K}$ candidate $f_0(980)$. Conventional $I = 0$ $n\bar{n}$ and $s\bar{s}$ states are expected at about 1.3 and 1.5 GeV/c^2 in the quark model; these are likely to be rather broad, although the $^3P_0$ model predictions for their width are quite sensitive to their radial wavefunctions.

Several experiments at the LEAR $p\bar{p}$ facility at CERN have found a rather narrow $f_0(1500)$ scalar [42, 43], with a total width of about 120 MeV/c^2, which has been widely claimed as the scalar glueball. There are complications with this identification, however. The reduced decay couplings to pseudoscalar pairs do not follow the naive 3:4:1 $\pi\pi : K\bar{K} : \eta\eta$ ratio expected for a flavor singlet, instead the $K\bar{K}$ mode appears quite weak. Recent LGT studies of the $|k|$ dependence of glueball-Ps-Ps couplings finds the opposite result [23], that heavier mesons should be produced preferentially from scalar glueball decay, and for this reason the $f_0(1700)$ might instead be the scalar glueball. In either case these are rather narrow states, so one might also hope to find the 0^{-+} and 2^{++} glueballs as unusually narrow states. Of course the spectrum around 2.2 and 2.3 GeV/c^2 is poorly known, so this cannot be investigated without higher statistics high- mass data.

3.2.6 Hybrids - theory

The area of greatest interest in recent studies of meson spectroscopy has been the subject of hybrids. Hybrids are formally defined as mesons that have both $q\bar{q}$ and glue in their dominant *valence* basis state; clearly this is a working definition, and complications such as large levels of $q\bar{q} \leftrightarrow q\bar{q}g$ mixing in physical resonances might require a more careful classification. One can at least be confident that there will be more states than expected by the naive quark model, since the presence of both $q\bar{q}$ and $q\bar{q}g$ basis states will lead to more physical resonances than would follow given only $q\bar{q}$ basis states. As with glueballs, overpopulation forms one of the strategies in searching for hybrids.

There is a much more striking signature for hybrids, which is a principal reason they are so attractive experimentally: they can have exotic quantum numbers and the discovery of a resonance with exotic J^{PC} would be convincing evidence of a non-$q\bar{q}$ meson. The search for exotic hybrids is the most exciting topic in modern meson spectroscopy, as no such states have been universally accepted as confirmed, but there are several plausible candidates. The $J^{PC} = 1^{-+}$, especially $I = 1$ is of greatest current interest since it is ex-

pected theoretically to be the one of lightest and most stable of the light-quark hybrids.

Theorists have given detailed predictions of the spectrum of hybrids and their strong couplings. Many techniques have been used in these calculations, beginning with the bag model and continuing with constituent gluon models, QCD sum rules and the flux tube model. Common conclusions were that there should be a relatively light $J^{PC} = 1^{-+}$ exotic in the lowest multiplet (where determined), with a mass in the 1.5 to 2.0 GeV/c^2 region. These estimates have been improved on recently by lattice gauge theory calculations, which presumably lack most of the systematic uncertainty of models. The LGT results [44, 17] find that the $J^{PC} = 1^{-+}$ is indeed the lightest hybrid exotic, with a mass close to 2.0 GeV/c^2. Although this appears to vindicate the flux tube model of Isgur, Kokoski and Paton [32], which estimated the mass of the $J^{PC} = 1^{-+}$ exotic to be 1.9 GeV/c^2, one should note that the $J^{PC} = 0^{+-}$ exotic which the flux tube predicts to be degenerate with 1^{-+}, is found by LGT to be about 0.7 GeV/c^2 higher in mass! Evidently we still have much to learn about the spectrum of hybrids.

Calculations of strong decay modes of hybrids are of great interest, since these should let us distinguish between non-exotic hybrids and quarkonia, and also because they may indicate which hybrids are most accessible in photoproduction. The more recent decay calculations have relied exclusively on the flux tube model, which may or may not be accurate for these novel states. The most familiar work is that of Isgur, Paton and Kokoski [32], who found the hybrid selection rule, that the lightest hybrids should decay dominantly to S+P meson pairs rather than the simpler S+S modes. This implies for example that a hybrid search for an $I = 1$ $J^{PC} = 1^{-+}$ should concentrate on unfamiliar quasi-two-body modes such as $\pi f_1(1285)$ and $\pi b_1(1235)$ rather than the more experimentally accessible $\pi\eta$ and $\pi\rho$. This paper found that the total widths of several hybrids should be relatively narrow ($\Gamma_{tot} \approx 150$ MeV/c^2), notably including the $I = 1$ $J^{PC} = 1^{-+}$. The Isgur *et al.* reference only considered the more obvious exotic hybrids, whereas the flux tube predicts 5 nonexotic J^{PC} nonets at the same mass as the 3 exotics, 0^{+-}, 1^{-+} and 2^{+-}. With this many states, overpopulation could be evident if any of the nonexotic hybrids are narrow. The calculations of these nonexotic hybrid decays in the flux tube model were carried out by Close and Page [33], who found that several of these hybrids are indeed predicted to be quite narrow. Especially attractive nonexotic hybrids are relatively narrow 2^{-+} states in both I=0 and I=1, and a remarkably narrow $I = 0$ 1^{--}, with a total width of 100 MeV/c^2.

Finally, perturbative QCD signatures of hybrids have been theoretically investigated by Carlson and Mukhopadhyay [45].

3.2.7 Multiquark systems - theory

The best known *multiquarks* are nuclei, which are weakly bound associations of largely unmodified color-singlet nucleons. Similarly we know of many examples of hypernuclei, in which a nucleon has been replaced by a Λ, and the famous $\Lambda(1405)$ appears plausible as a weakly bound $\bar{K} - N$ meson-baryon nucleus. The $f_0(980)$ and $a_0(980)$ are likely cases of weakly bound meson pairs, and if so are our first examples of mesonic nuclei. There are many arguments in favor of this interpretation (see Weinstein and Isgur [46, 47]), most obviously that they are just below $K\bar{K}$ threshold, have S-wave $K\bar{K}$ quantum numbers, are 0.2 to 0.3 GeV/c^2 lighter than expectations for 0^{++} nnbar states, and are very narrow compared to expectations for scalar quarkonia at this mass.

Although the $f_0(980)$ and $a_0(980)$ can be explained as dominantly $K\bar{K}$ molecules, earlier predictions of four-quark states with these quantum numbers at light masses has resulted in persistent speculations that these might actually be $q^2\bar{q}^2$ clusters, once known as *baryonia* [48, 49]. These issues can be tested through photoproduction of an initial $\phi(1020)$ and a measurement of radiative transition rates. Preliminary experimental results from Novosibirsk [50] are closer to the theoretical $q^2\bar{q}^2$ branching fraction, although they may include important non-980 backgrounds.

There is likely to be a rich spectrum of similar exotic molecules in other sectors, such as vector-vector, so confirmation (or disproof) of the $K\bar{K}$ molecule hypothesis would be a very important step in the study of multiquark systems.

3.2.8 $s\bar{s}$ states - theory

The quark model describes conventional light mesons as bound states of quarks and antiquarks, interacting through perturbative gluon exchange at short distance and a nonperturbative confining interaction at large distances. Four "flavor" types are distinguished according to the type of quark and antiquark in the meson; in the light $q\bar{q}$ mesons we can have any of the three light quarks u, d, s and their antiquarks. If both q and $\bar{q}$ are of u, d type we have a "nonstrange meson", which we refer to generically as $n\bar{n}$. With one chosen from $n = u, d$ and the other s, we have an $n\bar{s}$ or $s\bar{n}$ "kaonic state". The remaining possibility, $s\bar{s}$, is called "strangeonium".

The nonstrange $n\bar{n}$ mesons are fairly well established experimentally at lower masses, *albeit* with notable exceptions such as the scalar states. Taking 2.2 GeV/c^2 as a current frontier of light meson spectroscopy, the quark model anticipates 44 $n\bar{n}$ states up to this mass. (These are the 1S, 2S, 3S, 1P, 2P, 1D, 1F = 22 J^{PC} levels, with a doubling for $I = 0$ and $I = 1$.) About half these

mesons have been identified experimentally. Similarly we anticipate 22 kaonic J^{PC} levels ($n\bar{s}$ and $s\bar{n}$), and about 2/3 of these are known. In comparison the $s\bar{s}$ "strangeonium" states are a *terra incognita*; only 6 of the corresponding $s\bar{s}$ states are well established. These are the $\eta(547)$ and $\eta'(958)$ (counted as one $s\bar{s}$ state), $\phi(1019)$ $h_1'(1380)$, $f_1(1420)$ $f_2'(1525)$ and the $\phi_3(1854)$.

Photoproduction is an excellent technique for producing $s\bar{s}$ mesons, because the incident photon is in effect a vector meson beam with a large ϕ-meson component. Much of the photon-hadron interaction takes place through vector dominance, in which the incident photon becomes a vector meson. The relative probability of interacting through the different light meson types $\rho^o : \omega : \phi$ is $9 : 1 : 2$ according to the quark model, and this relative coupling strength is approximately confirmed by the diffractive cross sections for vector meson photoproduction. (There is an additional suppression of the $s\bar{s}$ cross section by about a factor of two that is not well understood.) Thus in photoproduction we have the opportunity to produce mesons with vector meson beams of all diagonal light flavors $u\bar{u}$, $d\bar{d}$ and $s\bar{s}$, with a known relative luminosity between the flavors. In addition to diffractive photoproduction, which produces C=(-) states, other mechanisms such as t-channel vector exchange may lead to significant photoproduction of C=(+) $s\bar{s}$ states. In contrast, hadronic production of $s\bar{s}$ states is suppressed because the initial hadrons provide at most one strange valence quark (for example in KN experiments such as LASS).

The $s\bar{s}$ sector is also attractive because some decay modes should be very "clean". These include channels such as $\phi\eta$, $\phi\eta'$ and $\phi\phi$, which according to the Zweig rule should only arise from $s\bar{s}$ initial states. One may also study channels such as $\phi\pi$, which expected *not* to show evidence for $q\bar{q}$ states; one might find evidence for molecular states or Zweig-rule violation in this channel. Observation of both the $n\bar{n}$ and $s\bar{s}$ partners of a flavor nonet would be useful for establishing the $q\bar{q}$ (and $q\bar{q}$ hybrid) spectrum, since the relative photoproduction amplitudes can be estimated. This would distinguish a $q\bar{q}$ or hybrid flavor nonet from a meson-meson molecule or a glueball, as molecules and glueballs do not span nonets.

The total widths of $s\bar{s}$ states are predicted on average to be comparable to the widths of $n\bar{n}$ states. Detailed calculations in the $^3P_0$ model [51, 52] do however find some rather narrow states. Four of the $s\bar{s}$ states anticipated in the 1.6-2.2 GeV/c^2 region are predicted to have widths in the 100-200 MeV/c^2 range: These are the $^3D_3$ $\phi_3(1854)$ (predicted total width 104 MeV/c^2, observed $\approx$ 90 MeV/c^2), the $^3D_2$ (predicted 214 MeV/c^2), the $^1D_2$ $\eta_2(1850)$ (predicted 129 MeV/c^2) and the $^3F_4$ $f_4(2200)$ (predicted 154 MeV/c^2, possibly observed by LASS [53] with a total width of roughly 100 MeV/c^2.) Since the $\rho_3(1690)$ has been reported in diffractive photoproduction, the $\phi_3(1850)$

should also be observed, with a known cross section. The as yet unknown $\phi_2(1850)$ (expected in K^*K) is interesting as a test of the quantum number dependence of the diffractive photoproduction mechanism. It might also be produced through $\phi\eta$ collisions in η exchange (a strong coupling to $\phi\eta$ is predicted), and could be observed in the $\phi\eta$ final state. Studies of these narrower states, especially the as yet unknown levels, will be useful as tests of our decay models, photoproduction mechanisms, and mixing with non-$s\bar{s}$ components.

The vector sector provides an example of the paucity of information on $s\bar{s}$ spectroscopy. As in the $n\bar{n}$ case one expects both $L = 0$ and $L = 2$ vectors, a 2^3S_1 and a $^3D_1$. In the $I = 1$ $n\bar{n}$ sector there has been progress recently in separating these states [54, 55]. Experimentally there are somewhat overlapping $\rho(1450)$ and $\rho(1700)$ states, which both appear to be present in diffractive photoproduction. Usually the 1450 state is assumed to be 2^3S_1 and the 1700 is $^3D_1$, since the nonrelativistic quark model anticipates approximately this mass splitting between spectroscopically pure $n\bar{n}$ levels. The $^3P_0$ decay model predicts that these states should have very different couplings to the S+P modes πh_1 and πa_1; these should couple very strongly to $^3D_1$ but quite weakly to 2^3S_1. A recent study of 4π modes by the Crystal Barrel has confirmed this result. In the $s\bar{s}$ sector only one higher-mass vector state has been reported, the $\phi(1680)$. This is seen in e^+e^- annihilation and in photoproduction, and apparently decays to KK but dominantly to K^*K. Can one similarly confirm that this state is the 2^3S_1 level as the mass suggests? If so, should the unknown higher-mass $^3D_1$ be observable in any particular final states? The experimental situation is summarized in Table 3.2.8 ; it is consistent with the 2^3S_1 $\phi(1680)$ identification, but only qualitative information on branching fractions is available, and the crucial $K_1(1273)K$ mode has not been investigated. Both states should appear in the clean $\phi\eta$ mode, but again this has not been studied. Thus we have the beginnings of $s\bar{s}$ spectroscopy, but quantitative studies of interesting and characteristic modes such as $\phi\eta$ and the "$s\bar{s}$ workhorse" modes KK, K^*K, K^*K^* and K_1K simply have not been carried out. We may find many surprises in the $s\bar{s}$ sector, especially as regards mixing with non-$s\bar{s}$ states.

If these $s\bar{s}$ states were expected to be simple copies of the $n\bar{n}$ states, with a mass higher by ca. 250MeV/c^2, establishing the $s\bar{s}$ spectrum might be considered a mundane exercise. However even the lightest $s\bar{s}$ system, the η and η', show a remarkable and poorly understood strong mixing with $n\bar{n}$; the physical states are close to the maximally mixed $(|n\bar{n}\rangle \pm |s\bar{s}\rangle)/\sqrt{2}$ combinations. This is due to a large $q\bar{q}$ annihilation amplitude in the 0^{-+} channel, which has been

	KK	K^*K	K^*K^*	$K_1(1273)K$	$\phi\eta$
expt.(1680 region)	seen	dominant	-	-	-
theor. 2^3S_1(1680 assumed)	89	245	0	0	44
theor. $^3D_1$(1850 assumed)	65	75	5	465	29

Table 3.2: Predicted and observed partial widths (in MeV/c^2) of the two 1^{--} $s\bar{s}$ states 2^3S_1(1680) and $^3D_1$(1850).

attributed to various perturbative and nonperturbative QCD mechanisms but has never been convincingly explained. This large mixing is presumably due to annihilation through the gluonic sector, but why 0^{-+} shows such a large annihilation amplitude, whereas others such as vector and tensor are relatively unmixed, remains a mystery. The discovery of the CERN glueball candidate has added more information to this puzzle [22, 56, 57, 58, 59, 60, 23]. The observed decays of the $f_0(1500)$ are far from the flavor-symmetric pattern of $\pi\pi : KK : \eta\eta : \eta\eta' = 3 : 4 : 1 : 0$ (for branching fraction divided by phase space) that one would expect from a simple model of glueball decay, and instead strongly favor $\pi\pi$. This may be due to an intrinsic quark mass dependence of these couplings (as suggested by the LGT results of Weingarten et al), or (as suggested by Close and Amsler) it may be due to a large $n\bar{n} \leftrightarrow G \leftrightarrow s\bar{s}$ mixing similar to the $n\bar{n} \leftrightarrow s\bar{s}$ mixing in the $\eta - \eta'$ system. While all J^{PC} channels will provide important information regarding $n\bar{n} \leftrightarrow s\bar{s}$ mixing, the most likely *a priori* to show a significant effect are the radial pseudoscalars (perhaps the $\eta(1295)$ and the one time glueball candidate $\eta(1440)$) and the 2^{-+} pseudotensors. 2^{-+} is interesting because this is one of the lighter glueball channels, and there are η_2 states at about 1.65 and 1.87 GeV/c^2 (reported by Crystal Barrel [61]) both of which couple strongly to modes forbidden to $s\bar{s}$ by the Zweig rule.

3.3 Physics with ϕ mesons

Meson pair production with invariant mass near and above 1 GeV/c^2 is of prime importance for accessing the possible influence of coupled channel effects in meson spectroscopy and the need for "unquenching" of the quark model [62, 63, 64, 65, 66]. Photoproduction of vector mesons is one of the clean and reasonably well understood cases of diffractive production. In the region of interest, photoproduction of ϕ mesons dominates and gives a good benchmark signal allowing other waves to be cleanly identified in the partial wave analysis. The dominant, two kaon decay mode of the ϕ can thus be com-

pared with the $K\bar{K}$ signal from background waves. The former carry crucial information about residual meson-meson interactions. These interactions are sensitive to the nature of the effective, QCD degrees of freedom and may come from quark or meson exchanges. They also provide test of the applicability of chiral symmetry beyond chiral perturbation theory [67, 68]. In studies of these residual interactions, $K\bar{K}$ threshold scattering plays a similar role to the one played by the low energy NN scattering in determining properties of the NN force. However, unlike the NN case, the experimental knowledge about threshold $K\bar{K}$ parameters is essentially nonexistent [69].

When measured together with $\pi\pi$ and $\pi\eta$, the coupled channel analysis will help resolve the "scalar meson puzzle" associated with the structure of the f_0 and a_0 mesons. As discussed earlier these are prime candidates for non-$q\bar{q}$ states. It is important to stress the ability of detection of neutral and charged modes simultaneously. This will enable isospin decomposition and also further studies of meson mixing due to isospin breaking ($a_0 - f_0$, $a_2 - f_2$). So far the only well documented case of such mixing comes from the $\rho-\omega$ channel. Above the ϕ region, production of $\pi\eta'$, 2η and $\eta\eta'$ will complement the analysis of the 980 region and enable a comprehensive mapping of the scalar and tensor multiplets in the $1 - 2\mathrm{GeV/c^2}$ mass range.

Since the ϕ-meson is primarily an $s\bar{s}$ pair lies in between the light and heavy quark sectors of QCD. From the theoretical point of view it thus provides a bridge between effective theories based on the chiral and the heavy quark expansions. These ideas could be tested by comparing theoretical predictions with detailed experimental information on diffractive photoproduction including polarization observables.

Finally, as will be discussed in more detail below, ϕ photoproduction has several advantages over the kinematics of a collider mode ϕ factory which would make HALL D competitive in the measurement of rare decays of the ϕ and possibly in symmetry tests as well [70, 71, 72].

3.3.1 S/P interferometry

The very limited, existing data on charged kaon pair production with invariant mass near 1 $\mathrm{GeV/c^2}$ comes form DESY [73] and Daresbury [74] and clearly identifies the presence of a strong S-wave signal under the P-wave ϕ peak. The different angular, energy, and t-dependencies of the two waves give a unique opportunity to study the physics of threshold production.

When it comes to details the two experimental results are seemly inconsistent with each other. The diffractive $\gamma p \to \phi p$ is dominated by the helicity-nonflip P-amplitude and therefore $\rho^{11}_{\pm 1,\pm 1}$ is the largest spin-density matrix

element. The signal for S/P interference is then expected to show up in the $\rho^{10}_{\pm 1,0}$ spin-density matrix element. However, angular momentum conservation implies that at low-t, $\rho^{10}_{\pm 1,0}$ has to be built from amplitudes that conserve nucleon helicity. If on the other hand, S-wave production is dominated by nucleon-helicity-flip, as expected for example in a production via ρ-exchange than one would expect $|\rho^{10}_{\pm 1,0}|/|\rho^{11}_{\pm 1,\pm 1}| \sim |\rho^{10}_{0,0}|/|\rho^{11}_{\pm 1,\pm 1}| \sim O(0.01-0.1)$. Experimentally this does not seem to be the case. The dominant interference signal comes from the $\langle Y_{10} \rangle$ moment indicating larger than expected dominance of the S-wave, nucleon-helicity-flip over the nonflip amplitude. The different P-wave helicity amplitudes are separately interesting since they provide a measure for the s-channel helicity nonconservation in diffraction. As mentioned above one should keep in mind however the poor statistics of the two experiments which makes them rather inconclusive. The 3500 events collected as DESY should now be compared with 10^5 events per day expected in the first stage of HALL D operations. High statistics will enable to analyze the t-dependence of individual partial waves which is very important for isolating different production mechanisms and thus for identification of the produced resonances. This will be further enhanced by the use of linear polarization of the photon beam which enables to discriminate between naturalities of the t-channel exchanges.

3.3.2 Rare decays

At HALL D the copiously produced vector, ρ, ω, ϕ, pseudovector η, η' and strange, $K^{\pm}$, $K_{S,L}$ mesons will enable to carry out extensive symmetry tests. HALL D will therefore act as a boosted vector meson factory. Operating at the ϕ peak with 5×10^7 photons/s HALL D will deliver approximately 30ϕ's per second. This is a factor of 10 smaller than what is expected at the dedicated ϕ-factory, DAΦNE at Frascati when operating at the projected luminosity of $5 \times 10^{32} cm^{-1} s^{-1}$. Hadronic photoproduction however, has its unique virtues which could easily make up for initially lower statistics (with the expected 5×10^8 photons per second in the second stage this will not be an issue). These are the boost factor which enhances detection capabilities for low energy photons, photon polarization and the existence of a strong S-wave under the ϕ-peak. All these will help to isolate a rare signal from various backgrounds. The largest ϕ radiative decay mode is to $\eta\gamma$. With the branching ratio, $BR(\phi \to \eta\gamma) = (1.29 \pm 0.07) \times 10^{-2}$ it will be used is a primarily source of the η mesons. There are a number of allowed radiative decay channels which have not yet been observed and are important from the spectroscopic point of view: $\phi \to \gamma f_0(a_0)$, $\phi \to 2\pi\gamma$, $\phi \to K\bar{K}\gamma$, $\phi \to \pi\eta\gamma$ [75]. Recently the CMD-2 collaboration reported 6 candidate events for the $\phi \to \eta'\gamma$ which lead

to a branching ratio for this decay of $(1.2 + 0.7 - 0.5) \times 10^{-4}$ [76]. In the first stage of HALL D operations during one year we thus expect to collect of the order of 10^5 of such events. The physics of the η and η' mesons is of great interest from the perspective of the U_1 axial anomaly, quark flavor symmetry, origins of confinement and is expected to give insight into the structure of the QCD vacuum [77]. The C-parity violating decays $\phi \to \rho\gamma$, $\phi \to \omega\gamma$ and $\eta\pi^0$ have not been seen so far, and upper limits on the branching ratios are of the order $10^{-2} - 10^{-4}$. The hadronic modes $\phi \to 3\pi$ and $\phi \to \rho\pi$ break OZI rule and are sensitive to the $\rho - \omega$ mixing. The phenomenological OZI rule states that there is a suppression of ϕ decays to final states with no strange quarks. OZI rule and isospin break together in $\phi \to \pi^+\pi^-$, $\phi \to \omega\pi^0$ and $\phi \to \pi^+\pi^-\eta$ which probe the $\phi - \rho$ mixing. From the theoretical point of view measurements of these decays are important since meson mixing mechanisms are very sensitive to the underlying quark dynamics and thus the structure of confinement. Production of the $\gamma K\bar{K}$ and $\gamma\pi\eta$ states gives another handle on the structure of the low lying scalars around 1 GeV/c^2. Resonant production though the P-wave ϕ decay, $\phi \to \gamma K\bar{K}(\eta\pi)$ can potentially differentiate between the $q\bar{q}$, molecular and four-quark models of these states. Theoretical predictions by Close, Isgur and Kumano lead to a ratio of the branching ratios : $BR(\phi \to a_0\gamma)/BR(\phi \to f_0\gamma) = 0, 1, 9$ for the three possibilities respectively [49]. The individual branching ratios are expected in the range $10^{-4} - 10^{-6}$. Thus $10^3 - 10^5$ of such event per year are expected. Another possibility will be to measure direct S-wave production through S/P interference, as discussed earlier. This could be used to measure the radiative decays $S \to \gamma K\bar{K}(\eta\pi)$ $(S = f_0, (a_0))$ and directly probe wave function of the scalar mesons. Here in particular the large boost factor, $\gamma_\phi = E_\phi/m_\phi \sim E_\gamma$ is relevant as it enhances photon acceptance. MeV/c^2.

As a source of the η mesons the reaction $\gamma p \to \phi p \to \eta\pi p$ will deliver 10^7 η's per year. The known η decays are all electromagnetic, hadronic decays break isospin and are therefore of electromagnetic origin too. Since hadron energy released in η decays is small, (m_η = 550 MeV/c^2) these give excellent opportunities for studies of low energy effective hadronic theories such as chiral Lagrangians and the applicability of chiral perturbation theory. Three body decays are of particular interest. Various theoretical approaches are now beginning to converge on the absolute decay rate for $\eta \to 3\pi$ however discrepancies still exist in the description of the Dalitz plots. For the same reason quality data for the $\eta \to \pi^+\pi^-\gamma$ decay is also needed [78].

HALL D, with the expected 5×10^8 kaons/year will also contribute to the measurement of the weak, radiative kaon decays. These are also sensitive probes of soft hadronic interactions since, in particular decays to states with

pions and any number of photons probe the higher $O(p^4)$ terms of the chiral Lagrangian [79]. Even though statistics is not expected to be higher than at DAΦNE boosted kinematics, in particular for measurements of channels with a large photon multiplicity will provide complementary analysis with very different systematics.

3.3.3 Future plans

Along the lines of symmetry tests, in the second stage of the experiments with 5×10^8 tagged photons/s the new facility will contribute to studies of the CP violation and to tests of CPT symmetry. The CPT theorem is a profound and general result for local relativistic quantum field theories in flat spacetime [80]. Symmetry under CPT has been investigated experimentally in various systems to a high degree of precision [81]. In the neutral kaon system, for example, the mass difference $|m_K - m_{\bar{K}}|$ has recently been constrained to about $10^{-18} m_K$ [82]. The broad theoretical validity of CPT symmetry and the availability of precision experimental tests make CPT tests a valuable probe for fundamental theories that break one or more of the usual axioms underlying the CPT theorem[83, 84, 85, 86, 87, 88]. Experimentally such signals could appear in the neutral kaon system, and reasonable values for the magnitude of the CPT violating parameter δ_K could lie in a range just below the present experimental limit $\sim 10^{-3}$ [89]. The decay $\phi \to \bar{K}^0 K^0$ is an excellent source of correlated $K_L K_S$ pairs, which can be used to test fundamental symmetries. By studying the difference in flight times for different combinations of $\pi^+\pi^-$ and $\pi^0\pi^0$ decays of the kaons, one can extract the CP violating parameters, including the CPT violating phase δ_K. A photoproduction facility, provides several advantages over e^+e^- machines such as DAΦNE. Once more the boost factor makes calorimetry for the $\pi \to 2\gamma$ photons more straightforward, and it extends the $\pi^\pm$ lifetime and decay path, which simplifies π/μ separation. Another is a theoretical advantage accruing directly from the boost. It can be shown that the CPT violating parameter δ_K acquires a boost dependence from the associated apparent Lorentz breaking[90]. The magnitude of δ_K under favorable circumstances is enhanced by the boost factor. In this scenario, a sample of kaons at, say, 5 GeV would provide a sensitivity to CPT violation ten times that of a comparable size sample at rest. An equivalent rest sensitivity would require roughly 100 times the statistics. Finally, the presence of an S-wave in the $\gamma p \to K\bar{K}p$ reaction underneath the ϕ-peak produces $K_L K_L$ or $K_S K_S$ pairs. The S/P interference discussed before may therefore be used to amplify the signal for CPT violation by selecting the appropriate region of phase space [91]. With 10^8 photons/s reaction rates for $\gamma p \to \phi p$ are

competitive with rates at the e^+e^- factories. To take advantage of this, one would need to study the asymmetry in azimuthal angle in the ϕ helicity frame.

Chapter 4

Photon Beam

One of the unique opportunities presented by a CEBAF upgrade to energies of 8 GeV and beyond is the possibility of generating high-intensity c.w. photon beams for high energy photoproduction experiments. In this regime, photon beams represent an interesting extension to the meson spectroscopy program that has been actively pursued using beams of pseudoscalar mesons at hadron accelerator laboratories: with high energy photons one has essentially a bam of *vector* mesons. It is difficult, in fact, to conceive of any other way to obtain such a vector beam.

Vector beams offer at least two advantages in the search for a more complete understanding of the hadron spectrum. From the theoretical standpoint, vectors are interesting as a possible source of hybrid mesons because the two are connected in the flux tube model by a simple operator which excited the orbital motion of the flux tube. Thus, measuring the coupling between conventional and hybrid mesons is a direct way to probe the structure of hybrids. From the experimental point of view, the polarization of a vector beam offers new observables that are not available to experiments with pseudoscalar beams. These additional observables are useful to distinguish the exchange character of the production process and help resolve contributions from different interfering waves in the partial wave analysis of the final state.

4.1 Choice of technique

Three major methods have been considered for producing photons of the highest possible energy, flux and polarization from electrons in the energy range 8-12 GeV. The methods are ordinary bremsstrahlung, coherent bremsstrahlung and Compton backscattering of light. None of the methods are new and cal-

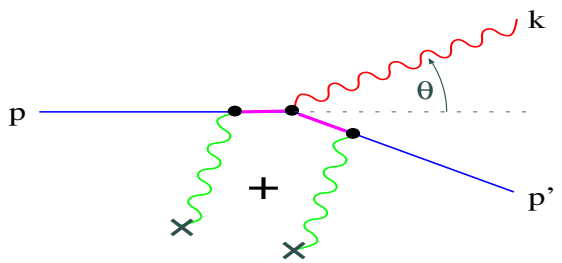

Figure 4.1: Generic diagrams for hard photon production from a high energy electron beam. The symbol $\times$ represents either a static charge distribution, in the case of virtual photons in the initial state (i.e. bremsstrahlung) or an optical cavity, in the case of real photons in the initial state (i.e. Compton scattering) The + denotes the fact that this leading order amplitude is actually the sum of two diagrams, one with the initial state photons attached to the incoming electron leg and one with it attached to the outgoing electron.

culation of the basic cross sections that underlie them are presented in most textbooks on applications of QED. All three techniques are actually described by the same Feynman diagram shown in figure 4.1

Each of these techniques has its own limitations and advantages. This, taken together with the requirements of the experimental program determine the method used to generate the photon beam. The experimental requirements (beam energy and polarization) are discussed below followed by a brief discussion of the properties of Compton backscattered and ordinary bremsstrahlung beams. The coherent bremsstrahlung technique is clearly the best choice to satisfy the requirements of the experimental program and this solution is then discussed in detail.

4.2 Energy requirements

The interesting range of meson masses for the study of gluonic excitations spans the region from the mass of the π^0 to just below $c\bar{c}$ threshold ($\approx$ 3 GeV/c^2). This range includes conventional ($q\bar{q}$) mesons and glueball and exotic hybrid masses, as predicted by lattice gauge calculations, flux tube models and bag models.

Figure 4.2 shows the maximum mass of particle X, in the reaction $\gamma p \to Xp$

as a function of incident photon energy. As can be seen from this plot, the desired mass range could be achieved with photon energies below ≈ 8 GeV. However higher energies are needed to produce mesons with sufficient boost so as to achieve good acceptance for the decay products of produced resonances.

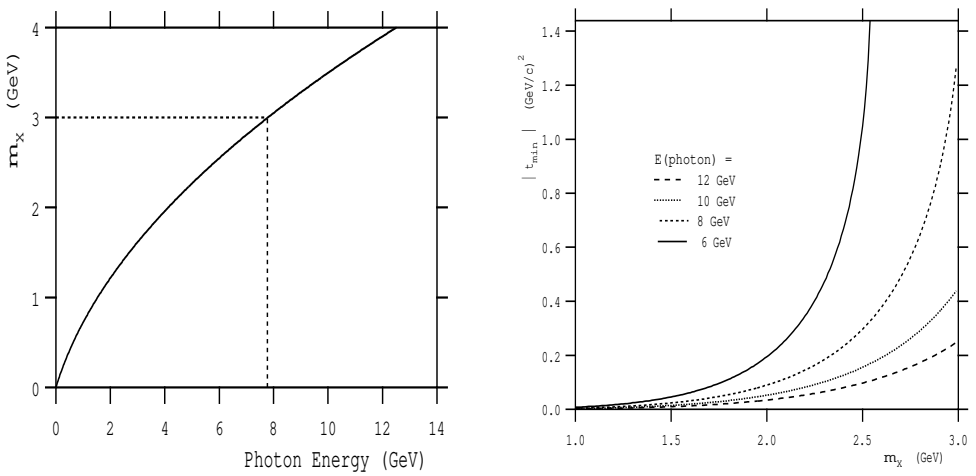

Figure 4.2: Kinematic limits on production properties for several choices of beam energy. (left) Maximum mass for particle X as a function of incident photon energy in the reaction $\gamma p \to Xp$. (right) The minimum value of $|t|$ as a function of the mass of particle X in the reaction $\gamma p \to Xp$ for various values of incident photon energies.

Higher energies are also needed to minimize the effect of the overlap of produced baryon resonances with meson resonances. This is illustrated by the Dalitz plot boundaries of Figure 4.3 for the reactions $\gamma p \to \pi\pi p$ and $\gamma p \to \eta\eta p$ for various incident photon energies. As the incident energy is increased from 4 to 8 to 12 GeV, the effect of overlap of produced mesons with produced baryon resonances (N^* or Δ) becomes less important.

Another important consideration in choice of energy is the effect of the minimum square of the momentum transfer, $|t_{min}|$ from incoming photon to outgoing meson required in the reaction $\gamma p \to Xp$. The dependence of $|t_{min}|$ on the mass of X is shown in Figure 4.2 for various incident photon energies.

The effect of $|t_{min}|$ can be illustrated in the production rate of mesons in peripheral processes. Figure 4.4 shows the mass spectrum of the meson system X in the reaction $\gamma p \to Xp$. Resonances with equal cross-sections are assumed but weighted by $dN/dt = e^{-8\cdot|t|}$. Resonance widths were all chosen to be 100 MeV/c^2 with masses of 1.0, 1.5, 2.0 and 2.5 GeV/c^2 for incident photon energies of 6, 8, 10, and 12 GeV. Clearly, photon beam energies of $\approx$

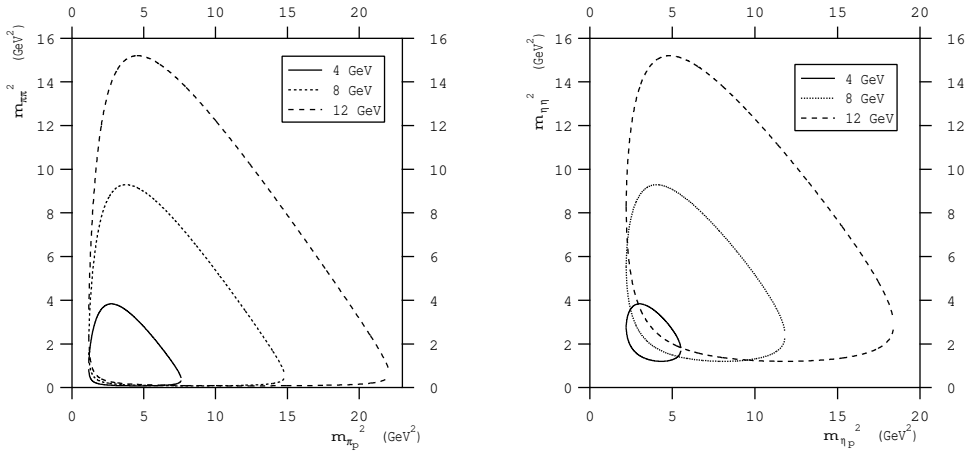

Figure 4.3: Dalitz plot boundaries for the reaction $\gamma p \to \pi\pi p$ (left) and $\gamma p \to \eta\eta p$ (right) for incident photon energies of 4, 8 and 12 GeV.

12 GeV are required if the mass region up to 3 GeV/c^2 is to be studied.

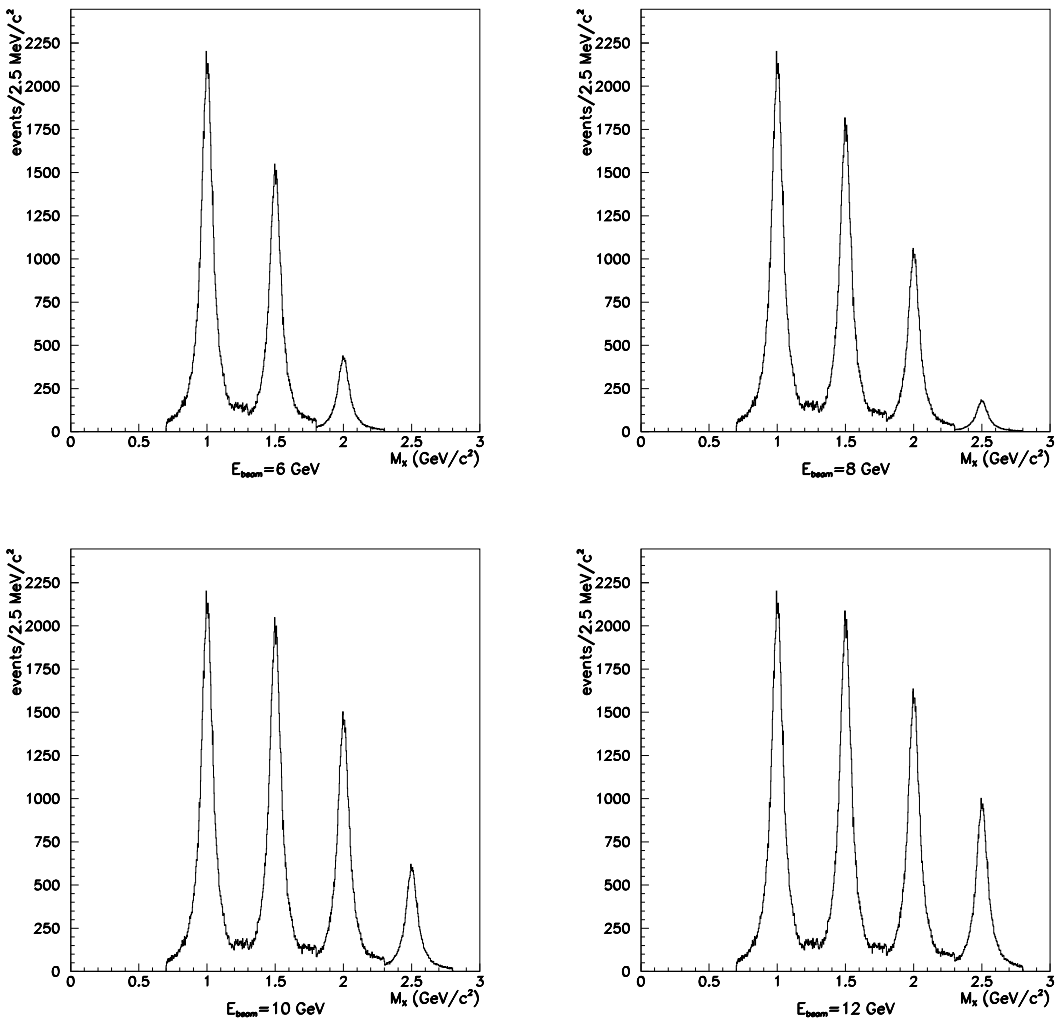

Figure 4.4: Plots of the mass distribution of 4 produced resonances in the reaction $\gamma p \to Xp$ taking into account the t_{min} effect for an incident photon energy of 6 GeV (upper left), 8 GeV (upper right), 10 GeV (lower left) and 12 GeV (lower right). (see the text for details).

4.3 Polarization requirements

From the point of view of physics of the HALL D the main difference between photon and hadron beams has to do with their quark content. With a good accuracy, photons may be viewed as a superposition of spin-1 $q\bar{q}$-pairs while a typical hadronic beam of pions or kaons is a source of valence spin-0 $q\bar{q}$ pairs. Thus, as compared to hadroproduction, photons may lead to different final states or similar final states may be reached via different production mechanisms. This unique quark structure of the photon might be of particular relevance for production of exotic states. This is because for low lying exotics theory predicts their valence $q\bar{q}$ pair to be in the spin-1 configuration [6].

The basic mechanisms of meson photoproduction are through diffraction, t-channel meson exchange and a decay of an excited baryonic resonance. From these three, at HALL D energies t-channel exchanges dominate. The hierarchy of exchanges suppresses those which require a change of several quantum numbers at once. Thus from the possible t-channel exchange the Pomeron exchange followed by a charge exchange are expected to dominate. Nevertheless at energies available at HALL D an extensive coverage of various production mechanisms is expected [92]. Real photons have two, transverse degrees of polarization and therefore are "richer" than π or K beams. This is reflected in the number of independent spin-density matrix elements. For example in photoproduction of vector mesons on an unpolarized proton target, $\gamma p \to VN$ there are 17 independent real spin-density matrix elements. For comparison, an analogous reaction with pion beams, $\pi p \to VN$ has only 4 independent real parameters in the spin-density matrix. Dynamical content of photoproduction is clearly larger. The crucial point however is how many of the spin-density matrix elements can actually be measured. In general this number depends on the type of photon polarization. In the above example if the vector meson is analyzed via its two body, (pseudo)scalar decay, *e.g.* $V = \rho \to 2\pi$ or $V = \phi \to K\bar{K}$ then linearly, circularly, and unpolarized photons access 9, 5, and 3 out of the 17 spin matrix elements, respectively [93]. In general linear polarization enables to extract the largest number of the spin-density matrix elements.

When t-channel exchanges dominate, linear polarization is even more important since it enables to isolate natural from unnatural parity exchanges. Naturality, τ of a state with intrinsic parity, η and spin J is defined as a product $\tau = \eta(-)^J$. Thus, for example the $\pi(J^{PC} = 0^{-+})$ and $a_1(J^{PC} = 1^{++})$ are unnatural, while the $\rho(J^{PC} = 1^{--})$ or the exotic $\hat{\rho}(J^{PC} = 1^{-+})$ are natural. Measurement of naturality of the exchanged particle together with its t-dependence and partial wave analysis are central for identification of pro-

duced mesonic resonances and understanding of production mechanisms. To see the connection between photon polarization and naturality in the t-channel consider a reaction $a+b \to c+d$ where a, b refer to the beam and target particle respectively and c, d to the produced meson and the recoiling baryon. We will assume that t-channel exchange of a particle, e or more generally of a Reggion dominates. This type of processes are best analyzed in the Gottfried-Jackson frame defined as the rest frame of the produced meson, (particle c) with the spin quantization, z-axis chosen in the direction of the beam (particle a) in that frame. Consider the case of pion beam first. It is possible to show that symmetry of the corresponding production amplitude $A(m_c) = A_{a+b\to c+d}$ under interchange $m_c \to -m_c$, where m_c is the spin projection of the produced meson (target and the recoiling baryon spins are implicit since they are irrelevant in the following discussion) is determined by the product of naturalities of the exchanged particle (τ_e) and that of the produced meson (τ_c). Thus, for a final state of given naturality, (say $\tau_c = +1$) determined by a partial wave $A(m_c)$ the two combinations

$$A^{U,N}(m_c) = \frac{1}{2}(A(m_c) \pm A(-m_c)) \tag{4.1}$$

isolate processes of opposite naturalities in the t-channel (if $\tau_c = -1$, A^U and A^N should be exchanged). For a photon beam an analogous partial wave, $A(m_a, m_c) = A_{a+b\to c+d}$ depends on the photon polarization, $m_a = \pm 1$. In this case when defining amplitudes which project onto definite naturality of the exchanged particle will also require flipping photon polarization (which is identical to photon helicity in the GJ frame). For $\tau_c = +1$ the corresponding two amplitudes are

$$A^{N,U}(m_c) = \frac{1}{2}(A(1, m_c) \pm A(-1, -m_c)) \tag{4.2}$$

with the definitions being reversed for $\tau_c = -1$. It thus follows that amplitudes with defined photon helicity *i.e.* corresponding to circularly polarized beams mix exchanges of different naturalities,

$$A(\pm 1, \pm m_c) = (A^N(m_c) \pm A^U(m_c)), \tag{4.3}$$

and to separate naturality of the exchanged particle it is necessary to measure coherent superpositions of the two helicity amplitudes. This can be achieved using linear polarization [93].

Finally lets focus on photoproduction of a $\hat{\rho}(J^{PC} = 1^{-+})$ exotic in a charge exchange reaction, $\gamma p \to \hat{\rho} n$ [94]. As discussed earlier, at HALL D energies one would expect diffractive photoproduction to dominate the total γp cross

section. However, since diffraction corresponds to a $C = +$ exchange the 1^{-+} exotic would not be produced this way. Charge exchange is the next, least suppressed production mechanism, and since $\gamma\hat{\rho}\pi$ coupling is not ruled out by any symmetry, at low t pion exchange is expected to dominate. This is good news since OPE is reasonably well understood at high energies. In this case linear polarization has another advantage. One can show that in the GJ frame the photoproduction amplitude $A(m_a, m_c)$ is proportional to either $\delta_{m_a m_c}$ or $\tau^3_{m_a m_c}$ depending on the naturality of the produced meson [95]. Thus in this case linear polarization selects naturality of the produced mesonic resonance. For a *natural* exotic, 1^{-+} state with mass around 1.5-1.6 GeV/c^2, as seen in the E852 data [96], the dominant backgrounds are expected from the *unnatural* $a_1(1260)$ and $\pi_2(1670)$ ($a_2(1320)$ is too narrow to significantly contribute in this mass region). Thus direction of linear polarization of the exotic signal is then expected to be at 90^o with respect to the backgrounds. This has obvious implications for the partial wave analysis.

4.4 Compton backscattered beams

The basic design of the Compton-backscatter source for this study was taken from C. Keppel and R. Ent [97]. The design entails the use of a four mirror high-gain cavity pumped by a 10 kW argon0ion laser putting out 2 *ps* pulses at a frequency of 100 MHz. The pulses in the cavity are synchronized so that light pulses in each of the arms crossing the electron beam intercepts an electron bucket on each pass through the beam. The total length of the cavity is 2m with a crossing angle of 1°. Both cavity and electron beam are focused to $10\mu m$ r.m.s. radius at the crossing point and ideal alignment is assumed making this a technically challenging device to implement. Even so, and using the best dielectric mirrors now available, this source suffers from flux limitations. Figure 4.4.1 shows the photon energy spectrum in photons/GeV/s for a 1μA electron beam. The highest energy photons in this beam are only 30% of the endpoint energy.

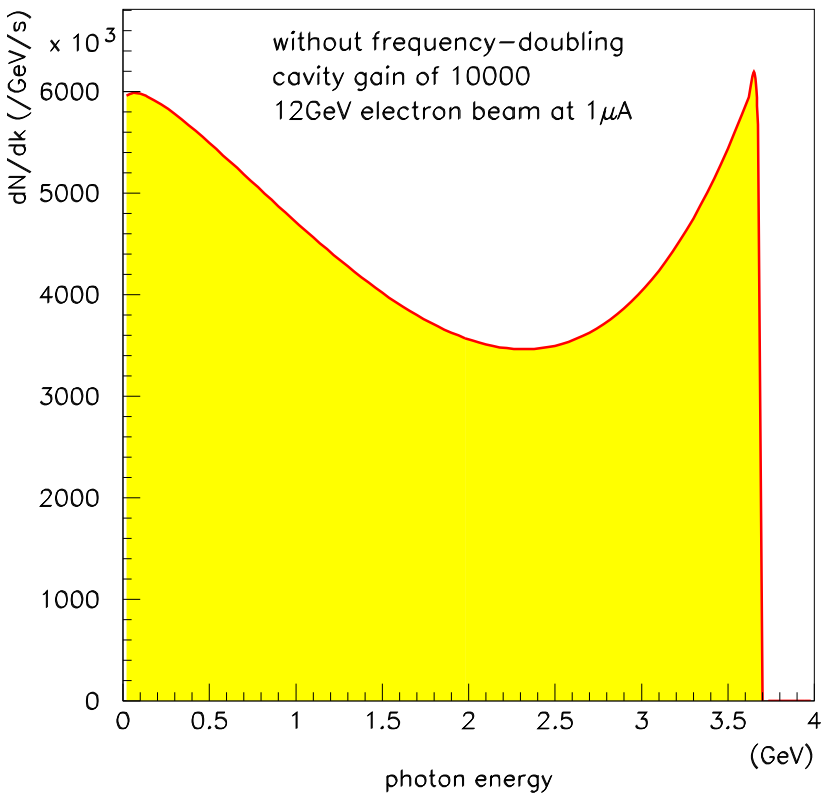

Figure 4.4.1 Photon energy spectrum in a laser backscatter photon beam for a resonant cavity driven by a state-of-the-art pulsed Argon-ion laser operating at 514 nm that is synchronized with the pulse cycle of the accelerator.

Higher energies can be obtained by frequency doubling the laser before injection into the cavity. The spectrum and flux under these conditions is shown in figure 4.4.2. The observed losses in intensity arise from poorer mirror reflectivity at shorter wavelengths, inefficiency of the frequency doubling apparatus and the dropping Compton cross section with increasing photon energy. The endpoint energy is still less than 50% of the electron energy and well below the energy requirements described above, hence, this option is not considered further.

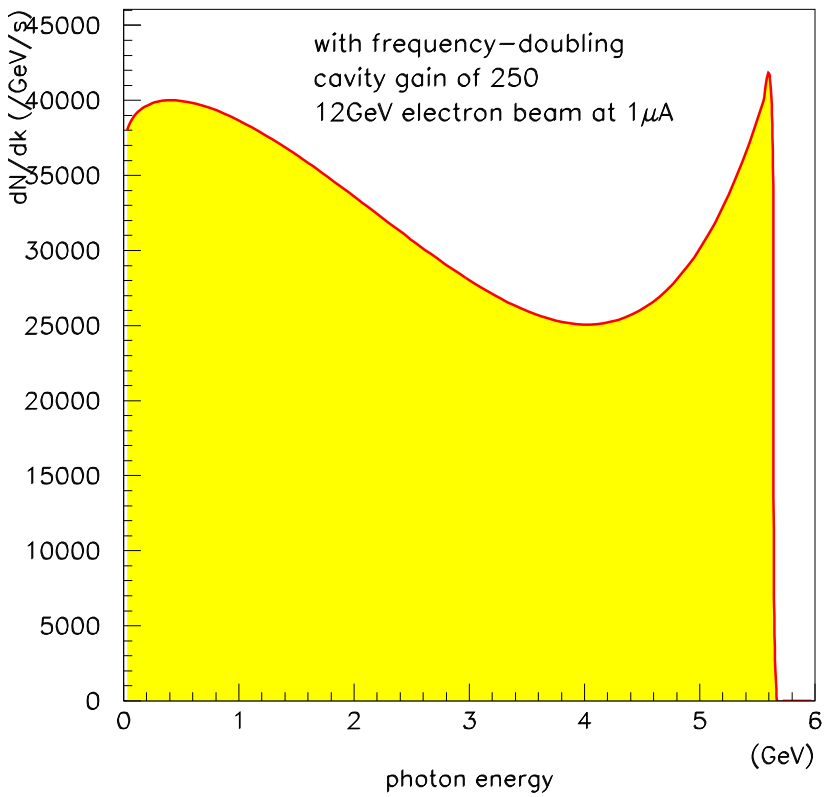

Figure 4.4.2 Same as figure 4.4.1 but using a frequency-doubler cavity tuned to 257 nm.

4.5 Bremsstrahlung beams

Bremsstrahlung offers the only practical way, starting with an electron beam at CEBAF energies, to produce a photon beam with a significant flux in the vicinity of the end point. Bremsstrahlung provides a naturally collimated photon beam with a characteristic angular spread of m/E, which allows the low emittance of the CEBAF beam to be effectively transfered into the secondary photon beam. Detecting the post-bremsstrahlung electron in a spectrometer in coincidence with the final state from photon interactions tags the energy of the incident photon, thereby providing an effectively monochromatic photon beam. The photons can be generated with a significant plane polarization by using a thin oriented crystal in the place of an amorphous or

polycrystalline bremsstrahlung target (radiator), through the process of coherent bremsstrahlung. This polarization is enhanced by collimating the photon beam beyond its intrinsic angular spread, and making up the diminished flux by increasing the electron beam current. As shown below, even in the case of very thin crystals and severe collimation, the electron beam current required to satisfy the needs of this experiment is quite modest compared to what CEBAF can produce, which is why the facility can be located above ground. The experiment does, however, make significant demands on the machine from the point of view of emittance and beam position stability, both areas in which CEBAF has shown outstanding performance. In the following sections it is shown how the electron beam quality at higher energies translates into the quality of the photon beam available to the experiment.

A horizontal plan view of the photon beam line is shown in figure 4.5 with the major components labeled. The electron beam enters the figure from below ground at the left and is bent into the horizontal plane to enter the tagger building. There it passes through two small dipoles to impinge upon the bremsstrahlung radiator. After its exit from the radiator, the electron beam passes into the tagger magnet where the primary beam is bent in the direction of the electron beam dump. The radiator crystal is thin enough that most of the electrons lose less energy in traversing the radiator than the intrinsic energy spread of the incident beam, so apart from some emittance growth from multiple scattering in the radiator the primary beam is simply deflected by the tagger magnet into the dump. Those electrons which lose a significant fraction of their initial energy inside the radiator do so dominantly by emitting a single bremsstrahlung photon. These degraded electrons are bent out of the primary beam inside the tagger magnet and exit the vacuum between the poles of the magnet, passing through air for a short distance to strike the focal plane of the spectrometer. The primary electron beam is contained inside vacuum all the way to the dump. The two dipole magnets shown in the figure downstream of the tagger are there to provide sufficient deflection that the dumping beam is not able to produce any forward-going particles into the experimental hall.

The photons that are produced in the radiator pass through the tagger magnet to exit the vacuum through a thin window in the forward direction. They then pass into a transfer pipe, which may either be evacuated or filled with helium to reduce photon beam degradation due to interactions, and travel to the experimental hall. Just before it enters the hall, the photon beam passes through a system of collimators and sweeping magnets housed inside a shielded vault. The primary collimator is first, defining the part of the photon beam that is allowed to reach the target. Debris from interactions that take place

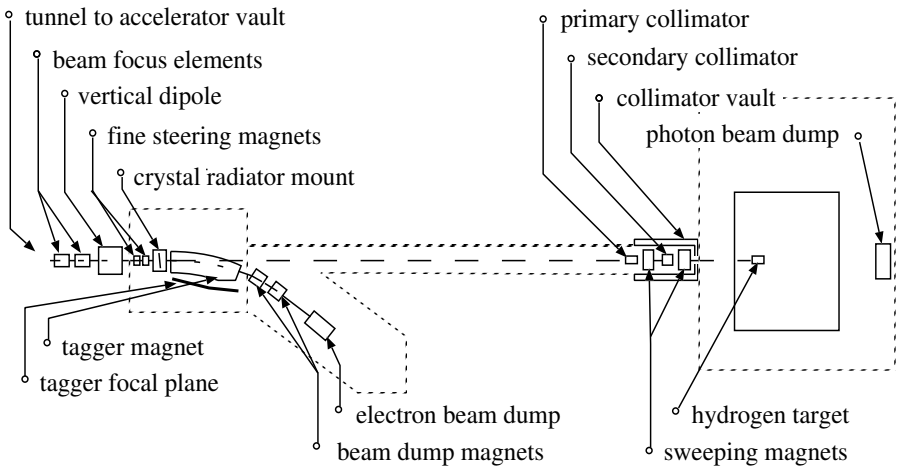

Figure 4.5: Schematic plan view of the photon beam line, shown in the horizontal plane as viewed from above. The objects in this figure are not drawn to scale.

along the inside surface of the collimator forms a halo around the collimated photon beam. The charged component of the halo is deflected away from the beam axis by a dipole "sweeping" magnet just downstream of the collimator. A secondary collimator follows the sweeping magnet to stop the deflected shower particles and block the secondary photons generated from the first collimator. The secondary collimator is of larger diameter than the primary and so sees a reduced rate of secondary interactions on the inner surface of the hole, and what new showers are generated there are cleaned up by a second sweeping magnet and a final collimating aperture, through which the beam passes into the experimental hall. This triple-collimation system was copied from the setup developed at SLAC [98].

The collimated photon beam, now only a few mm in diameter, is delivered to the experimental target. After passing through of order 5% radiation lengths of target, including windows and liquid hydrogen, the photon beam passes through the detector and into the photon beam dump at the back of the hall. The total power in the photon beam is at most 1W in the experimental hall, compared to at most 50W in the collimator vault, and 120kW maximum at the electron beam dump.

4.6 Photon Source

Essential features

The adjective 'coherent' in coherent bremsstrahlung does not indicate that the photons in the beam are in a coherent state, as is light from a laser. Rather it refers to the coherent effect of multiple atoms in a crystal lattice in absorbing the recoil momentum from a high energy electron when it radiates a bremsstrahlung photon. In X-ray spectroscopy one encounters the same thing in the Mosbauer effect, except in that case the chief physical consequence is the disappearance of the recoil Doppler shift. Here the chief consequence is the enhancement of bremsstrahlung at those particular kinematics for which the recoil momentum matches one of the reciprocal lattice vectors of the crystal. Another useful way to view the process of coherent bremsstrahlung is as virtual Compton scattering. To the high energy electron, the atoms in the radiator appear as clouds of virtual photons. For a disoriented radiator material, the virtual photon spectrum is given simply by the atomic form factor, averaged over the different species in the material. If the radiator is a single crystal, however, the atomic form factor gets multiplied by the form factor of the crystal, which in the ideal case looks like a series of delta-functions located at the sites of the reciprocal lattice. In effect, the crystal provides a set of virtual laser beams, each one a standing wave tuned to a specific reciprocal lattice vector. In this view the process of hard bremsstrahlung is seen to be the same as Compton backscattering of laser light. For a more detailed discussion of the physics of coherent bremsstrahlung there are a number of good references

The use of Compton backscattering of laser light as a photon source was earlier noted as ruled out by the limitation of high-power lasers and cavities to wavelengths above $100\mu m$. The characteristic wavelength of the crystal photons is a few Angstroms, three orders of magnitude shorter. In this case, 180° scattering would result in essentially 100% of the electron beam momentum being transfered to the photon in the lab frame. Unfortunately, however, the Compton cross section contains a factor of $(\vec{q} \cdot \vec{p})^2$ where $\vec{q}$ is the virtual photon momentum and $\vec{p}$ is that of the electron, which strongly favors incident photons with $\vec{q}$ nearly orthogonal to $\vec{p}$. With reciprocal lattice vectors pointing in almost every direction, only those nearly perpendicular to the beam contribute appreciably to the scattering rate. This fact applies equally to ordinary bremsstrahlung; in fact, to a first approximation the bremsstrahlung spectrum from a single crystal is the same as from a disoriented radiator. The reason is that, if the sum over crystal momenta were replaced with a continuous integral, one would recover the ordinary bremsstrahlung result for isolated

atoms. Beyond a few unit cells from the origin in reciprocal lattice space, the atomic form factor and kinematic factors become slowly varying on the scale of the lattice spacing, and the sum becomes indistinguishable from the integral. Besides that, the uncertainty principle requires that atoms localized at the sites in a crystal undergo fluctuations about their mean position. This has the effect of attenuating the discrete peaks in the crystal form factor at progressively higher-order crystal momenta, eventually washing them out and filling in the gaps between them, so that the sum deforms smoothly into the integral at high momentum transfer. Hence, the sum over crystal indices that yields the final photon spectrum can be separated into two parts: a discrete sum over a limited set of small crystal indices and an integral over the continuum of momentum transfer values beyond. The latter appears in the coherent bremsstrahlung beam as an ordinary $1/k$ bremsstrahlung spectrum, while the former appears as a set of peak structures superimposed upon it. The $1/k$ continuum, referred to as the incoherent component, is invariant as the crystal is rotated, whereas the coherent peaks change in position and intensity, depending on crystal orientation.

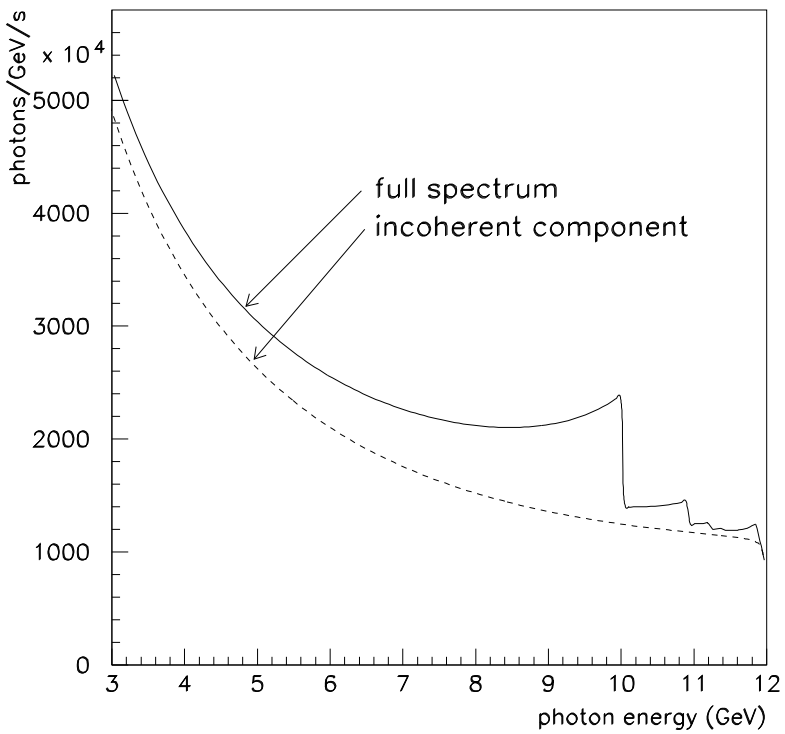

Figure 4.6.1 Coherent bremsstrahlung spectrum, calculated for a diamond crystal radiator $20\mu m$ thick and a 100nA electron beam of 12 GeV energy. Typical values were used for beam emittance and crystal mosaic spread.

A typical coherent bremsstrahlung spectrum is shown in figure 4.6.1. The distinction between incoherent and coherent components in the figure is artificial; it is there to show the part of the spectrum that shifts as the crystal is rotated. The vertical scale in the figure gives the photon rate for the given beam current and crystal thickness. Note that the intensity of the incoherent background is less than what would be obtained with an amorphous carbon radiator of the same thickness, because a part of the momentum transfer integral in the Bethe-Heitler formula has been moved into the discrete sum and contributes to the coherent part. The radiation length of diamond is actually an average over all orientations of the crystal. In the calculation for figure 4.6.1 the leading 400 lattice sites were included in the discrete part of the

calculation, although it can be seen that only two or three of them contribute with sufficient intensity to be individually visible in the spectrum.

4.6.1 Use of collimation

The presence of the large incoherent flux in 4.6.1 presents a significant handicap to a photoproduction experiment. Not only do the low energy photons produce background in the detector, but they diminish the polarization of the beam. The entire beam polarization appears in the coherent component; the underlying incoherent flux only serves to dilute the polarization. There is another difference between the two components that allows them to be separated to some extent. The kinematics of bremsstrahlung confines most of the intensity of the photon beam to forward angles within m/E radians of the incident electron direction. In the lab this is a small angle, but in the rest frame of the electron-photon system it subtends all angles in the forward hemisphere. A peak in the coherent component that corresponds to a single reciprocal lattice vector has two-body kinematics, so there is a well-defined relation between the emission angle and the energy of the emitted photon in the lab: emission at 0° yields a maximum energy photon, with energy decreasing with increasing angle. This accounts for the shape of the coherent peaks in figure 4.6.1, with the sharp right-hand edge corresponding to 0° emission and the tail to lower energies corresponding to scattering into higher angles.

The incoherent component, because it comes from a sum over momentum transfers at all angles, has essentially no correlation between photon energy and emission angle. This means that collimating away all photons beyond some angle $\theta_{max} < m/E$ uniformly attenuates the incoherent spectrum at all energies, whereas it preserves all of the coherent photons from the maximum energy for the given peak down to some cutoff. The kinematic relations for coherent bremsstrahlung are as follows,

$$\theta^2 + 1 = \left(\frac{1-x}{x}\right)\left(\frac{x_{max}}{1-x_{max}}\right) \tag{4.4}$$

$$x_{max} = \frac{2\vec{p}\cdot\vec{q}}{2\vec{p}\cdot\vec{q} - m_e^2} \tag{4.5}$$

where x is the photon energy in units of the incident electron energy and θ is the lab emission angle of the photon relative to the incident electron momentum axis, in units of m/E .

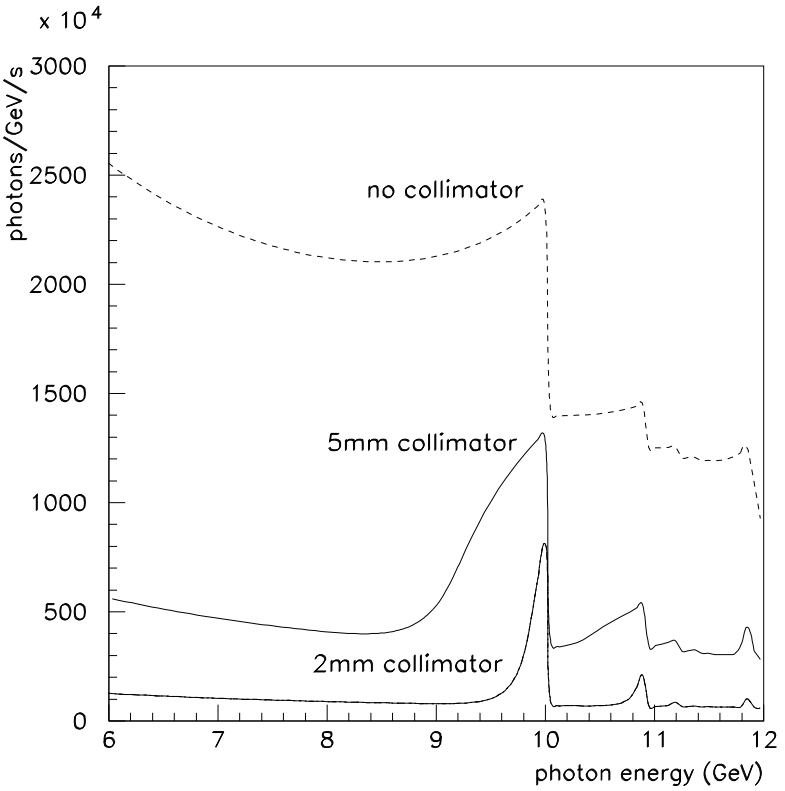

Figure 4.6.2 Coherent bremsstrahlung spectrum, calculated under the same conditions as in figure 4.6.1 , after collimation. The upper curve is the uncollimated spectrum from figure 4.6.1. The middle curve corresponds to a $5mm$ diameter collimator placed 80m downstream of the radiator, or approximately 0.75 m/E in collimator half-angle. The lower curve corresponds to a $2mm$ collimator in the same position, approximately 0.30 m/E in half-angle.

The effects of collimation are demonstrated in the calculated spectra shown in figure 4.6.2. First, note that the collimation angles are very small, which requires a long flight path of order 100m in order that the collimator can be larger than the intrinsic beam spot size, otherwise the collimator is cutting in transverse coordinate instead of in angle. This distance is, in fact, a sensitive function of the electron beam emittance from the machine, and must be increased in inverse proportion to the beam emittance if the effectiveness of

collimation is to be maintained. This issue, along with the associated demands placed on beam alignment and position stability, are taken up in more detail in the following section on the electron beam line.

Second, note that the cut imposed on the coherent peak by collimation does not produce a perfectly sharp edge as would be expected from two-body kinematics. This is because a collimator cuts on radius at some fixed position which translates into a cut on emission angle only in an approximate way, and is why the curves in figure 4.6.2 are labelled by their collimator size and distance individually rather than their ratio which is the approximate collimation angle. Multiple scattering by the electron in the radiator prior to emission and beam spot size and divergence are the major contributors to the error involved in interpreting a collimator as a cut in emission angle. All of these effects have been incorporated into the analytical calculation of the yields from a collimated coherent bremsstrahlung source that has been used in preparing this report. Crystal imperfections, which amount to an intrinsic spread in the direction of the incoming virtual photon, are also accounted for in the calculation.

Third, note that the relatively weak collimation at $5mm$ reduces the incoherent background without significantly affecting the coherent flux near the maximum, and thereby almost doubling the polarization of the beam at the peak relative to the uncollimated case. Further reducing the collimator diameter continues to narrow the peak and reduce the incoherent flux relative to the peak, albeit at some cost in peak intensity. In the case of the $2mm$ collimator, the peak polarization is essentially that of the coherent component alone. Although almost all of the photon beam energy is being absorbed at this point at the collimator, provided there is adequate shielding around the collimator the necessary flux in the collimated beam can be made up by increasing the electron beam current. The peak in figure 4.6.2 for a $2mm$ collimator contains 1M photons/s for an electron beam current of 100nA, which could be increased by a factor of up to 100 in the facility being planned for HALL D .

Fourth, note that the rate seen in the focal plane of the tagging spectrometer corresponds to the dotted curve in figure 4.6.2 , regardless of the collimation. This means that collimating the bremsstrahlung beam increases the rate in the tagger focal plane relative to what is seen at the detector. For example, running with the $2mm$ collimator and 10^7 photons/s in the main coherent peak implies according to figure 4.6.2 a rate of 250MHz per GeV in the focal plane. Under these conditions, only a small part of the focal plane is in coincidence with the events of interest, which limits the rate of accidental tags to a reasonable level. For maximum flexibility, the full upper 25% of the tagging range must be designed to handle rates as high as this.

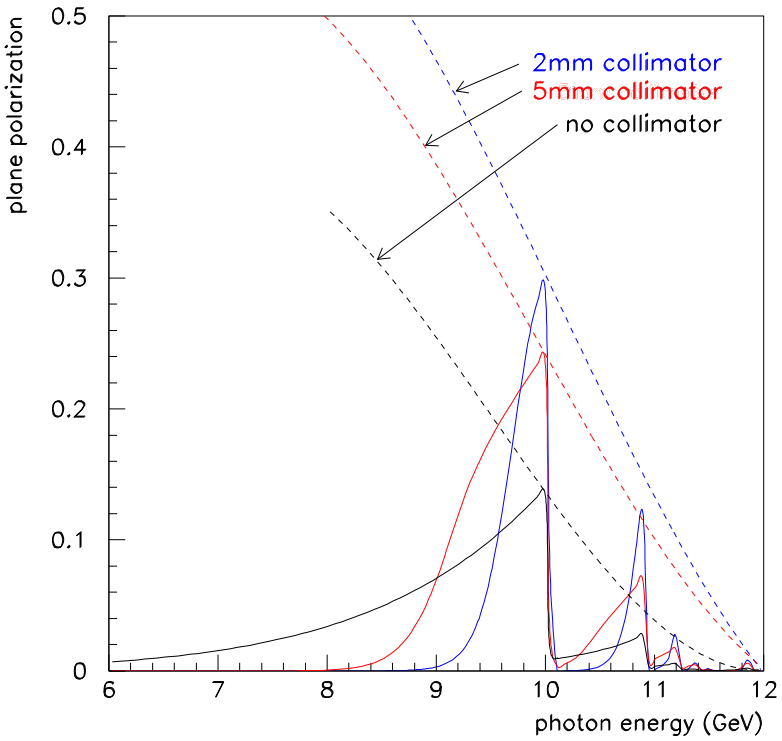

Figure 4.6.3 Plane polarization of the coherent bremsstrahlung beam, calculated under the same conditions as in figure 4.6.2. The dashed lines indicate the trajectory of the peak polarization as the peak energy is swept across the focal plane by rotating the crystal.

The net polarization of the beam under different collimation conditions is shown in figure 4.6.3. The dashed curves show how the maximum polarization in the peak varies as the peak energy is changed by rotating the crystal. The polarization in all cases is zero at the endpoint. Without collimation it rises as $(k-E)^2$, one power coming from the intensity of the coherent peak relative to the incoherent component going to zero linearly at the endpoint, and the other from the intrinsic polarization of the coherent photons also behaving like $(k-E)$ near the endpoint. Collimation allows one to essentially isolate the coherent component, so that the polarization available to the experiment rises from zero at the endpoint in a linear fashion. The dashed curves in figure 4.6.3

crystal	best reciprocal vector	$P/P_{diamond}$
diamond	2,-2,0	1.00
beryllium	0,0,2	0.86
boron	2,0,8	0.38
silicon	2,-2,0	0.19
Be_2C	2,2,0	1.10

Table 4.1: Figure of merit of various materials that might be used as a coherent bremsstrahlung radiator. This table is reproduced from Table 2 in H. Bilokon *et al.*

demonstrate this point.

4.6.2 Choice of radiator

The ideal radiator would be a layered structure with a strong transverse fields that alternate between layers spaced about $50nm$ apart, thus simulating the standing wave in a cavity driven by a 15eV laser. While it is possible to construct ordered materials with unit cells as large as this, the self-shielding of atoms means that beyond the atomic length scale the residual fields are comparatively weak. Hence heterogeneous structures are not viable for use as a coherent radiator. Since the strong fields inside a solid are revealed at the atomic scale, the first requirement for a good radiator is that the unit cell be compact and closely packed. The best radiators are those with the smallest unit cells because these provide the best match between the atomic and the crystal form factors. This match is best for the light elements, and essentially prohibits the effectiveness of any materials heavier than carbon. An extensive survey of possible radiator materials is presented in Ref. [99]. In table 4.1 is shown the figure of merit that those authors report for favored crystalline materials. The figure of merit is the product of the atomic times the crystal form factor evaluated at the leading peak, normalized to the value for diamond.

Table 1 shows that the list of viable materials for a crystal radiator is relatively short. Silicon would be an excellent choice from the point of view of price and fabrication, but unfortunately it is far inferior in terms of performance. Beryllium carbide is not a material that is familiar to the crystal growth industry, and nothing is known at present concerning its suitability for the growth of single crystals of large area. In general compound materials are

more susceptible to radiation damage than are pure elements, which would argue in favor of diamond and beryllium metal. These two materials are comparable in terms of their performance. Most of the experience to date with coherent bremsstrahlung has been with diamond radiators. Extensive expertise for handling large diamond crystals exists within the gem industry. High quality monocrystals of $6mm \times 6mm$ and as thin as $100\mu m$ were obtained at SLAC [98]by cleaving from a facet of a large gem. This was made possible by a contact that existed at the time with a friendly insider in the gem business. It is not clear at the present whether this success could be repeated in a cost effective way, and so it is important to consider beryllium as an alternative radiator material.

Beryllium metal is widely used in industry, being preferred for its high strength-to-weight ratio and robustness, in addition to its transparency to X-rays. Thin films of high-purity beryllium are routinely produced for vacuum window applications, which use some of the same vacuum deposition techniques that would be used for the growth of single crystals. As a radiator material, beryllium is distinguished as the metal with the highest Debye temperature, around 1400°K . The Debye temperature measures the temperature at which the thermal motion of the atoms in the lattice reaches the level of the zero-point motion due to their confinement in the lattice, as dictated by the uncertainty principle. A high Debye temperature indicates a stiff crystal lattice, in which the atoms have little liberty to move and so have large momentum fluctuations, as dictated by the uncertainty principle.

A high Debye temperature is important for a bremsstrahlung radiator material for three reasons. First, the cross section for coherent bremsstrahlung from a discrete crystal momentum vector $\vec{q}$ contains a factor $e^{-q^2/4M\theta_D}$ which reflects the fact that position fluctuations of atoms in the lattice diminish the coherent effect. This factor is near unity for the low-order crystal momenta provided that θ is sufficiently large. Second, the Debye temperature is, roughly speaking, a measure of the stability of the crystal structure and hence its readiness to form as a single crystal and to survive significant doses of radiation. Third, the radiator material will inevitably be heated by the beam, and will normally operate in vacuum well above the ambient temperature. A high Debye temperature means that there is a large range of temperatures over which the material may operate without degraded performance as a crystal radiator. The Debye temperature of diamond is about 2200° K. Past experience has shown that diamond meets all of the requirements for a good crystal radiator. There is good reason to believe that beryllium would function almost as well at substantially less cost, but this remains to be proved.

4.6.3 Crystal thickness

The range of permissible thicknesses for a crystal radiator is bounded both from above and below. It is bounded from above by multiple scattering of the electron beam as it passes through the radiator, which causes the divergence of the incident beam to grow, thereby enlarging the photon beam spot on the collimator face and degrading the degree to which collimation discriminates against the incoherent component in favor of the coherent part. It is bounded from below by the fact that the crystal must be of some minimum thickness in order to achieve the full coherent gain. In the calculation of the coherent bremsstrahlung process one begins by assuming an infinite crystal, although practically it is presumed to mean only that the crystal is large compared to the some characteristic scale. It is important to identify what the characteristic scale is in this problem in order to know how thin one can make the crystal without hurting performance. In the analogous case of the Mosbauer effect, one can estimate the number of atoms participating in the collective absorption by looking at the emission time of the photon (lifetime of the radiating transition) and asking how many nuclei lie within the envelop of the photon wave packet. In the coherent bremsstrahlung process, the lifetime of the radiating system is given in the lab system by the uncertainty principle and by how far the electron energy deviates from its on-shell value between absorbing the virtual photon and emitting the real one. The latter quantity is almost exactly given by q_z , the virtual photon momentum component along the incident electron axis, which means that the electron travels a distance $\lambda = \hbar c/q_z$ during the interaction. For a given coherent peak at normalized energy x in the photon spectrum, the coherence length is given by

$$\lambda = \frac{2e(1-x)}{xm^2} \tag{4.6}$$

in units of $\hbar c$. From this simple argument one sees that the coherent gain goes linearly to zero at the endpoint, a result that is borne out by the full QED calculation. One also sees that the lower limit on crystal thickness imposed by the coherence length depends upon both the electron beam energy and the photon energy. For a 12 GeV beam energy and a 6 GeV coherent photon the coherence length is $18nm$, or about 50 unit cells for diamond. This shows that the coherence length does not impose a practical limit on how thin the radiator should be.

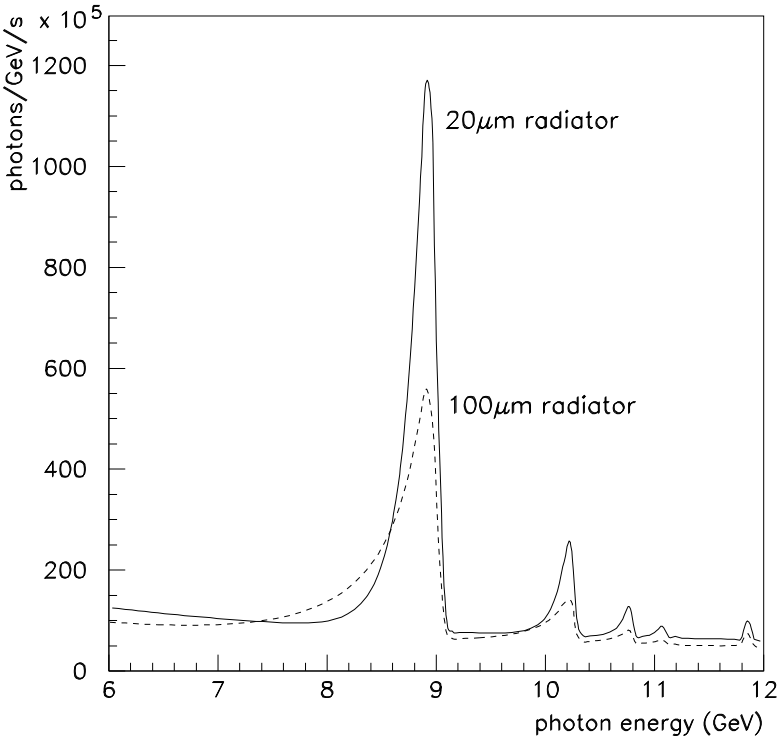

Figure 4.6.4 Collimated coherent bremsstrahlung spectrum from a 1A electron beam at 12 GeV using diamond radiators of two different thicknesses. The calculation assumes a $2mm$ collimator located 80m from the radiator, and typical values for beam emittance and crystal quality.

The effects of multiple scattering are best presented by showing the calculated spectra for various radiator thicknesses. The diamond radiators used at SLAC were cleaved at approximately $100\mu m$ and then milled down to about $50\mu m$ using ion bombardment. In figure 4.6.4 is shown the photon spectrum for a $20\mu m$ and a $100\mu m$ radiator to demonstrate the effect. The $100\mu m$ spectrum is scaled down by a factor of 5 to facilitate the comparison. The calculation assumed a $2mm$ collimator located 80m downstream of the radiator. The loss in normalized intensity with the thicker radiator, as well as the broadening of the left edge of the peak, is due to the enlarging of the photon beam spot on the collimator face from multiple scattering of the electron beam in the

crystal prior to radiation. A $100\mu m$ diamond crystal is roughly 10^{-3} radiation lengths thick. It is reasonable to run with as thick a radiator as is permitted by multiple scattering considerations, in order to keep the beam current to a minimum and prolong as much as possible the lifetime of the crystal.

4.6.4 Crystal mount

It has already been shown that in order to achieve appreciable coherent gain the crystal must be oriented so that the coherent peaks appear well below the end point. Eqn. 4.5 then implies that the orientation must be such that the crystal momentum dotted with the beam momentum be of order m^2 . Given a p of 12 GeV and q of 10KeV, this requires that the two vectors must be within $100\mu r$ of perpendicular to each other and that, within a range of angles of that order, the coherent peak sweeps out nearly the full range in x from 0 to 1. Hence both the incident beam angle and the angle of the crystal radiator must be stable at the level of a few μr in order to have a stable photon beam for running. At least one of the two must be adjustable in steps that are small compared to $100\mu m$ in order to have the ability to position the coherent peak at the desired energy. These requirements are most simply achieved using a precision two-axis goniometer. Commercial devices of this type exist with step sizes as small as required for this application. With two-axis remote control the crystal can be reoriented in a matter of minutes to produce a coherent beam of any desired energy and in either vertical or horizontal plane polarization modes.

Thermal effects in the crystal mount and small variations in the beam tune from the accelerator make long term stability and reproducibility more difficult to achieve than adequate controls for the initial setup. For this reason it is important that there be sufficient diagnostics present to monitor the crystal orientation relative to the beam. This diagnostic is provided by the rates in the tagger focal plane counters. From figure 4.6.1 it is clear that the critical angle between the beam and the crystal, as well as the quality of the crystal, are accurately reflected in the position and sharpness of the coherent edge in the focal plane rate profile. Better than simply monitoring the critical angle, the tagger profile provides a direct look at the photon beam spectrum prior to collimation. This means that there is no need for an absolute alignment of the crystal and goniometer to this level of precision, because only relative accuracy is required. The second angle is non critical, typically of order a degree, and does not need to be monitored. If conditions require it, a feedback system could be put in place to correct for drifts seen in the tagger focal plane profile by periodically adjusting the goniometer setting within predefined limits. This

would involve a slow control system, and does not need to be designed in advance.

4.6.5 Crystal quality and lifetime

There are two considerations that fall under the heading of crystal quality. The first respects the quality of the original crystal, and the second is with regard to degradation from radiation damage. In the calculation of the coherent bremsstrahlung spectrum a perfect single crystal was assumed, but even the very best crystals have some dislocations and other defects. Besides locally disrupting the regularity of the crystal, these defects impose stresses which produce small ripples in the crystal planes. If these ripples were amplified, the surface of a crystal would appear like a mosaic of planar regions with approximately parallel surfaces. The scale of deviations from planarity across the face of a single crystal is termed the *mosaic spread* of the crystal. The mosaic spread contributes in the same way as beam divergence to the smearing in the exact energy-angle relation for coherent photons. This quantity, which can be measured directly using specialized optical equipment, was poorly known by the SLAC group for their diamonds, but they believed them to be better than $50\mu r$. This is the value that is used in the calculations for this report.

The SLAC group found that the performance of their diamonds had degraded considerably after a total charge of 3 Coulombs had been accumulated over a surface of $6mm \times 6mm$ in area. They were able to recover a better performance for the damaged crystals by putting them through an annealing process. This translates to five weeks of running, or about a two months of real time at $1\mu A$ of current, before the crystal would need to be removed for treatment. A small set of radiators of different thicknesses would accommodate a run plan that includes some running with maximum polarization, i.e. narrow collimation, a thin radiator and microamps of beam current, and running the rest of the time with a thicker radiator, less beam current and more modest collimation.

4.7 Electron Beam Line

The possibility of a collimated coherent bremsstrahlung photon source in HALL D depends in a critical way on having a low-emittance electron beam from CEBAF at 12 GeV. It is inevitable that, as the energy of the machine is increased, there will be some growth in the emittance from the steep rise in synchrotron radiation. However, the plans for the upgrade of the accelerator include mea-

sures that substantially control and offset these effects, albeit at substantial cost for some of them. Such investments require careful justification in terms of the physics research that they enable. The purpose of this section is to show the connection between the parameters of the beam at 12 GeV and the quality of the photon beam that can be produced from it for the HALL D . The connection between the photon source performance and the physics HALL D is planning to do is made elsewhere in this document. Any decision regarding the final configuration of the machine involves a cost/benefit analysis that goes beyond any one experimental hall. However, we see an important link between the HALL D project and the upgrade of CEBAF to 12 GeV beams. In the following sections the mutual implications of the two projects are explored in detail.

4.7.1 Beam emittance requirements

Widely different machine performance figures can be projected from the present performance to operation at 12 GeV, depending upon what other upgrades accompany the addition of high-gradient cavities to the linacs. Rather than decide on some favorite configuration and base the HALL D design on that, we have decided to take the present parameters for operation at 6 GeV as a starting point, and examine how the photon beam is affected as the emittance gets worse. For this starting point, a value of $10mm \cdot \mu r$ is taken for the beam emittance at the entrance to the bremsstrahlung radiator. The definition of emittance used here is the area of the 2σ ellipse in the space of displacement from beam center vs divergence from the beam axis. Because synchrotron radiation occurs mainly in the horizontal plane inside the accelerator, the emittance values in x are generally larger than those for y. The calculations presented here assumed the same value for vertical and horizontal emittance, taking $10mm \cdot \mu r$ as an effective average between the two. The longitudinal emittance, displacement along the beam from bunch center vs deviation from nominal beam energy, is not a critical parameter for HALL D . Energy resolution of 25MeV f.w.h.m. for a 12 GeV beam or better is required in order to make full use of the resolution planned for the tagger.

The place where transverse emittance plays a critical role is at the photon collimator. For optimum effectiveness in collimation it is important that the electron beam spot at the collimator position be as small as possible. The electron beam does not actually reach the photon collimator, being bent into the dump shortly after the radiator by the tagger magnet. But considering the optics of the electron beam as if the tagger dipole were switched off, the electron beam at the radiator can be projected forward 80m to form a vir-

tual image on the collimator entrance plane. The position and size of this spot gives the the definition of the 0° emission angle for the photons. If this spot is small compared to the collimator aperture and is centered then the collimator does its job of removing photons with emission angle beyond the collimator half-angle. However, if the virtual spot is larger than the aperture then the collimator serves only to reduce the intensity of the beam and does not discriminate between coherent and incoherent beam components.

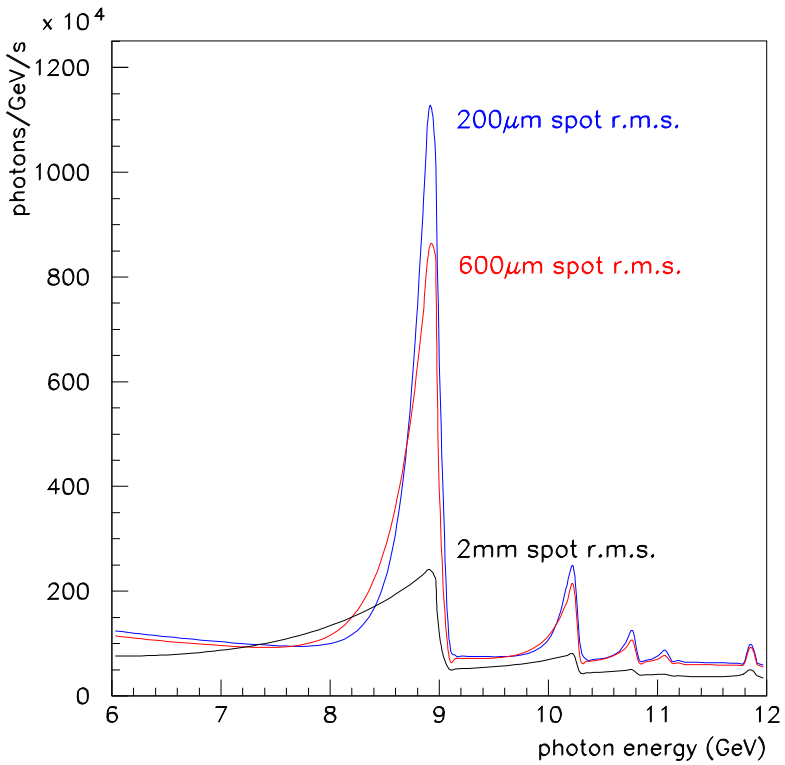

Figure 4.7.1 Coherent photon spectrum for three different values of the r.m.s. size of the virtual electron beam spot on the collimator. A $2mm$ diameter collimator 80m downstream of the radiator was used.

Note that this analysis does not place any specific limits on the size of the beam at the radiator. The beam spot can and should be larger there to avoid burning a hole in the radiator. For the SLAC coherent bremsstrahlung source the beam at the radiator was $6mm$ in diameter and focused to image a $2mm$

spot at the collimator positioned 91m downstream of the radiator. The focus ensures that photons emitted near zero degrees, even those far from the beam axis at the radiator, will pass near to the axis at the collimator position and so be seen at the experimental target. The virtual electron beam spot is not the same as the actual photon beam spot on the collimator, which is concentric with the former but larger.

Figure 4.7.1 shows how the collimated photon spectrum depends upon the r.m.s. size of the virtual electron beam spot on the collimator. When the spot size becomes comparable with the collimator aperture then the collimation is rendered ineffective, and the photon spectrum and polarization revert to their uncollimated values. The connection between focal spot size and beam emittance can be seen by noting that an upper bound is placed on the angular divergence of the beam at the radiator in order to maintain the same incidence angle with respect to the planes of the crystal for all electrons in the beam. Practically, the divergence does not broaden the coherent peak provided that it is kept below the mosaic spread of the crystal. A conservative value for the allowable angular divergence δ in the electron beam at the radiator would then be $20\mu m$. Taken together with a $200\mu m$ r.m.s. spot size at the focus, this leads to an emittance of $50mm \cdot \mu r$ at 12 GeV. The $600\mu m$ spot size in figure 4.7.1 corresponds to an emittance of $150mm \cdot \mu r$ and the $2mm$ spot to $0.5mm \cdot mr$.

4.7.2 Electron beam line optics

Taking the electron beam out of the machine and focusing it onto a $200\mu m$ spot requires some optics in the beam line leading up to the radiator. Translating the beam emittance into a r.m.s. values for the beam radius and divergence requires the knowledge of the β parameter, defined as the ratio of the r.m.s. beam size at the focus to its angular divergence. The β varies along a beam line wherever there are focusing elements. When it comes out of the accelerator, β is large, of order 1km, corresponding very highly parallel beam. In order to focus a beam of emittance $50mm \cdot \mu r$ down to a r.m.s. size of $200\mu r$, the β must be reduced from 1km down to 10m by the use of focusing elements. The focusing must be done in both x and y axes separately to achieve the desired result, and must be accomplished by elements located along the transfer line from the accelerator vault to the surface. The strong focusing requirement significantly complicates the design of the transfer line, and will require careful study. It may be simpler to achieve a lower emittance beam and run with weaker focusing than to require a fine tuning in the transfer line in order to squeeze a larger emittance beam all the way down to its theoretically minimum

focus.

Not only must the virtual electron spot be small enough to fit within the collimator aperture, but it must also be centered on the aperture and stable. In order to maintain a stable beam position on the collimator, the SLAC experiment [98] installed a segmented halo detector just upstream of the collimator and operated an active feedback loop to a vertical and horizontal pair of dipoles located just upstream of the radiator. From that distance a bend of only $10\mu r$ results in a shift of $1mm$ at the collimator position. Hence the beam alignment feedback system is effectively decoupled from the crystal orientation controls. Small deflections that are necessary to keep the beam centered on the collimator do not produce appreciable walk in the beam-crystal angle, and by using a goniometer to control the latter, the former can be operated in a feedback circuit that operates independent of the photon source energy controls. The experimental program in parity violation at Jefferson Lab has already designed a position stabilization circuit that is able to keep the beam position steady to within $20\mu m$ over a 20m lever arm. A less sophisticated version of this circuit should be a part of the collimated photon source for HALL D .

4.7.3 Electron beam dump

The electron beam is dumped in the horizontal plane, as shown in figure 4.5. The horizontal bend offers several advantages over dumping the beam into the ground. The tagger magnet is easier to support if it sits in the horizontal position. It is also easier to mount and service the focal plane in this position. The dump itself is also more accessible in case it needs to be serviced. An above-ground dump also affords the possibility of running parasitic beam dump experiments that do not interfere with the operation of the experimental hall. It also allows for a possible future implementation of secondary meson beams in HALL D , which is the subject of the next section.

The primary design requirement for the electron beam dump is that it have a sufficiently high capacity to handle beams of the highest intensities foreseen for HALL D . A 250KW design would provide a a healthy margin for 12 GeV operation and sufficient capacity to handle as much as $10\mu A$ in the planned 24 GeV era. The present design calls for a 15° bend in the horizontal plane from the axis along which the electron beam enters the tagger building to the direction it exits into the beam dump. The total 15° bend is divided about equally between the tagger magnet and one or two dipoles. The dipoles were added as a cheaper alternative to enlarging the tagger magnet. It is considered that 15° provides sufficient space for shielding that the experimental hall can

be effectively isolated from the dump.

4.7.4 Possibility of hadron beams

The physics program planned for HALL D centers around photoproduction as a source of both conventional and exotic mesons, and emphasizes the interest of these studies as follow-up to the experimental progress that has been achieved over the last five years using pion and antiproton beams at hadron facilities. The possibility of using high energy electrons from CEBAF to generate secondary meson beams at some time in the future has arisen in HALL D discussions, however, mainly for two reasons. The first is that the detector that is being planned for HALL D is of a general-purpose design. At present very little is known concerning high energy meson photoproduction, aside from the fact that it is a prolific source of vector mesons and possibly of vector hybrids. The detector package described in this report is capable within the first two years of operation of collecting as much data on photoproduction as presently exists for any production mode, including pion production. Thus the possibility is very real that after a relatively short running period in HALL D , there might be reason to turn again to pion or kaon production methods to examine states that are suppressed or missing in photoproduction. The second reason is that one of the most successful programs ever carried out in meson spectroscopy was the LASS experiment, which used a secondary kaon beam generated using 20 GeV electrons from SLAC to study kaon production. The fact that the same detector could be used for both kinds of beams, and that some mention has already appeared of energies even higher than 12 GeV at Jefferson lab, warrants a brief summary of these discussions in this report.

The LASS experiment took 3-4 kaons per pulse and about 120 pulses per second during normal operation, for a total of 300-500 kaons/s. Averaged over the duty cycle of the accelerator, this beam rate was achieved with an average electron beam current of $7\mu A$. They used rf separation to obtain a nearly pure kaon beam, which required a beam line of 150m, rather long compared to the mean decay distance of about 40m for a 10 GeV K^- . A beam line of a similar design but without rf separation would fit into the HALL D design, with the production target just before the electron beam dump and the secondary beam being bent by a chicane onto the same axis as the photon beam. The 80m space between the tagger building and the experimental hall would allow room for one or more gas Cerenkov counters that could be used in the place of rf separation to tag the different species in the beam. Using the same apertures as were used for LASS would give in excess of 1000 kaons/s and about a factor of 60 more rate in pions for a $10\mu A$ electron beam. The secondary particles

have a broad energy spectrum that peaks around half of the electron beam energy. While these rates are not high compared with what is available at a hadron machine, the availability of a high-quality detector designed for this kind of physics makes it worthwhile to carry out the design of the experiment and beam lines keeping this possibility in mind.

4.8 Tagging Spectrometer

4.8.1 Magnet

The tagging spectrometer being envisioned for HALL D is of a similar design to the one currently in use in Hall B. The radius of curvature has been adjusted to follow the path of the primary 12 GeV beam at a low field of only 1T. Operation at low field during the 12 GeV era allows the spectrometer to be used in the case of further energy upgrades, all the way up 24 GeV beam energy, simply by increasing the field in the dipole. Under this design the spectrometer is able to tag the top 50% of the photon spectrum (corresponds to the low momentum region in recoil electron momentum) independent of the energy of the primary beam. The choice to restrict the tagged region to 50% or more of the endpoint reflects the priority of the experimental program for running at the highest possible photon energies.

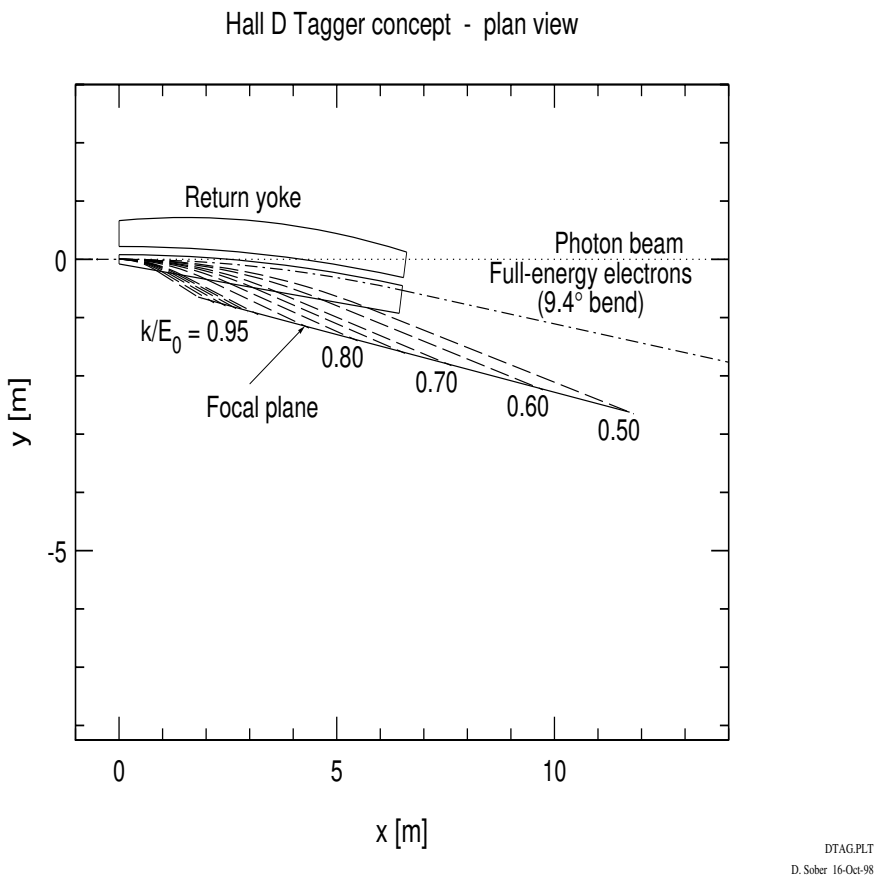

Figure 4.8.1 A plan view of the tagging spectrometer from above, showing the path of the primary beam and the trajectory of post-bremsstrahlung electrons of various recoil momenta.

4.8.2 Focal-plane hodoscope

A plan view from above the tagger and focal plane is shown schematically in figure 4.8.1. The two primary requirements for the design of the focal plane hodoscope is that it have sufficient segmentation to provide the required photon energy resolution and that it be able to handle the high rates associated with coherent bremsstrahlung with collimation. Detector studies indicate that 0.1% r.m.s. photon energy resolution is required in the most demanding case, in order to make maximum use of the resolution of the detector to reconstruct incomplete events using the missing mass technique. Assuming that the energy

of the incident electron beam is defined at the 0.1% level, a focal plane of non-overlapping counters each subtending a 25MeV bite of the total 6 GeV momentum tagged at 12 GeV electron beam energy provides the required tagged photon energy resolution. About 240 individual counters are required to completely instrument the tagger focal plane under these conditions. The detectors themselves can be little rectangular pieces of plastic scintillator no more than $2-3cm$ on a side and lined up with just enough overlap to prevent electrons from slipping between them without detection.

The counters subtending the upper 25% of the photon energy spectrum must be equipped with special bases and electronics to be capable of sustaining rates as high as 10MHz when running in collimated coherent mode. The part of the focal plane outside the coherent peak may as well be turned off for running in collimated mode because only the photons in the vicinity of the coherent peak are polarized. Given that one has a measurement of the energy of the photon from the tagger in any case, the primary reason for collimating the coherent beam is to enhance the polarization.

Chapter 5

The Detector

5.1 Overview

The physics goals of the HALL D project require a full partial wave analysis of kinematically identified exclusive reactions producing mesons. The decay products of produced mesons must be identified and measured with good resolution and with full acceptance in decay angles. In many cases, the decays of mesons involve a chain of particle decays. The HALL D detector must therefore be hermetic with 4π coveragee with the capability of measuring energies of neutral particles (γ, π^0, η) and momenta of charged particles with good resolution. Particle identification is also required.

The HALL D detector will be built in two stages. The STAGE 1 detector will be used with incident photons in the energy range from 6 to 8 GeV - assuming that HALL D and beamline are in place before the 12 GeV energy upgrade.

Figure 5.1 is a schematic representation of the proposed STAGE 1 HALL D detector. The STAGE 1 detector has a *solenoid region* and a *forward region.* The individual subsystems are discussed in more detail below.

The STAGE 2 HALL D detector will likely have the same *solenoid region* since the kinematics of the particles produced as part of the recoil system does not change appreciably with the increased beam energy. However, in STAGE 2 the forward particles will have higher energies and momenta requiring a modification of the *forward region.* A dipole magnet will be added with more forward tracking. The forward calorimetry will also need modification.

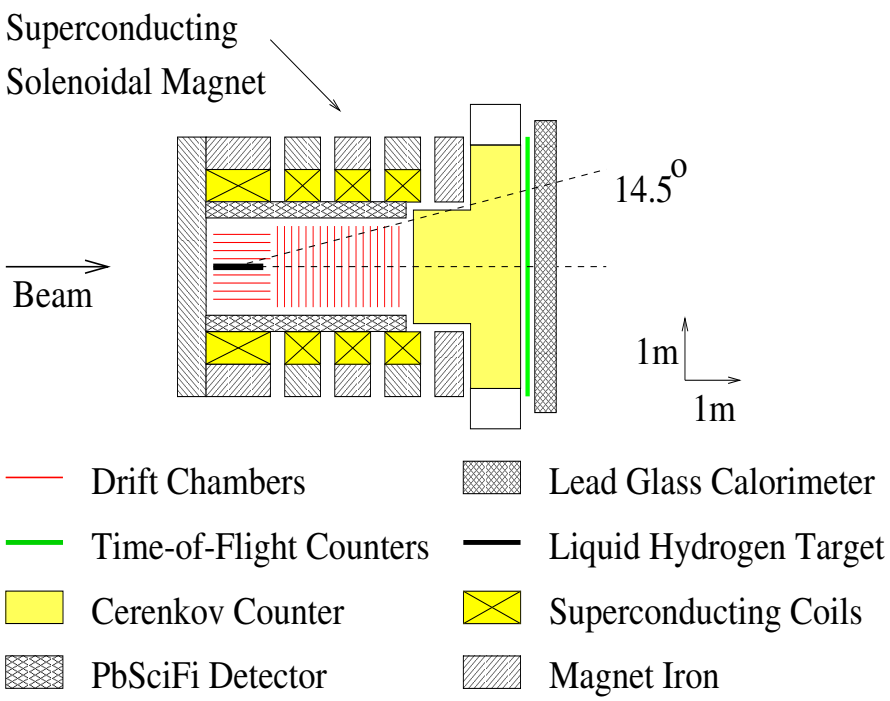

Figure 5.1: An overview of the STAGE 1 HALL D detector. The major subsystems are labeled and are discussed individually in the text.

5.2 The solenoid region

5.2.1 Superconducting solenoid

The *solenoid region* detectors will reside in a large superconducting solenoidal magnet – the LASS/MEGA magnet. This magnet was built for the Large Aperture Superconducting Solenoid Spectrometer (LASS) and SLAC and later transferred to LANL for use in the MEGA experiment. It will be transferred to Jefferson Lab for use in HALL D . This magnet has been previously described[100] and some relevant portions of that description are quoted below. Table 5.1 summarizes some of the parameters of the magnet.

Inside diameter of coils	80 inches
Clear bore diameter	73 inches
Overall length (iron)	183 inches
Inside iron diameter	116 inches
Outside iron diameter	148 inches
Coil-to-coil separation	11 inches
Total iron weight	200 tons
Central field	25 kG
Conductor current	1800 A
Total stored energy	36 MJ
Inductance	22 H
Total helium volume (including reservoir)	5,000 liters
Operating heat load (liquid He)	30 liters/hour
Operating heat load (liquid nitrogen)	30 liters/hour
Cool-down time	2 weeks
Copper to superconductor ratio	20:1 (grade A) 28:1 (Grade B)
Total conductor length	117,600 feet
Total conductor weight	29,000 lbs
Turn on time	20 minutes
Turn off time (normal)	20 minutes
Axial load per coil due to magnetic forces	280 tons

Table 5.1: Summary of characteristics of the solenoid in the LASS configuration

The LASS solenoid magnet provides a 22.4 kG magnetic field parallel to the beam direction. The inside diameter of the magnet is 185 cm and its overall length is 465 cm.

The fudicial region within the bore is 320 cm in length and 75 cm in radius. Within this region the field homogeneity is better than $\pm$ 3.1 %. Along the beam axis the homogeneity improves to $\pm$ 0.9 %.

The solenoid is constructed of four separate superconducting toroidal coil-Dewar units [101] in order to permit intercoil placement of planar proportional chambers. A 200 ton iron flux return path, similarly split in four places surrounds and supports the coil assemblies. A common liquid helium reservoir is located atop the solenoid providing the gravity feed of the liquid to the coils.

The superconductor used is a stabilized, composite, twisted, multi-filament wire of niobium-titanium. The wire is made by soldering the superconductor composite between two copper strips to form a rectangular cross section 0.763 x 0.533 cm. The coil is wound directly on the liquid helium vessel inner cylinder wall. As the coil is wound, a 0.20 inch thick stainless steel support band, and a mylar insulating strip are wound along with it for mechanical support and insulation. Cooling by the liquid helium is accomplished from the edges. Each of the four toroidal windings has its own predetermined number of turns, the configuration being selected for optimum central field homogeneity consistent with the requirement of the intercoil gaps and the large downstream end opening.

The liquid helium vessel is surrounded by a liquid nitrogen cooled radiation shield and this assembly centered in the vacuum tank by a circumferential series of tie bolts designed for minimum conductive heat flux to the helium bath. Radial centering and support are achieved by four low conductance hangers arranged in a spiral pattern. Various tie rods and hangers were instrumented with stress bolts to measure the tremendous forces on the assembly caused by the magnetic fields.

The inductance of the coil is 25 Henries, and the magnet is run at 1600 Amperes. The liquid helium volume is $\approx$ 5000 liters and the heat load is $\approx$ 60 l/hour. Refrigeration is supplied by two C.T.I. refrigerators, one a nominal 100 watt refrigerator, the second nominally 70 watt. Either refrigerator alone is capable of supplying the liquid helium required by the magnet while operating

under current. However, when operated together at half speed they can handle the magnet and supply additional liquid to a reserve tank. This conservative design, both of the refrigeration system and of a superconductor itself, has produced a stable, reliable and safe superconducting magnet.

5.2.2 Target

A 30 *cm* liquid hydrogen target will be used. It will be contained in the same vacuum jacket containing the photon tagger radiator and constructed of low mass materials. A 5 *cm* diameter will entirely contain the collimated photon beam and will allow adequate space between the hydrogen vessel and the innermost detector element for insulation, a vacuum pipe and any plumbing and wiring required to instrument the target. Safety is, of course, a very serious concern for any hydrogen target and we will be consulting with the appropriate lab groups early on in the actual design of the target.

It may be desirable, during some running of the experiment, to use compact, nuclear targets. For this reason it is anticipated that the target will be removable from the apparatus. Is is assumed that it will be inserted from the upstream end of the solenoid through the hole in the upstream flux return.

5.2.3 Start counter

Immediately surrounding the target is a scintillator hodoscope. In the STAGE 1 detector, this device serves as a trigger element only, analogous to the CLAS *start counter*. A coincidence between this counter and the tagger loosely defines an interaction. To minimize rates in the phototubes of this counter, it must be segmented, currently some small number (≤ 16) of segments is anticipated. The segments are similar to the staves of a barrel. A simple OR of the segments defines a hit in this device. The light from the scintillator segments is transported out of the target region on fiber light guides through the flux return on the upstream end of the solenoid to shielded photomultiplier tubes. A discriminator, a TDC and simple OR logic complete the instrumentation of the counter.

For the STAGE 2 detector, the target hodoscope will also serve as a tracking device used to provide accurate position information very close to the target. It will continue to be used as a trigger element but with greatly upgraded logic. A possible design could be a scintillating fiber array detector with three logical layers (one parallel to the beam and two stero layers). The exact dimensions of the fibers will be optimized for both position resolution and sufficient light

output for trigger purposes, currently, 1 mm fibers are assumed. The detector is located between 5.0 and 5.5 cm radially from the target. The axial extension is taken to be 80 cm. Six actual layers of 1 mm fibers between 5.0 and 5.5 cm leads to a total of roughly 2000 fibers. *Sea of gates* coincidence logic will determine hit multiplicity in the counter for use in the prompt trigger.

The trigger section of this design report has additional discussion of the STAGE 1 and STAGE 2 start counters.

5.2.4 Cylindrical tracking chambers

Proceeding radially outward from the start counter, the region between $r = 15$ to $r = 60$ cm is occupied by the central drift chambers, CDC. These are the primary chambers for reconstructing large angle tracks. They will be built from 1 cm carbon fiber straw tubes and read out by 250 MHz (or faster) flash ADC's and arranged in 22 layers for a total channel count of ≈ 5200 cells. An $r - \phi$ resolution of 200 μm is the design requirement and measurement of the z-coordinate is through stereo layers with a resolution of 500 μm. Drift times will be measured by fitting the digitized output pulse and extrapolating to the inital time of the pulse. Time resolution better than the sampling interval is anticipated, although, with a 4 ns sampling interval, 200 μm resolution is achieved if the drift velocity is 50 $\mu m/ns$. Integration of the fitted pulse shape allows dE/dx information to be obtained for use in particle identification.

5.2.5 Barrel calorimeter

The region in the solenoid most radially distant from the beam axis ($r = 65$ to $r = 90$ cm) contains the barrel calorimeter. This device detects photons, is a trigger element and serves as a time of flight device for the particle identification system. It consists of 48 azimuthally segmented sectors of lead/scintillating fiber (Pb/SciFi) electromagnetic calorimeter. It is read out at both ends of the solenoid with flash ADC's and pipelined TDC's. The large fiber to lead ratio gives excellent energy and position resolution. Multiple samples of particle arrival time allow good resolution when this device is used in the TOF system. The fast resopnse time allows the device to be used as a trigger device. The barrel calorimeter is discussed in more detail below.

5.2.6 Forward tracking system

In the STAGE 1 detector, high momentum, forward going tracks are reconstructed using planar drift chambers inside the solenoidal field. Two types of

chambers are assumed, one very near the beam, denoted as the beam vertex trackers (BVT), with another type radially farther from the beam denoted as the forward drift chambers(FDC). The BVT elements exist in a high rate environment and so have small cell sizes and correspondingly small drift times. The FDC have larger 1 cm cells. Both types of chambers will provide space point measurements with 200 μm resolution transverse to the beam axis. Space point measurement is achieved by using six layers of wires each with (u, v) coordinate cathode strip readout.

5.3 The forward region

5.3.1 Forward tracking system

Because higher beam energies (up to 12 GeV) are used in STAGE 2 of the experiment higher momentum forward going tracks are expected. As the track momentum increases the resolution for these tracks degrades. For this reason, the STAGE 2 detector will be augmented with forward, planar drift chambers before and after a dipole magnet. This allows excellent[1] momentum resolution for the highest momentum tracks.

The difficulty is that the dipole spreads e^+e^- pairs created by interactions of photons with matter upstream into a "sheet of flame" in the bend plane of the dipole. Two solutions to this problem are being considered:

- Ignore them. The problem can be avoided by deadening the small strip of the detector illuminated by these e^+e^- pairs. The acceptance is, of course, zero in this region
- Shield them from the dipole field. This could be achieved with a multilayer ferromagnetic flux exclusion tube extending from the exit of the solenoid through the dipole. Since the pairs experience a greatly reduced field, they are not bent to large angles thus eliminating the *sheet of flame*. This approach reduces the acceptance for the smallest angle tracks.

Both approaches will be considered and a decision reached as to which acceptance effect is least harmful after the data from STAGE 1 is evaluated.

5.3.2 Čerenkov counter

A heavy gas Čerenkov counter will be used as part of the particle identification system. The range of momenta to be covered is similar to that encountered by

[1] ($\Delta p/p = 0.75\%$) was achieved by LASS in a similar configuration, see [100]

the LASS experiment so their experience is directly applicable. The Čerenkov counter envisioned for HALL D will be segmented into three rings each further segmented into 12 azimuthal sectors. The device will be located in the downstream end of the solenoid and will protrude from it by about 1 meter. The heavy gas used by LASS (Freon-114) is no longer produced but an environmentally acceptable alternative (C_4F_{10}) exists. The index of refraction of this gas is such that π/K separation is possible over the energy range 2.6 to 9.5 GeV.

5.3.3 Forward calorimeter

An existing calorimeter is ideally suitable for use in HALL D . The Brookhaven National Laboratory Experiment 852 lead glass detector has an aperature and cell size well suited to this application. Its energy and position resolution are adequate for the spectroscopy envisioned in this report. It consists of ≈ 3000 $4 \times 4 \times 45$ cm^3 lead glass modules. Each is instrumented with a type FEU-84-3 Russian made 30 mm phototube. Computer controlled Cockroft-Walton bases have been designed for use with these tubes and have been extensively prototyped in JLab experiment 94-016 (Radphi).

5.4 Barrel calorimetry

Electromagnetic (EM) calorimetry in the barrel region of the HALL D detector covers the approximate polar angular range $14^\circ < \theta < 138^\circ$. Exact specifications depend on the final size and location of the liquid hydrogen target, the effective thickness of the calorimeter and its readout scheme on both the upstream and downstream ends of the solenoid. It will be positioned immediately to the inside of the solenoid which determines the outer radius to be 90 cm. This allows 2 cm for supports and cabling. The outer surface area is approximately $23m^2$. A device this large intercepts a considerable number of gammas from a myriad of reactions as presented in the physics chapter, and therefore represents a key component of a hermetic system. The size also implies that it will be a challenge to build and instrument at reasonable cost.

We briefly review some of the important aspects of having full EM calorimetry in the stage 1 design of the spectrometer. First, many of the reactions to be studied can be produced with the photoproduction of an object, X, recoiling against either a proton *or*, for example, a Δ. The ability to detect the π^0 from the Δ decay allows selection of exclusive final states, a requirement for partial wave analysis. Second, many reactions feature π^0s or ηs in the final states.

Excellent energy and position resolution of these neutral mesons is critical to complete reconstruction of these states. Finally, for all charged modes, it is essential to be able to veto on neutral missing energy. Here, nearly hermetic coverage is critical. For selected triggers, neutral vetoes are relatively easy to implement.

5.4.1 Design considerations

The inside clear bore radius of the LASS solenoid is 92.7 cm. Allowing for mechanical supports, the outer calorimeter envelope is restricted to 90 cm. In order for the tracking elements inside the magnet to perform optimally, the barrel calorimeter must be thin, perhaps no more than 25 cm. The length of the solenoid is 4.5 m. These geometrical constraints lead to a long, narrow tube-like design. In this geometry, readout is easiest at the ends where space exists. However, at the upstream end, a magnetic field-shaping plug interferes with simple design ideas. We believe we can overcome these with modifications to the plug. The choice of readout device must bear in mind the considerable magnetic field (2.5 kG) inside the bore and the rapidly varying fringe field at the ends. Conventional photomultiplier tubes (PMTs) will work only outside of the solenoid and even there considerable attention must be paid to shielding.

Following the Oct. 1998 HALL D Workshop at FSU, a number of candidate calorimeter designs were being considered. The leading design utilizes scintillating fibers embedded in a lead matrix to make a relatively high-resolution sampling calorimeter. Advantages include speed, cost, ease of readout, and the fact that it is based on a proven technology. The second, "high-end" option is based on the idea to use the relatively new Lead Tungstate ($PbWO_4$) crystals which are being developed as the main EM calorimetry for the CMS experiment at the LHC. They offer superior resolution, good light output and the density to make them very compact. Unfortunately, the very large channel count probably makes this option cost-prohibitive. Naturally, a hybrid design, mixing two technologies for different parts of the polar coverage is possible. The very forward angles ($\theta < 14^\circ$) are assumed to be covered by the existing Lead Glass Detector (LGD) recovered from the BNL E852 experiment and restacked to meet the geometrical acceptance criteria for HALL D.

5.4.2 Pb/SciFi barrel calorimeter

Scintillating fibers embedded in a matrix of lead or other high-Z materials have been used in calorimeter design and operation for more than a decade. The ratio of the active scintillator to the passive high-Z material, as well as

the diameter of the fibers can be tuned to enhance resolution, to determine the radiation length, and to achieve uniformity in the electromagnetic to hadronic response (the e/h ratio). For high-resolution EM performance, the Jetset detector developed at Illinois [102] was the first designed specifically to optimize EM resolution. The recipe produced a detector comparable to lead glass at a considerably lower cost and with approximately half the radiation length. It utilizes 1 mm fibers spaced uniformly (close packed) on specially grooved plates of lead. The lead is alloyed with $3-6\%$ antimony to provide mechanical stiffness. Tooling was developed in order to groove the plates. A second machine was built to guide spools across stacks of the plates taking care to properly align each fiber spool with a groove in the lead. The assembly of a module consisted of a repeated layering of fibers and plates, all held together with an optical epoxy. A finished module was machined into final shape, polished and outfitted with a plastic lightguide for readout.

The resolution for an array of prototypes subjected to electrons in the range from $300-1500$ MeV was represented by the function $\sigma/E = 6.3\%/\sqrt{E}$ with a negligible constant term. In the Jetset Forward Calorimeter, the beam entered nearly parallel to the fiber direction. The energy resolution was also measured with tagged photons below 100 MeV and improved to $\approx 5\%/\sqrt{(E)}$; the detector gave a resolvable signal all the way down to 20 MeV. Of moderate interest to HALL D is the fact that this type of detector has been proven to be radiation hard up at about 0.5 Mrad. [103]

In Jetset, a Barrel Gamma Veto detector with thickness $6X_0$ was made in a barrel-like fashion with 24 modules of length 80 cm each forming the sides of the barrel. Here, with the interaction point centered in the barrel, gammas entered the modules at normal incidence for polar angles of 90 deg. For other angles, the detector is effectively thicker. Our design for HALL D follows this concept but would be a full $12.5-15X_0$ thick at normal incidence and considerably longer. Realization of these changes fortunately can be based on the KLOE calorimeter at DAΦNE where they have been building a device of this length with an even larger inner diameter. The KLOE collaboration has taken the development of Pb/SciFi a step further. They have developed better tooling for production of long grooved plates, have pushed the technology for excellent, bright fibers with long attenuation lengths, [2] and have produced prototypes with excellent energy and timing characteristics. [3]

[2] A discussion of the properties of the fibers considered for KLOE can be found in [104]. Included are measurements of propagation velocity, attenuation length, light yield and decay time.

[3] Energy, time and position resolutions of a 2.03 meter KLOE prototype calorimeter are discussed in [105].

We intend to follow much of this development and therefore describe some of the aspects below.

Like Jetset, the KLOE design utilizes 1 mm scintillating fibers embedded in a lead matrix with a fiber to lead to glue ratio of approximately 48 : 42 : 10. Prototype modules, 2 m in length, were produced with PMT readout at both ends. An excellent energy resolution parameterization of $\sigma/E \approx 4.4\%/\sqrt{E}$ was found. In the actual experiment the module length increases to 4.3 m (which is similar to HALL D) and therefore special efforts were made to develop and test scintillating fibers with very long attenuation lengths. Tested fibers had attenuation lengths in the range from $2.3 < \Lambda < 3.2m$ which is far superior to the average Λ of 1 m for the Jetset fibers. This aspect of the design is critical because it there exists a significant coupling between the position of impact (essentially the polar angle, θ) and the interpreted energy. Light collected on each end must be corrected for attenuation length before conversion to energy units.

An important feature of these detectors is the signal risetime and overall duration. Because fast plastic scintillator [4] is used, integrated signal time can be kept below 100 ns with shorter times possible if deemed necessary for rate considerations. At the expected maximum luminosity, no problems are anticipated. With risetimes of a few ns, excellent timing can be expected for each of the PMTs involved in collecting the light from a shower. Time differences from the two ends produces the z coordinate of the hit. Because we will use an array of PMTs on each end (segmented in azimuth and depth), redundant measurements are made of the z coordinate. These measurements of z correspond to different average radii and therefore help to establish the angle of the incoming photon.

The fractional volume of scintillator in the detector naturally makes it efficient for responding to ordinary charged pion or kaon tracks. The mean light collection time of the two readout ends can be used to determine the particle time-of-flight (TOF). TOF coupled with the track length and momentum then yields particle mass. Therefore, this design for a Barrel Calorimeter can be expected to play an important role in the overall barrel PID scheme. In the KLOE design, timing of better than 100 ps was achieved. The same can be expected for HALL D as long as PMTs and discriminator chains are selected carefully.

In order to form grooved plates and construct modules 4.5 m long, we plan to study the KLOE tooling development. We would either replicate or borrow their successful devices. This proof of principle gives us confidence that the

[4] Decay times are 2.0 - 2.5 ns

daunting mechanical task can be handled. For HALL D, we expect to build 48 modules each 4.5 m in length and 20-25 cm deep. Variants on this theme are being considered; in particular, half length modules with intermediate readout will be studied. The readout scheme takes advantage of the fact that all fibers run parallel to the axis of symmetry of the solenoid and therefore all light piped to the ends of the modules retains its azimuthal and radial information. The polished ends of the detectors can be coupled with multiple independent lightguides. In the figure shown below, 6 segments are suggested. This gives a minimum of 96 independent azimuthal slices, each with three dual- ended readouts at varying depths. The transverse size of a module is approximately 4 cm at impact. Because the EM showers spread across these azimuthal boundaries, algorithms for finer positioning of the shower are employed. In Jetset, one finds a typical weighted position resolution of $\delta x \approx 5mm/\sqrt{E}$). For the HALL D design, this would lead to an azimuthal resolution of $\approx$ 10 mrad. Using the z position resolution of approximately 1 cm obtained from time difference leads to a polar angular resolution at 45° of $\approx$ 8 mrad. As the design of the barrel calorimeter is further refined, it will be important to keep these numbers balanced.

In figure 5.2 several views are shown for the barrel calorimeter including an overall perspective, a side view of one module, and an end view indicating how a single module could be segmented with six independent readouts. In this design, there are $48 \times 6 \times 2 = 576$ PMTs. Each requires ADC, TDC, discriminator, HV and cabling. A calibration system is critical and can be based in part on the use of Nichia blue LEDs glued directly to a short lightguide stub at the end of each module. An LED driver system is also required. The choice of ADC and TDC systems depends on the overall readout coordination for HALL D . To estimate costs, we can we can imagine packaging typical of existing Fastbus-based systems with 64 or 96 channels per unit.

5.4.3 Crystal options

An upgrade to the barrel calorimeter plans illustrated above would be a true pointing geometry "crystal" type design, with independent readout for individual modules. The difficulty for HALL D is that the area to be covered is very large and the radial constraints are severe, limiting consideration to materials with radiation lengths shorter than 1.7 cm. (25 cm divided by 15 X_0 minimum depth) For high-rate situations, pileup is an important consideration so that only fast scintillating materials are useful. Further, the high-field environment of the solenoid prohibits conventional PMT use requiring the use of scintillating materials.

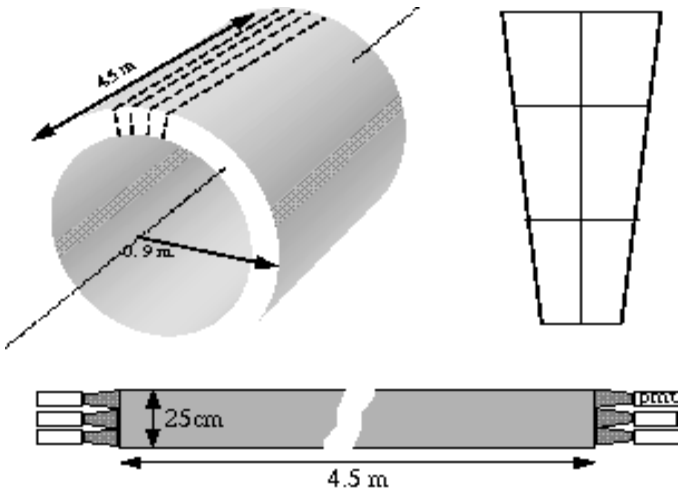

Figure 5.2: Sketch of Barrel Calorimeter made from bars of Pb/SciFi material. (a) perspective view; (b) closeup of end with suggested readout segmentation for one of 48 bars; (c) side view showing approximate locations of PMTs.

A candidate material is Lead Tungstate which features a compact radiation length of 8.9 mm and has excellent energy resolution, typically $\sigma/E = 2.8\%/\sqrt{E} + 0.45\%$. If the very large transverse dimension of 6 cm is assumed for an individual cell of a calorimeter of this type approximately 6000 crystals will be required for full barrel coverage (23 m^2 divided by 0.0036 m^2 per cell) Due to a large demand for such crystals for the LHC, a major Russian fabrication facility has been established so that the crystals are, in principle, available. However, the per channel electronics cost is increased by a factor of 10 to approximately \$9M. We take this to be prohibitive and so do not intend to pursue this option further.

5.5 Tracking chambers

The configuration of charged tracking devices within the solenoid has been studied to optimize the acceptance and momentum resolution. Several of these designs are shown schematically in Figure 5.3 with rough geometrical parameters given in table 5.2. The studied designs contained different mixes of cylindrical, large–angle forward and small–angle forward tracking devices, as well as varying the position resolution of these devices.

All devices in these designs are subject to the constraint that there maxi-

System	*Radius*		*Length*		*Resolution*	
	r_{min}	r_{max}	z_{min}	z_{max}	$\sigma_{r\phi}$	σ_z
Design a						
VTX	5.0 cm	5.5 cm	−90.0 cm	−10.0 cm	1000μm	*stereo*
CDC	15.0 cm	60.0 cm	−100.0 cm	0.0 cm	200μm	500μm
FDC	10.0 cm	60.0 cm	20.0 cm	320. cm	200μm	*fixed*
BVT	3.50 cm	13.0 cm	20.0 cm	330. cm	200μm	*fixed*
Design b						
VTX	5.0 cm	5.5 cm	−90.0 cm	−10.0 cm	1000μm	*stereo*
CDC	15.0 cm	60.0 cm	−100.0 cm	50. cm	200μm	500μm
FDC	10.0 cm	60.0 cm	110. cm	350. cm	200μm	*fixed*
BVT	3.50 cm	13.0 cm	30. cm	330. cm	200μm	*fixed*
Design c						
VTX	5.0 cm	5.5 cm	−90.0 cm	−10.0 cm	1000μm	*stereo*
CDC	15.0 cm	60.0 cm	−100.0 cm	100. cm	200μm	500μm
FDC	10.0 cm	60.0 cm	110. cm	350. cm	200μm	*fixed*
BVT	3.50 cm	13.0 cm	30. cm	330. cm	200μm	*fixed*
Design d						
VTX	5.0 cm	5.5 cm	−80.0 cm	10.0 cm	1000μm	*stereo*
CDC	15.0 cm	60.0 cm	−100.0 cm	140. cm	200μm	500μm
FDC	10.0 cm	60.0 cm	150. cm	350. cm	200μm	*fixed*
BVT	3.50 cm	13.0 cm	85. cm	335. cm	200μm	*fixed*

Table 5.2: A summary of the tracking chamber parameters. The z values under *Length* give the smallest and largest z of the combined system. The z resolution for the *cdc* comes from 500μm cathode strips on the inner and outer shell, and $\pm 6°$ stereo layers. The VTX chamber is expected to have z resolution through stereo layers. The z resolution of the planar chambers is assumed to be given by there orientation in space.

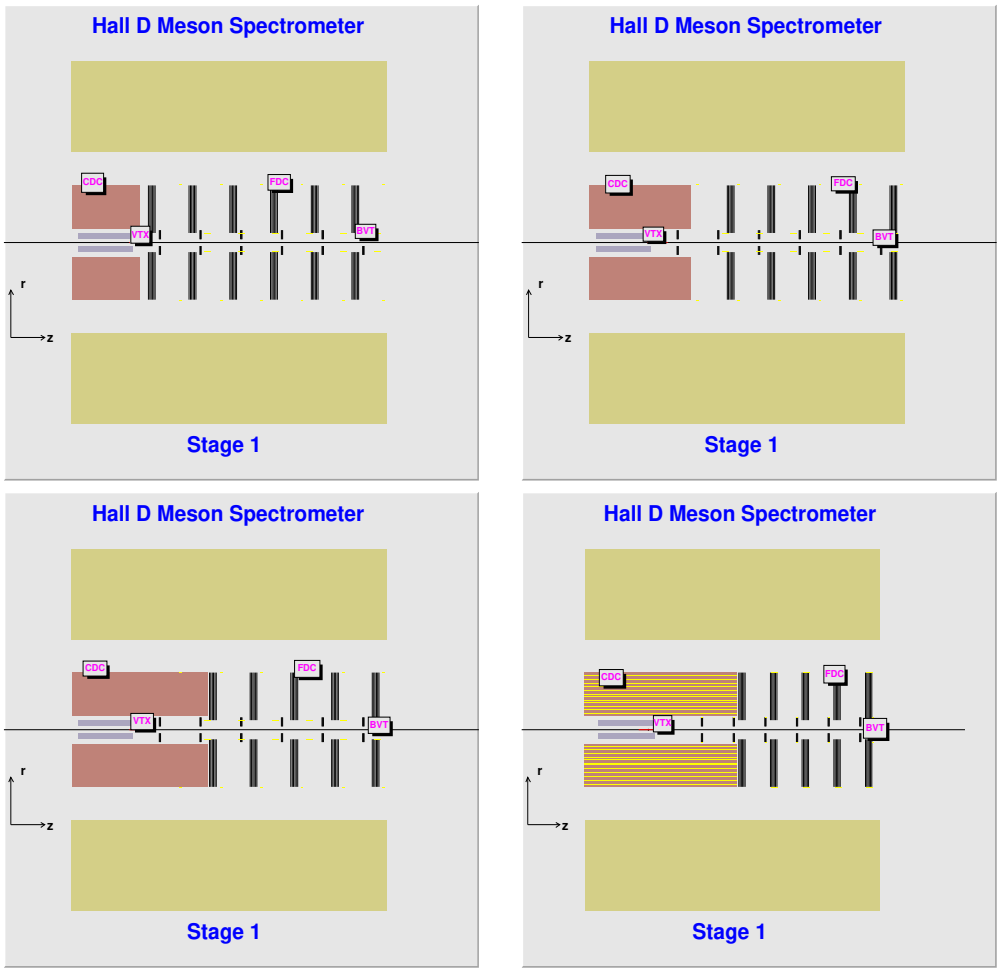

Figure 5.3: The Stage 1 tracking elements. CDC is a cylindrical drift chamber, VTX is a vertex chamber with fast trigger capabilities, BVT are cylindrical drift chambers close to the beam line, and FDC are forward planar drift chambers.

mum radius does not exceed 60.0 cm (92.0 cm bore minus 32.0 cm for barrel calorimetry, detector supports, and cabling).

The solenoid field determines the physically measurable quantities, and hence, the momentum resolution. The transverse momentum, $p_\perp$ and the *dip–angle* λ, ($\lambda = \frac{\pi}{2} - \theta$), are measured from the curvature of the tracks and their initial direction. The total momentum and the longitudinal momentum are then obtained from these as $p_{total} = p_\perp \sec\lambda$ and $p_{||} = p_\perp \tan\lambda$. The accuracy of the $p_\perp$ measurement is completely dominated by the r–ϕ resolution of the tracking chambers, while the λ measurement relies on an accurate measurement of both z and the distance traveled.

In figure 5.4 is shown the distribution of charged particles in p versus θ space for both $E_\gamma = 6$ GeV and $E_\gamma = 10$ GeV. The events are $\gamma p \to Xp \to K^+K^-\pi^+\pi^-p$ where the X has masses between 1.7 GeV/c^2 and 3.2 GeV/c^2. Table 5.3 summarizes the maximum total momentum as a function of angle for both photon energies.

θ [°]	p_{max} [GeV/c]	
	$E_\gamma = 6$ GeV	$E_\gamma = 10$ GeV
20°	3.00 GeV/c	5.00 GeV/c
50°	1.00 GeV/c	1.50 GeV/c
70°	0.50 GeV/c	0.50 GeV/c
100°	0.25 GeV/c	0.25 GeV/c

Table 5.3: Maximum total momentum as a function of angle for both E_γ of 6 and 10 GeV.

From the plots in figure 5.4, we observe several important features which drive the design of the detector. In particular, particles that come out at angles larger than 90° have momenta less than 200 MeV/c. The measurement of these particles is made easy by their lower momenta, but complicated by the fact that they will tend to spiral up in the magnetic field. In order to measure these slow particles accurately, good z–resolution will be needed near the target. Additionally, these particles will not make it to any time of flight system. The only particle identification will come from a dE/dx measurement. On the other hand, we do not need good tracking resolution for fast particles in this region. Next, most events have at least one particle moving in the forward direction at high momentum. In figure 5.4 **c** and **d** are shown the momentum versus angle for the most forward particle in each event. Good tracking will be needed as close to the beam line as possible.

With regard to spiraling tracks, figure 5.5 shows p versus θ for spiraling

tracks. Tracks which fall above the hyperbolic curve cannot spiral in the 60 cm radius region containing tracking chambers. Below the hyperbola are a series of approximately horizontal lines. Tracks below these lines spiral the number of times indicated. Based on the p versus θ distributions in figure 5.4, it can be easily seen that most tracks at angles larger than 50° will always spiral in the detector.

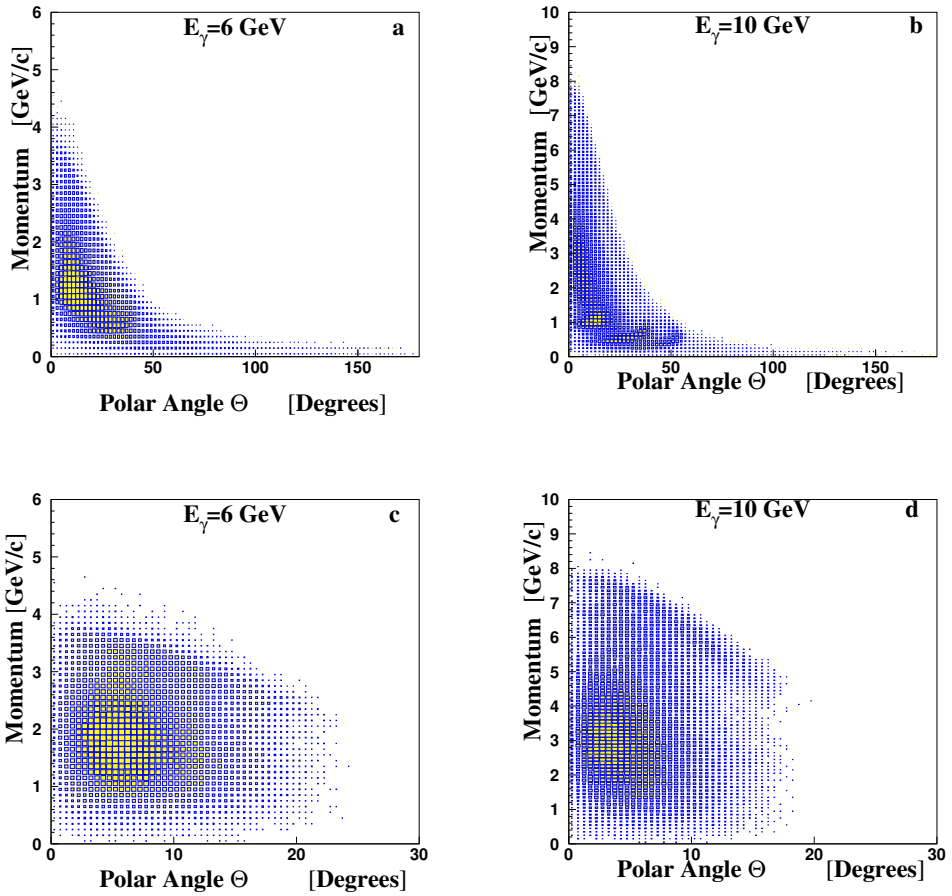

Figure 5.4: Momentum versus polar angle for all charged particles in $\gamma p \rightarrow K^+K^-\pi^+\pi^-p$ data sets. Figures **a** and **b** are the distributions for all particles for $E_\gamma = 6$ GeV and E_γ=10 GeV respectively. Plots **c** and **d** show momentum versus angle for the most forward particle in both cases.

In the stage one design, we have considered a series of tracking layouts as shown in figure 5.3. The elements are broken into four systems whose rough

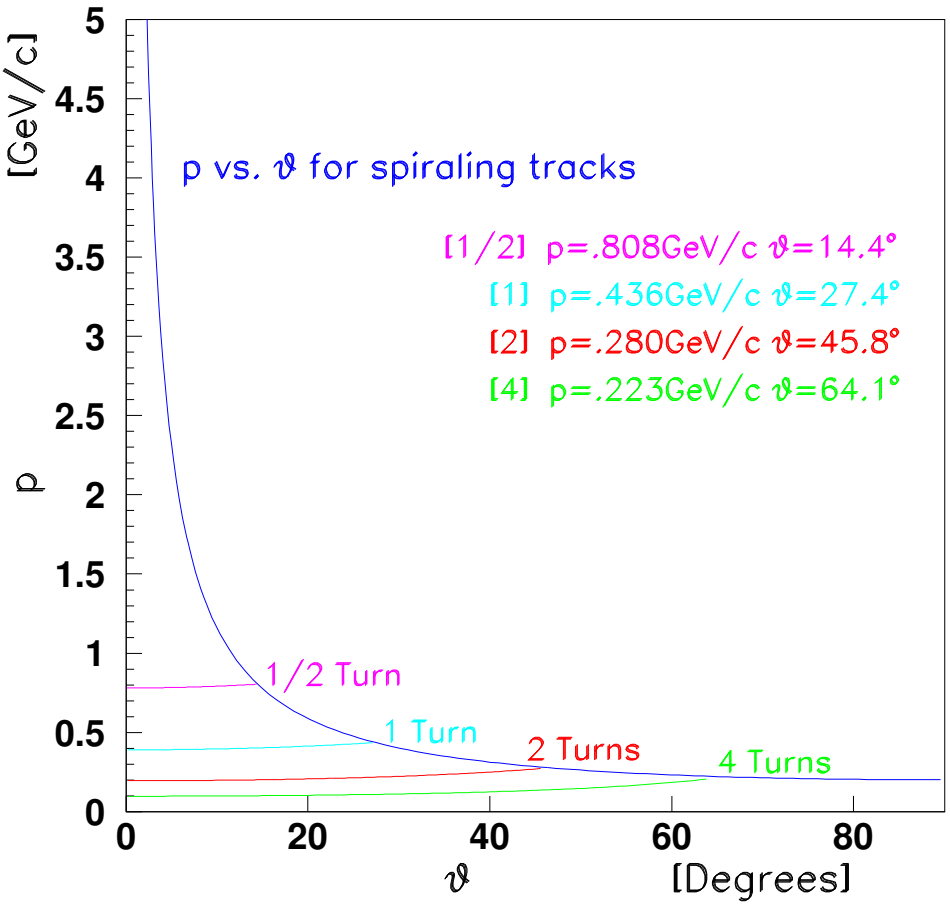

Figure 5.5: This figure shows the number of full circles made by charged particles in the magnetic field. The limit line corresponds to $p_\perp = 0.3$ GeV/c tracks. The approximately horizontal lines indicate when the particle can make the indicated number of turns without leaving the magnet.

characteristics are given in table 5.2. VTX represents a vertex chamber located very close to the target and can double as part of the trigger system. One likely design would be to have scintillating fibers. CDC is a cylindrical detector system. This chamber would have on the order of 20 radial layers making $r\phi$ measurements of the tracks. z information would be obtained from bother 6° stereo wires, and cathode strips on the inner and outer cylindrical shells. In the forward direction, the FDC are planar drift chambers, and finally the BVT are chambers close to the beam line for measuring forward going tracks.

Corresponding to the detector layouts in figure 5.3 are momentum resolution as a function of angle shown in figure 5.6. The most striking feature of these plots are the two upward spikes at forward angles. The first is due to very stiff particles at small angles and can be improved with the addition of a dipole magnet. The second is due to the interface between CDC and FDC. This feature leads us to believe that the CDC chamber should be a long as possible.

However, the current Monte Carlo assumes a CDC position resolution which is independent of the dip–angle. This is not true; the resolution will deteriorate like $\tan\lambda$. On the other hand, the FDC chamber resolution will be optimum for tracks parallel to the beam axis, and deteriorate for tracks at small values of λ.

Finally, a second check on the detector performance is shown in Fig. 5.7. Here we have examined the reaction $\gamma p \rightarrow K^+K^-\pi^+\pi^-\pi^\circ$ where the π° is assumed missing. We have then computed the square of the missing mass, and plotted this. The second plot shows this resolution as a function of beam energy resolution. The detector resolution has been reasonably well matched to a 0.1% beam energy resolution.

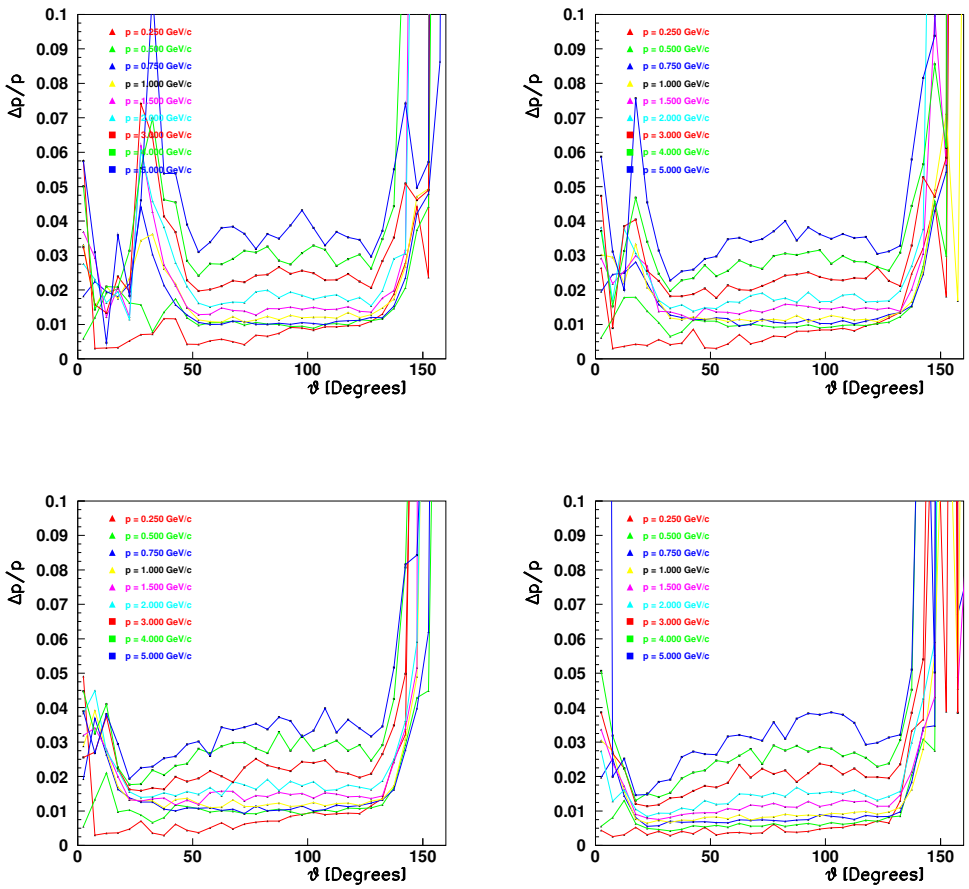

Figure 5.6: The resolution as a function of angle plotted for several total momentums. The four plots correspond to the four detector designs shown in Fig. 5.3. The large spike at about 35° in **a** that moves forward in **b** and **c** corresponds to the transition region between the central cylindrical chamber and the forward planar chambers.

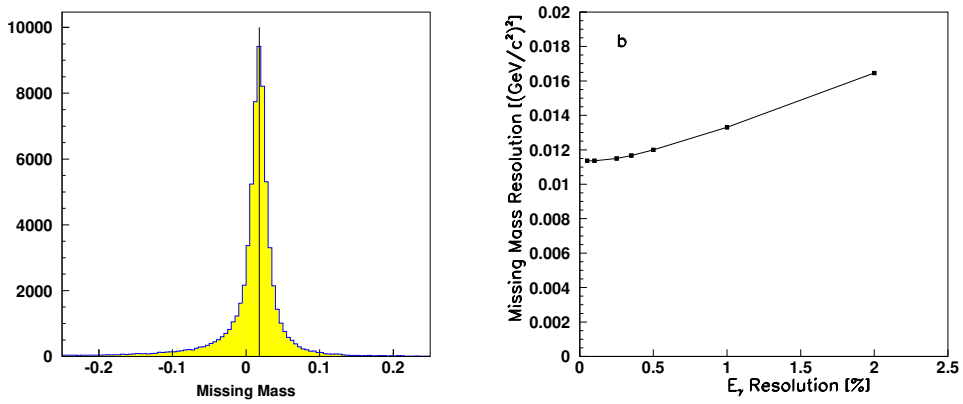

Figure 5.7: Missing mass from the reaction $\gamma p \to K^+K^-\pi^+\pi^-\pi^\circ$ where the π° is assumed missing. **a** is for 0.1% beam energy resolution, while **b** is a plot of the missing mass resolution as a function of the beam energy resolution.

5.5.1 Central drift chamber

The central drift chamber, (CDC), is used to accurately track particles between polar angles of 20° back to 170°. The chamber is filled with 5200 1 cm diameter straw tubes arranged in 22 layers. The tubes are assumed to have an $r\phi$ resolution of $200\,\mu m$, while resolution along the wire length will be obtained by placing about half of the layers at a 6° stereo angle. A typical hydrocarbon drift gas will have v_d on the order of $50 mm/\mu s$, meaning maximum drift times will be on order of $100\,ns$. In which case a $4 ns$ drift time corresponds to $200\,\mu m$ of drift. In addition, there will be cathode strips on the cylindrical wall of the chamber to provide a point with $500\mu m$ resolution. Many of the charged particles will not reach the time–of–flight system in the calorimeter, requiring that use the dE/dx information in the chamber for particle identification. This requires both TDC and ADC readout on the chamber. This is likely to be better accomplished with a flash–ADC system, though this system would probably need to run at 250 MHz, ($4.0\,ns$ time bins).

5.5.2 Central vertex chamber

The central vertex chamber has several purposes. First it will be used to provide accurate tracking information very close to the target. These track elements need to be *connected* to both the CDC as well as the FDC chambers.

Secondly, this chamber needs to provide a fast signal which can be used in the level–0 trigger of the experiment. We are currently proposing a scintillating fiber array to provide this. The exact dimensions of the fibers needs to be optimized for both position resolution and sufficient light output for trigger purposes. This optimum is somewhere between 0.5 mm and 1.0 mm fibers. We currently assume six layers of $1mm$ fibers between $5.0\,cm$ and $5.5\,cm$ radius. This leads to roughly 2000 fibers. We currently assume only TDCs on these fibers, but of course there will be other electronics associated with the trigger system.

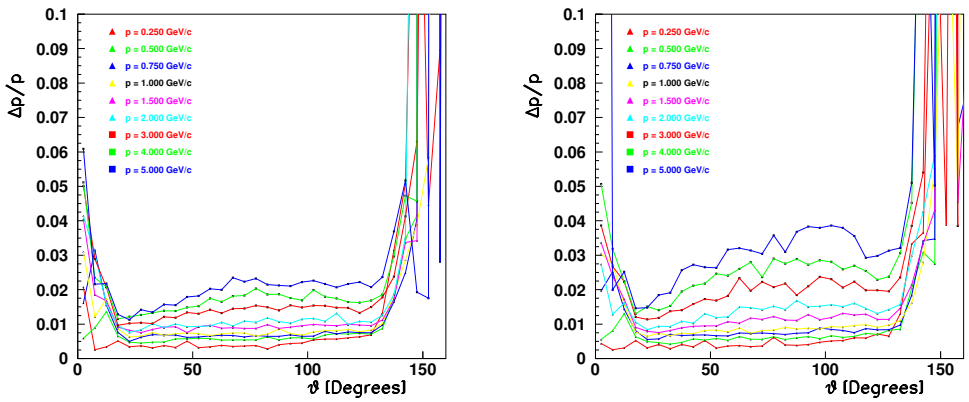

Figure 5.8: Tracking resolution as a function of angle and momentum. The left–hand figure has $200\mu m$ resolution in the CVC, while the right-hand one has $1000\mu m$ resolution.

5.5.3 Forward drift chambers

The forward drift chambers FDC are disk shaped drift chambers. The basic drift package is a plane of wires with $200\mu m$ spatial resolution between two plans of cathode strips. the strips are arranged in a u and v geometry with respect to the wires, allowing the reconstruction of a 3–D space point from each hit. The chambers are arranged in packages of six to provide a small track segment to facilitate later linking of tracks. Given the number of spiraling tracks, it is critical that these chambers not only provide good spatial resolution, but also reasonable direction information.

The basic chamber element is an annulus of inner radius 10.0 cm and outer radius 60.0 cm The wires strung as chords across the chamber. With a 1.0 cm

wire spacing, each chamber will contain 119 wires. In addition, there will be an equal number of cathode strips on each face, leading to 357 channels per chamber, or about 2200 channels per package. With four packages, this leads to 8800 channels of electronics.

5.5.4 The beam vertex trackers

The Beam Vertex Trackers, BVT, are small low–mass drift chambers located very close to the beam pipe. They are necessary to reconstruct fast small angle tracks, hopefully down to about 1° off the beam axis. The performance of these chambers is dominated by multiple scattering effects, so it is critical to make them as low mass as possible. They are also in a very high rate environment, so it is necessary that they have maximum drift times on the order of $100ns$.

These chambers are also annulus shaped, with inner radius 3.00 cm and outer radius 12.00 cm. With 5.00 mm wire spacing, each plane will have 24 wires. Each package is assumed to have three planes, and there are 6 packages in the detector. This leads to 432 channels of electronics.

5.5.5 Electronics

Table 5.4 summarizes the numbers of ADC and TDC channels needed in the basic drift chamber configuration. The only chamber that needs to have dE/dx information is the CDC, where many of the slow tracks will not reach the time–of–flight systems. Here it would be possible to replace the ADC / TDC pair with flash–ADCs, although they would need to run at $250\,MHz$ to provide sufficient spatial resolution.

Detector	*Anodes*			*Cathodes*		
	channels	*tdc*	*adc*	*channels*	*tdc*	*adc*
VTX		2000	0	0	0	0
CDC	5200	5200	5200	1000	0	1000
FDC	2856	2856	0	5712	0	5721
BVT			0	0	0	0
total		8056	5200	6712	0	6712

Table 5.4: A summary of the electronic channels in the detector components.

5.6 Particle identification

5.6.1 Introduction

This section discusses the initial design of a particle identification (PID) system for the STAGE 1 detector in HALL D . In order to design a PID system for a general purpose detector, it is best to start by choosing some typical reaction as a benchmark. One then follows up by testing the initial design against other reactions of interest.

Our initial design focuses mainly on K/π separation in the reaction $\gamma p \to K^\star \bar{K}^\star p$. The early physics goals in HALL D will likely involve reactions exciting various forms of strangeonium. These reactions will lead to multiparticle final states containing both $K^\pm$ and $\pi^\pm$. However, a large part of the cross section will lead to similar multiparticle states but with all pions, hence our present focus. We also consider identification of the recoil proton.

SLAC Experiment E135, a.k.a. LASS [100] used time-of-flight and two gas Čerenkov detectors, but also relied heavily on kinematic fitting for PID. For example, see their measurements of the reactions $K^- p \to \Lambda K^\star \bar{K}^\star \to \Lambda K^+ K^- \pi^+ \pi^-$ [106] and $K^- p \to \Lambda \pi^+ \pi^- \pi^+ \pi^-$ [107]. We expect to use the LASS solenoid as the primary magnetic field for our STAGE 1 detector, and it is therefore reasonable to use that facility as a guide for our initial design.

A sketch of the STAGE 1 apparatus, with particular attention to PID, is shown in Fig. 5.1.

Identification of downstream particles will be done primarily using high resolution Time-of-Flight (TOF) for the lower momenta, and a heavy gas Čerenkov threshold for the fastest particles. At larger angles, we will rely on dE/dx measurements in the drift chambers, and on TOF measurements with the Pb/SciFi barrel calorimeter.

5.6.2 Event simulation

We generated 10^4 events of the type $\gamma p \to K^\star \bar{K}^\star p$ using the program gener8, with 8 GeV photons. The p, $K^\pm$, and $\pi^\pm$ momentum distributions are shown in Fig. 5.6.1 for all events and for particles which emerge at angles less than 14.5° with respect to the beam direction. The cross section for four charged pion production is substantial, proceeding through high mass vector resonance production [108], so it is reasonable to expect a significant pion contamination in the four prong event sample. Clearly, the main problem in the forward region is to separate $K^\pm$ from $\pi^\pm$ over momenta from 1 to 5 GeV/c or so.

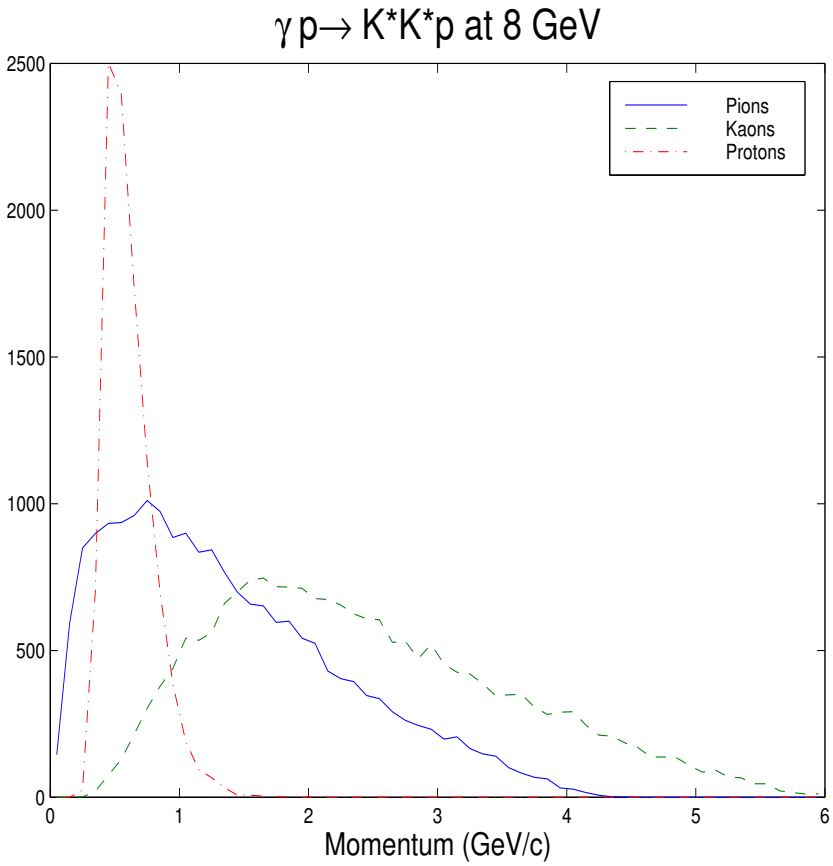

Figure 5.6.1 Momentum distributions for particles produced in the reaction $\gamma p \to K^{\star}\bar{K}^{\star}p$ at 8 GeV/c. Particles within 14.5° will emerge from the downstream end of the solenoid.

We have not tracked the particles through the magnetic field, but for this simple analysis we can neglect the bending. In PDG notation, the radius of curvature R in a magnetic field B is related to the momentum p as $p\cos\lambda = 0.3BR$ where λ is the "pitch" angle and R, B, and p are measured in meters, tesla, and GeV/c respectively. In our geometry, $p\cos\lambda = p_{\perp}$. We can estimate the effect of bending by calculating the fraction of one circular orbit executed during the time the particle spends in the solenoid. The time for one circular orbit is $2\pi R/c\cos\lambda$ and the transit time through the solenoid is $L/c\sin\lambda$ where $L \approx 3.5$ m. With $p = 4$, and $B = 2$, this fraction works out to be

$$\frac{L/v\sin\lambda}{2\pi R/v\cos\lambda} = \frac{L/\sin\lambda}{2\pi p/0.3B} \approx 0.1$$

for particles which emerge at small enough angles to exit the solenoid (i.e. λ

near 90°). This gives us some feel for the aberrations in particle trajectory exiting the magnet. We can neglect them for flight path estimates, but they will likely introduce important effects for calculating the effect on Čerenkov light direction.

The maximum radius of curvature that will be contained inside the magnet is the value of R that equals one quarter of the bore diameter of 185 cm. Therefore only particles with $p_\perp \leq 280$ MeV/c will be able to execute more than half a revolution before hitting the inside of the solenoid. Thus, if a particle is produced at an angle greater than 14.5° with respect to the beam, it will not exit the solenoid unless its momentum is less than about 1 GeV/c. Particles that do not exit the solenoid will be identified by a combination of TOF in the Pb/SciFi barrel and by dE/dx in the drift chambers.

5.6.3 PID for forward particles ($\theta \leq 14.5°$)

Time-of-flight is useful for PID in the forward region, if the particle momentum is not too high. Assuming a five meter flight path, the time difference between $\pi^\pm$ and $K^\pm$ works out to be the following:

p (GeV/c)	$t_K - t_\pi$ (ps)
2	463
3	207
4	117
5	75

For TOF scintillators that are ≈ 2 m long, RMS time resolutions on the order of 100-120 ps are typically achievable using well established techniques [109, 110]. With improvements in photomultiplier (PMT) design, however, one can achieve 50 ps RMS for detectors with long, narrow geometry. For example, Ref. [111] describes 2 m long detectors, with 2.5×2.5 cm^2 cross section and a 12-stage bialkali PMT on each end, which do this well. Of course, it would be important to control temperature and many other factors to routinely get 50 ps resolution on a large bank of counters.

TOF should therefore be sufficient for momenta up to 2 or 3 GeV/c, for most of the reactions we would consider. It is still necessary, however, to establish some method of K/π separation in the forward region for the upper end of the momentum spectrum.

Of course, this is typically the region where heavy gas atmospheric Čerenkov detectors become useful for pion detection. The LASS experiment employed such a detector, using geometry and energies rather similar to what we consider

here. This detector [100] used a gas volume that filled the downstream end of the solenoid, and used mirrors and guiding optics to focus light onto high gain, single-photon counting PMT's (RCA 8850, now available from Burle Industries). These optics and PMT's separated the detector into 12 equal "pie" slices in azimuthal angle, with each slice divided radially into three segments. There were also two mirror and PMT combinations in the beam region, giving a total of 38 optically separated detectors viewing the same gas volume but for different particle trajectories.

Figure 5.6.2 shows the efficiency calibration for the LASS Čerenkov detector, for each of the three radial "rings" of optical segments. For these measurements, the gas volume was filled with Freon-114 ($C_2Cl_2F_4$), with $n-1 = 1.53\times10^{-3}$ for π (K) momentum threshold of 2.51 GeV/c (8.95 GeV/c). (Fluoro-chlorocarbons are not longer produced, but a similar gas, C_4F_{10} is available and has $n - 1 = 1.4 \times 10^{-3}$.) [112] The efficiency is a bit low (0.97) for the outermost ring ("A"), but the detector performs very well overall. The photoelectron yield, based on a simultaneous fit to the efficiency curves of all three rings, which includes a constant background term, gives photoelectron yields of 4.6 ± 0.2/m, 4.8 ± 0.1/m, and 5.3 ± 0.2/m for rings A, B, and C respectively.

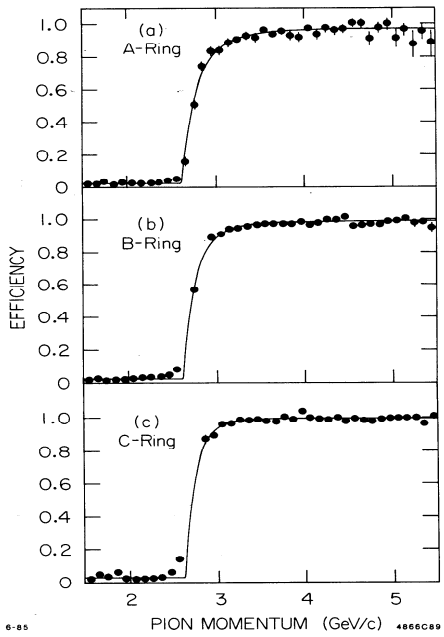

FIG. 57. The dependence of efficiency on momentum for the three rings of $\check{C}_1$; the curves correspond to the fits described in the text.

117

Figure 5.6.2 Performance of the LASS Čerenkov detector. The three "rings" correspond to the mirror and PMT configurations that encircle the beamline at three different radii. The detector is filled with Freon-114, for which the $\pi^{\pm}$ threshold is 2.5 GeV/c. The curves represent simultaneous fits through all three sets of data, for the expected Čerenkov efficiency curve plus a constant background. These fits yield asymptotic efficiencies of 0.971, 0.987, and 0.998 for rings A, B, and C respectively, and a yeild of about five photoelectrons per meter of gas.

These results suggest a C_4F_{10} filled Čerenkov detector followed immediately by a TOF system, just upstream of the LGD. It seems quite reasonable to follow a design based on the LASS system. (Unfortunately, that original detector is no longer available.)

Finally, a pipeline readout system will be used for the STAGE 1 detector. This has important implications for high resolution time-of-flight. This type

of readout digitizes analog signals in a stream, with analog values converted to digital signals at some characteristic sampling frequency. This works fine for things such as drift chamber timing, but since standard "flash encoder" ADC's are clocked at a few hundred MHz (i.e. several nanoseconds between time bins), it is difficult to achieve TOF resolutions on the order of 100 ps. However, recent development [113, 114] of high rate, pipeline TDC chips for the COMPASS experiment imply that the technology is feasible for our STAGE 1 design.

5.6.4 PID for particles within the solenoid ($\theta \geq 14.5°$)

It is clear from Fig. 5.6.1 that most particles with momenta greater than 2 GeV/c will leave through the downstream end of the solenoid. Lower momentum particles produced at small enough angles so that they also exit the solenoid should be easy to identify with TOF. Higher momentum particles, produced at large angles so that they intersect the inside of the solenoid, will be more difficult to identify. However, we fully expect to finally constrain events using kinematic fitting. Even if one or two particles have ambiguous identification, then by applying energy and momentum constraints we can still identify the event as a whole with good reliability.

We have two handles on PID within the solenoid. These are dE/dx information from the drift chamber signals, and TOF from the Pb/SciFi calorimeter modules lining the inside of the solenoid. Of course, for particles with low enough transverse momentum ($p_\perp \leq 280$ MeV/c) there will only be dE/dx information since they will not intersect the Pb/SciFi detectors, but in this case the energy loss difference between $p/K/\pi$ will be quite large.

The use of dE/dX in particle identification has in fact been recently reviewed [115, 116] One key consideration (see Table 1 in [115] is the number of samples along the track. Figure 5.6.3 shows the p/π^+ separation achieved in the LASS detector using six concentric cylindrical proportional chambers [100] each with anode and two cathode readouts, for a total of up to 18 samples. The dE/dX resolution here is not well-determined (the chambers were operated in near-saturation mode), but it is roughly 10%. Depending on the final drift chamber configuration, we should do somewhat better, particularly if care is taken to ensure optimal dE/dX characteristics from the start.

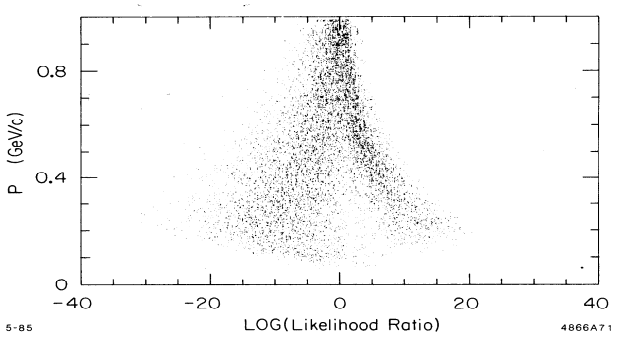

FIG. 67. A scatter plot of the logarithm of the likelihood ratio (P_p/P_π) versus particle momentum for positive cylinder tracks.

135

Figure 5.6.3 A scatterplot of the likelihood ratio P_p/P_π versus particle momentum for positively charged tracks in the LASS spectrometer. These data were taken with the cylindrical proportional wire chamber package, with up to 18 dE/dX samples per track. Clear separation is seen for momenta up to a few hundred MeV/c.

Time-of-flight using the Pb/SciFi detectors is an extremely valuable tool. The scintillation fiber component is quite fast and is in principle capable of high quality timing for single tracks. The time resolution achievable has been discussed previously.

5.7 Forward calorimetry

The Brookhaven National Laboratory E852 lead glass calorimeter will be used during the initial stage of HALL D operation.

The Lead Glass Detector (LGD) consists of an array of 3045 $4 \times 4 \times 45$ cm type F8-00 lead glass blocks stacked in a 43×71 rectangle with four corner blocks and four central blocks removed. Cerenkov light produced by interacting photons and electrons is measured by type FEU-84-3 Russian made phototubes. The tubes are powered by a computer controlled, Cockroft-Walton type base. The tube/base assemblies are held in an aluminum and soft iron structure referred to below as the cellular wall. The entire assembly is carried by a transporter to allow each module to be placed in an electron beam for calibration. A laser based illumination system is used to monitor the detector.

The glass and phototubes have been described [117] in detail but a brief description follows.

The transverse dimentions of each block were determined by an automated measuring system. The average block size was 40.0068 millimeters with a standard deviation of 24.0 microns. The high precision machining of the blocks allowed them to be stacked tightly in the array. The space between two typical blocks (as determined by a feeler guage) is less than 100 microns.

The quantum efficiency and noise rate was measured for each tube. The average quantum efficiency was 21% with a standard deviation of 3%.

The bases [118] are computer controlled Cocroft-Walton voltage multipliers. This design allows the system to operate with a small power consumption and with minimal cabling not associated with the signal. It is anticipated that bases identical to TJANF experiment E94-016 (Radphi) will be used

5.7.1 Performance

The calorimeter was used as a detector and a trigger element in BNL E852 and has been described previously.[119] Good position and energy resolution allowed for the reconstruction of multi-photon final states. Figure 5.7.1 gives some examples. We anticipate similar performance in the HALL D environment.

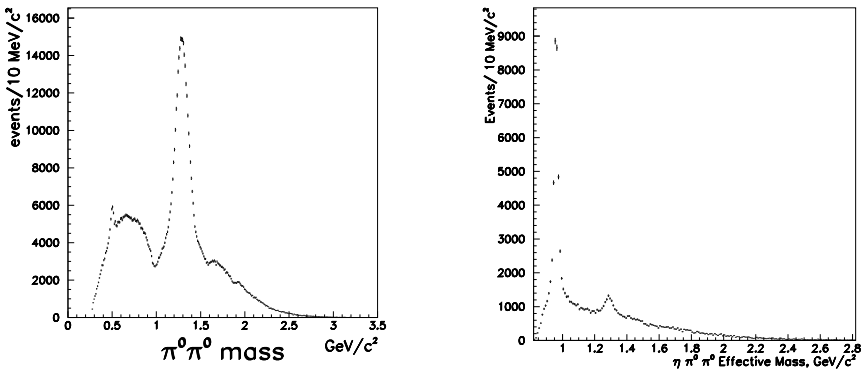

Figure 5.7.1 Left) The $\pi^0\pi^0$ effective mass as reconstructed from 4 photon events. Right) The $\eta\pi^0\pi^0$ effective mass as reconstructed from 6 photon events. Clear structures associated with the $\eta'(958)$ and $\eta(1295)$ are seen.

A trigger processor[120] allowed the calorimeter to be used as a trigger device. The total energy deposited and the effective mass of the photon system were calculated by this trigger processor. This allowed selection of well contained events or the rejection of relatively uninteresting final states. When used in conjunction with a charged track counting trigger element, final state topologies like, for example, $\pi^+\pi^-\eta$ (with $\eta \rightarrow \gamma\gamma$) could be selected while the $\pi^+\pi^-\pi^0$ topology was reduced. Figure 5.7.2 shows the result when events are selected by such a trigger.

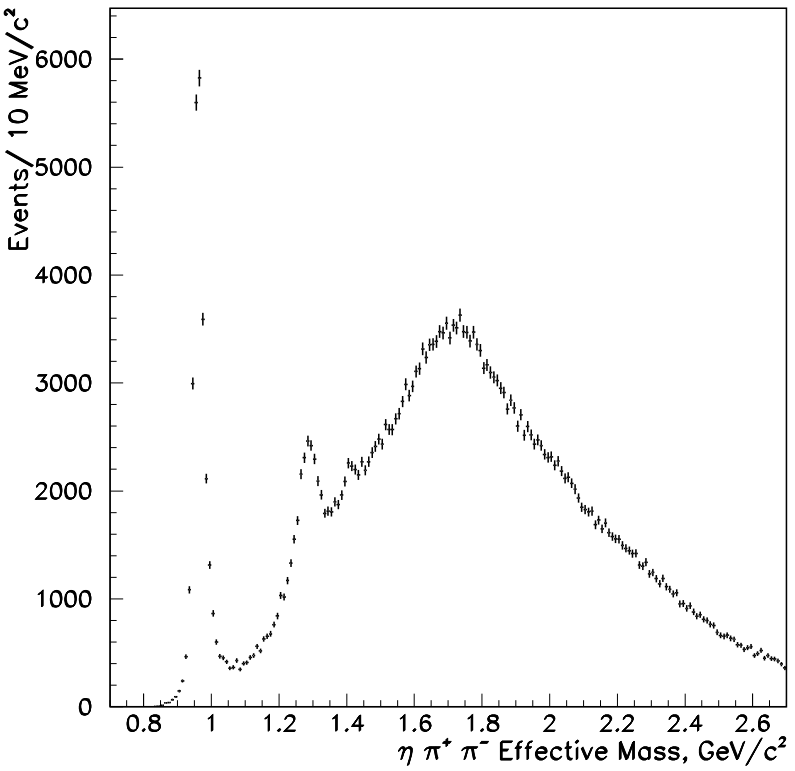

Figure 5.7.2 The $\eta\pi^+\pi^-$ effective mass distribution as reconstructed from "two charged tracks" plus $\eta \to \gamma\gamma$ events. Clear structures associated with the $\eta'(958), \eta(1295)$ and $\eta(1440)$ are seen.

5.7.2 Mechanical description

The transporter

The transporter system consists of four major components. (see figure 5.7.3) We refer to these components as the inner frame, the outer frame, the drive system and the rails.

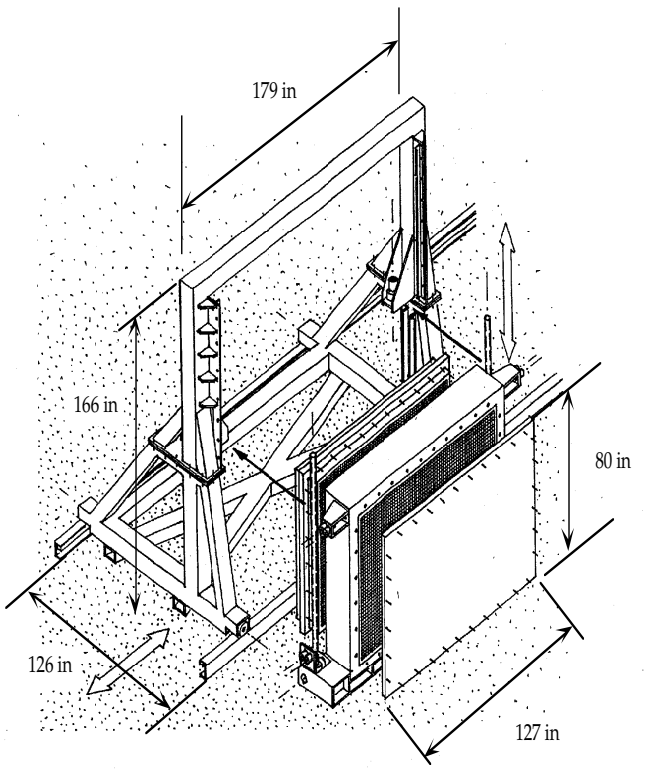

Figure 5.7.3 The E852 lead glass detector.

The inner frame, constructed of welded I-beams and steel tube carries the lead glass, the cellular wall, the phototubes and their bases and a light tight enclosure at the rear of the detector. The inner frame can move vertically via the vertical component of the drive system.

The inner frame is in turn carried by the outer frame. The outer frame has guide rails to constrain the vertical motion of the inner frame and flanges to support the ball screws of the vertical drive system. The wheels of the outer frame rest on the rails to provide horizontal motion.

The rails will be bolted and grouted to the floor of the experimental hall.

Motion of the transporter is provided by the horizontal and vertical drive systems. Vertical motion is produced by ball screws driven through worm drive speed reducers by a high torque stepping motor. Electrically operated brakes (locked when power off) hold the transporter in place (vertically) when it is not moving.

Horizontal motion is produced by a rack and pinion system driven through a worm gear speed reducer. An identical high torque stepping motor drives the vertical system. The transporter is constrained to its path on the rails by a guide roller system with wheels on the transporter and a guide block on the front rail.

A torque limiter, between the horizontal stepping motor and the speed reducer mechanically disconnects the motor in the event the transporter encounters an obstacle to horizontal motion. Limit switches and an interlock system prevent motion outside the desired range and operation of the system during periods when safety considerations forbid it.

The transporter position is determined by rotational position transducers connected to the speed reducers. Comparison of mechanical position measurements and the position measurements derived from these transducers showed that the transducers produced repeatable results in agreement with the independent mechanical measurement to within 0.5 mm.

The cellular wall

In order to hold the phototube/base assemblies at the rear of the lead glass blocks an aluminum and soft iron assembly was constructed. This "cellular wall" must serve two purposes: mechanical support and alignment of the phototubes and their bases and magnetic shielding of the tubes.

The design selected to achieve these goals consisted of a sandwich of aluminum plates supporting steel tubes between them. Two aluminum plates, 1/2 inch thick, had 3053 (43 by 71) 39 mm holes bored in them. The holes were on 40 mm centers. Each hole in one of the plates recieved a press fitted machined soft iron tube. When all the tubes were installed, the second plate was placed atop the array of tubes. The tubes were machined to have a slip fit into the upper plate. The outer edges of the plates were secured to aluminum blocks to provide a structure with sufficient rigidity for it to be moved. Further rigidity was obtained by filling the inter-tube gaps with epoxy. The epoxy was poured in several stages and allowed to cure between stages. 59 gallons were required. Additional magnetic shielding was provided by three layers of mu-metal installed in the front half of the soft iron tube.

Modifications required for HALL D

Two major modifications for use in HALL D are anticipated:

- The horizontal motion will be perpendicular to the E852 configuration, that is, horizontal motion will be along the beam axis

- A platform behind the LGD darkroom will be added. This platform will carry the delay cables and the electronics associated with the LGD.

Figure 5.7.4 shows the E852 LGD as modified for HALL D .

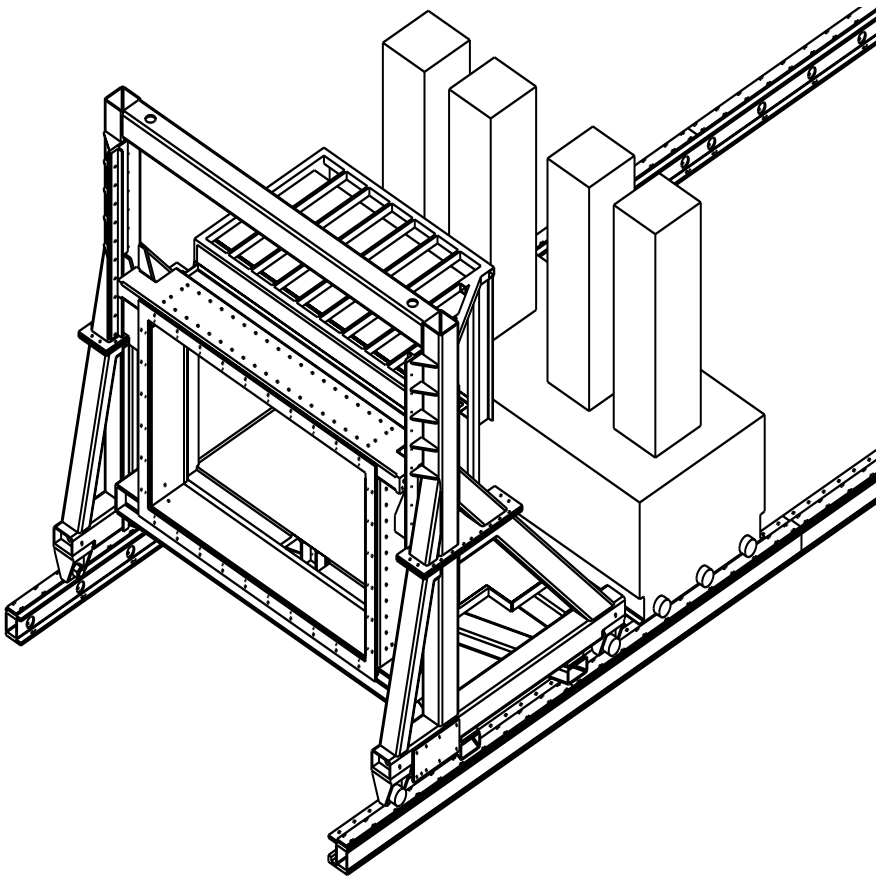

Figure 5.7.4 The E852 lead glass detector as modified for HALL D

These modifications are to allow for disassembly and staging of the detector. A large range of z-motion is required to allow removal and servicing of the solenoid region components. The addition of the platform makes the detector self-contained, all cables and electronics are contained on this platform and move with it. This modification satifies the desgin requirements while removing the need for a complex cable carrier.

5.7.3 Radphi experience

Operating an electomagnetic calorimeter, like the LGD, near a photon beamline could be a concern given the backgrounds one might expect with a tagged bremsstrahlung photon beam. For this reason, the recent experience with the LGD used in the Radphi experiment during a recent test run in the Hall B photon beam is of particular relevance. Because of the high quality of the photon beam, beam- associated backgrounds were manageable, even when operating at an endpoint energy of 4 GeV. At higher energies the beam spot size will be even smaller and the LGD energy resolution will improve.

This goal of the Radphi experiment is the measurement of rare radiative decays of the ϕ meson. The Radphi experiment uses an LGD similar to that used in the E852 experiment with 700 similar lead glass blocks arranged in a roughly circular arrangement around the beam. A two block by two block hole allows for passage of the beam. The PMT bases are of the Cockcroft-Walton type and the same ADCs and trigger processor used in the E852 experiment were used in this test run as well. The Radphi experiment is located in Hall B downstream of the CLAS detector. The tagged photon beam operated at an endpoint energy of 4 GeV and the photon beam passed through the CLAS target before reaching the Radphi experiment. For this run a cylindrical beryllium target was used (1 *in* long and 1 *in* diameter) placed about 1 *m* from the front face of the LGD wall.

The data shown here are from 10M triggers of the 15M collected in the test run. The triggers were passed through a cluster finder which looks for showers in the LGD array due to photons. Events with two clusters show clear presence of the π^0. The π^0 signal was used to calibrate the LGD by adjusting the gains of each of the modules to yield the nominal mass and to minimize the width of the π^0 seen in the 2γ mass distribution.

A skim on the 10M-trigger data set was performed to separate out events with three or more clusters. About 680,000 events remain with 75% of these events containing three clusters.

The 2γ effective mass spectrum from two cluster events in shown in Figure 5.7.5. Clear peaks at the π^0 and η are observed. The calibration procedure that the centroid of the peak occurs at the nominal mass. The observed width of the peak is 14 MeV/c^2. A fit of the η peak, show in Figure 2, yields a mass of 547 $\pm$ 4 MeV/c^2 and a width of 64 MeV/c^2 .

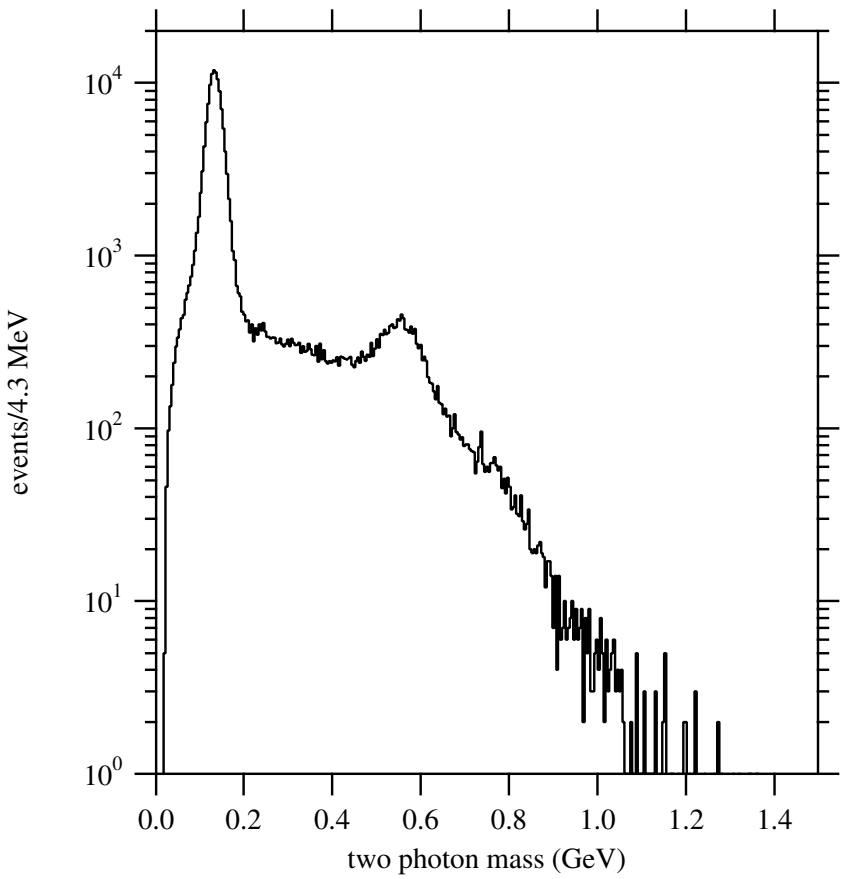

Figure 5.7.5 Two photon effective mass from two-cluster events from the Radphi experiment.

Figure 5.9 shows the effective mass distribution for 3γ events (plots (a) and (b)), 4γ events (plot (c)) and 6γ events (plot (d)). In each case the total energy in the LGD was required to exceed 3 GeV, increasing the probability of observing contained events.

Plot (a) shows the 3γ effective mass distribution for events in which two of the photons are consistent with $\pi^0 \to 2\gamma$. Note the peak in the vicinity of 780 MeV/c^2 indicating events from the decay: $\omega \to \pi^0 \to 3\gamma$. A fit of this region of the mass distribution to a Gaussian results in a mass of 780 MeV/c^2 with a σ of 63 MeV/c^2.

Plot (b) shows the 3γ effective mass distribution for events in which two of the photons are consistent with $\eta \to 2\gamma$. In addition, no diphoton is consistent with $\pi^0 \to 2\gamma$. Note the peak in the vicinity of 1 GeV/c^2 indicating events from the decay: $\phi \to \eta \to 3\gamma$.

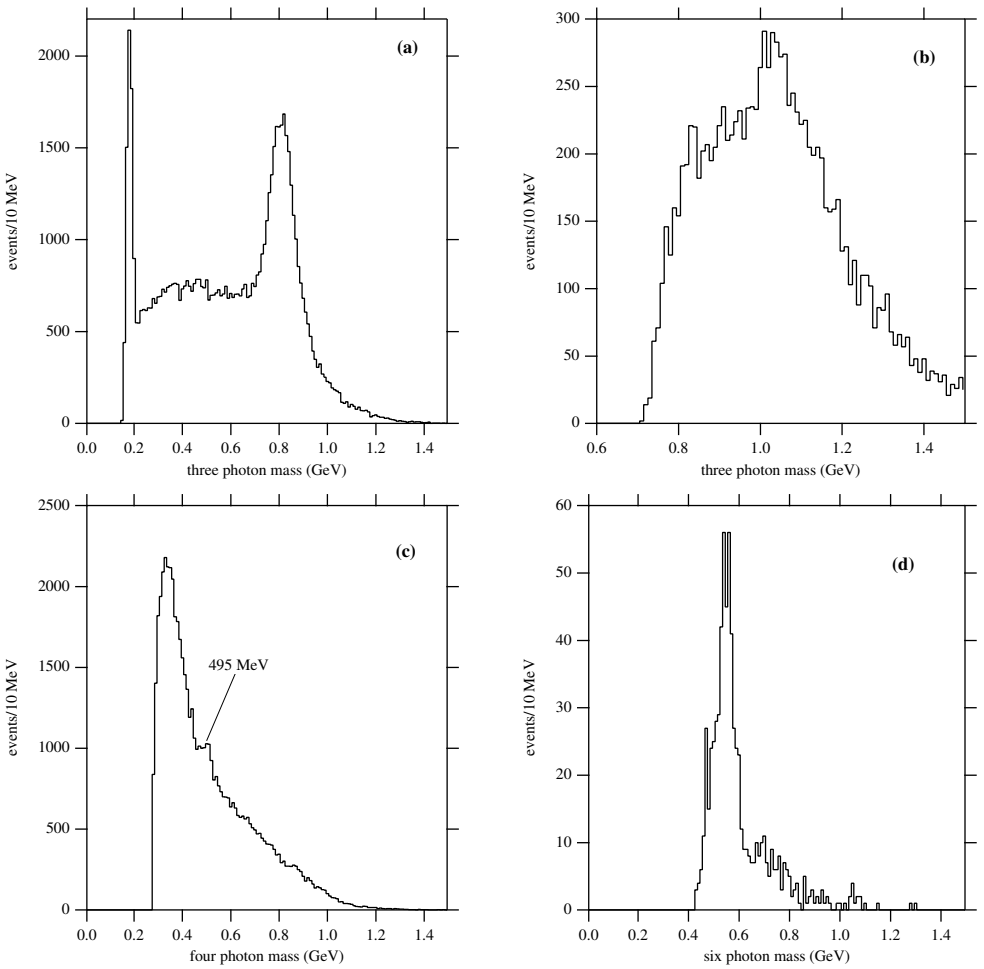

Figure 5.9: Effective mass distribution for multi-photon cluster events in the Radphi experiment test run. Plot **a** is for $\pi^0\gamma$ events. Plot **b** is for $\eta\gamma$ events. Plot **c** is for $2\pi^0$ events. Plot **d** is for $3\pi^0$ events.

Plot (c) shows the 4γ effective mass distribution for events in which two diphoton combinations are each consistent with $\pi^0 \to 2\gamma$. These events are then fitted to the $\pi^0\pi^0$ hypothesis. Note the presence of the peak at around 500 MeV/c^2 indicating the decay $K_S^0 \to 2\pi^0$. A fit to this peak shows that 470 ± 80 events are in this peak and the central value of the mass is 499 ± 3 MeV/c^2. Note that the analysis procedure assumes that all photons originate from the target so no allowance is made here for the decay vertex of the K_S^0 occurring outside the target.

Plot (d) shows the 6γ effective mass distribution for events in which three diphoton combinations are each consistent with $\pi^0 \to 2\gamma$. These events are then fitted to the $3\pi^0$ hypothesis. Note the presence of the peak at around 550 MeV/c^2 indicating the decay $\eta \to 3\pi^0$. A fit to a Gaussian yields a mass of 543 ± 3 MeV/c^2 and a σ of 26 MeV/c^2.

The Radphi experiment is approved to run with a 6 GeV photon beam. The performance of the LGD with 4 GeV photons is very encouraging since the resolution of the LGD improves with energy. For example the average energy of photons for events in the η peak of plot (d) is about 500 MeV. The average energy of photons in HALL D will be 2 GeV.

Chapter 6

Civil Construction

The plan is to site the meson spectrometer in a new experiment hall (HALL D) to be located at the end of the HALL D beamline which would come off the stub at the east end of the North Linac. The civil construction includes work associated with breaking through the stub, delivering beam above ground to a tagger, a tagger building, HALL D ,the counting house, roads and a parking area. Members of the HALL D collaboration have been meeting with members the JLab civil construction team to arrive at a cost estimate for civil construction sometime in February, 1999. The items under discussion are enumerated below.

Figure 6.1 shows the plan and elevation views for the HALL D beamline and associated buildings. Figure 6.2 shows more detail of the - tagger building and HALL D complex. Figure 6.3 shows the tagger building alone and Figure 6.4 shows HALL D alone.

6.1 Site Work

- clearing and grubbing
- relocate fence
- retaining walls at the ends of an 8-in beam pipe (tagger to HALL D)
- rework site drainage system
- select fill for project area
- relocate radiation monitoring wells
- berms, backfill, and seeding

- de-watering

6.2 HALL D

- 75 ft wide, 150 ft long, 40 ft high
- number of persons in the building 30 Max.
- top of floor at ground level
- unfinished ceiling with open web steel girders
- no windows
- no radiation protection in walls or ceiling (as confirmed by user)
- gravel approach road and parking
- thick concrete floor for 250 ton equipment and for concrete block shielding
- metal siding and metal roof
- one large overhead door, small overhead door and a double door.
- insulation with no inside finishes
- lighting, power outlets
- lightning protection system
- sprinklers
- fire alarm
- Gas exhaust and exhaust fans requirement - Forced exhaust to be provided for the following: (1) gas for chambers 10 m^3 of isobutane, (2) target 4 liter of LH_2, (3) solenoid 5000 liter of liquid helium (including reservoir), (4) solenoid 30 liter/hr of liquid He and same for liquid N_2
- HVAC with humidity control
- One 20 ton overhead travelling crane for full area

6.3 Tagger Building

- 30 ft wide, 45 ft long, 30 ft high; (Hall B tagger enclosure is 16 ft x 23 ft long x 21 ft high; keep the west wall open to install the radiation protection blocks. This will be closed using pre-cast concrete blocks. No overhead crane.
- large overhead door in one of the side walls
- number of persons in the building 10 Max.
- unfinished ceiling with open web steel girders
- no windows
- no radiation protection in walls or ceiling (as confirmed by user)
- top of floor at ground level
- gravel approach road and parking
- thick concrete floor equipment and for concrete block shielding
- metal siding and metal roof
- one large overhead doors
- insulation with no inside finishes.
- no toilets
- lighting, power outlets
- lightning protection system
- exhaust and exhaust fans not required
- sprinklers
- fire alarm
- HVAC with humidity control

6.4 Control Room

- 30 ft wide, 40 ft long, 12 ft high, with 8 ft clear ceiling height
- number of persons in the building?
- top of floor at ground level - no access flooring
- gravel approach road and gravel parking
- metal siding and metal roof
- windows
- two double doors
- insulation with painted gyp. board finish and acoustical ceiling tiles
- toilets to be provided
- lighting, power outlets
- lightning protection system
- sprinklers
- fire alarm
- HVAC with humidity control

6.5 Service building

- 15 ft wide, 20 ft long, 10 ft high
- top of floor at ground level
- gravel approach road
- metal siding and metal roof
- insulation
- no toilet facility to be provided
- lighting, power outlets

- lightning protection system
- sprinklers
- fire alarm
- HVAC with humidity control

6.6 Beam Dump

- Similar to Hall B beam dump

6.7 Concrete tunnel

- concrete tunnel 8 ft x 8 ft (high) with minimum concrete thickness of 2 ft. Small labyrinth required for personnel access only.
- maximum permissible slope about 10 .
- waterproofed
- painted inside
- covered with 5 ft of dirt for radiation protection?
- do we need an alcove no. Radiation protection to be provided by temporary shielding blocks.
- lighting, power outlets
- exhaust and exhaust fans required like in the existing tunnel.
- sprinklers
- sump and permanent de-watering
- fire alarm
- HVAC with humidity control
- fire door and radiation barrier requirements are to be defined

6.8 Permissible Settlements

- 1 in initial settlement and 2 in max over the lifetime.

6.9 Beam Pipe

- to be decided

6.10 LCW System and Cooling water Tower

- estimates for total project yet to be specified

6.11 Power Requirement

- photon building 1MW
- tagger building – 0.5 MW
- magnets in tunnel – 0.5 MW
- for economical design of the power system, it is necessary to list all loads, their voltages, locations and demand factors
- under the civil subcontract the power for all experimental equipment will be provided only to the switchboards

6.12 Communication Conduits

- Under the Civil subcontract only empty conduits are installed.
- The needs for Physics, Accelerator, and Computer and Telephone groups are to be established. Number and sizes of conduits, and the locations they need to connect, are to be established by those groups. There is a need to communicate from HALL D counting room to Photon building, Tagger Building, CEBAF CENTER and MCC.
- It will be better to include conduit requirements for Personnel Safety Interlocking, Cryo controls, Personnel Safety Signals and Controls, and Fire Safety Signals.

6.13 Items not Included Here

- Cryo Lines
- Construction and installation of shielding blocks
- Personnel safety and interlocks
- Experimental or other equipment and their installation
- Stabilized or special power supply equipment
- Communication wiring computer, telephones, and experimental signal
- Fiber optic cable system
- Furniture
- Shop Space
- Backup Electric Generator for safety systems, magnets, and Cryo Controls

6.14 Environmental and Radiation Concerns

- Project will need to be examined from environmental point of view and necessary permissions obtained for disturbing the land, before construction can start.
- Our Radiation Control Group must review the project plan, especially since the Photon Hall is so close to the edge of our property.
- There are a few Radiation Monitoring Wells in the proposed construction area. These will need to be relocated, which requires approval of Radiation Control Group.

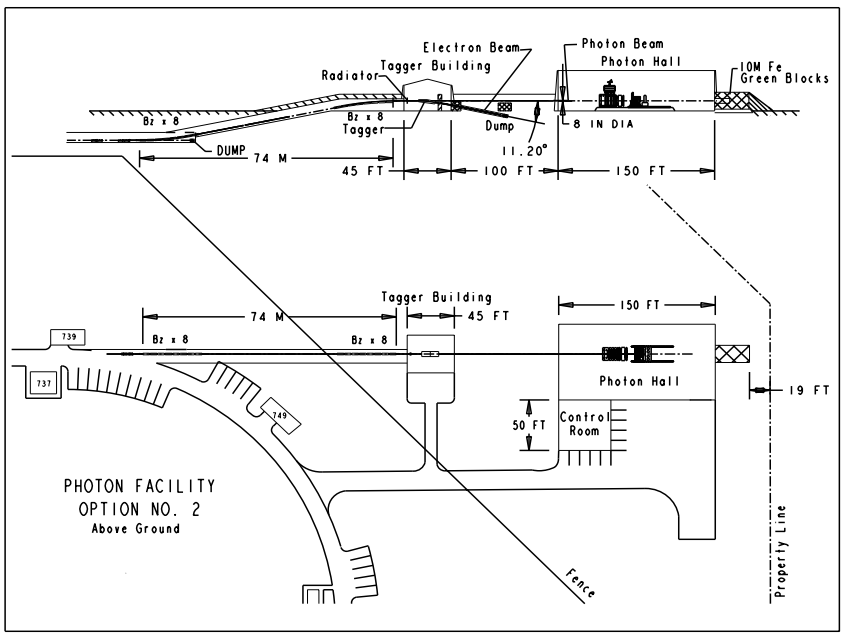

Figure 6.1: An overall view of the site modifications.

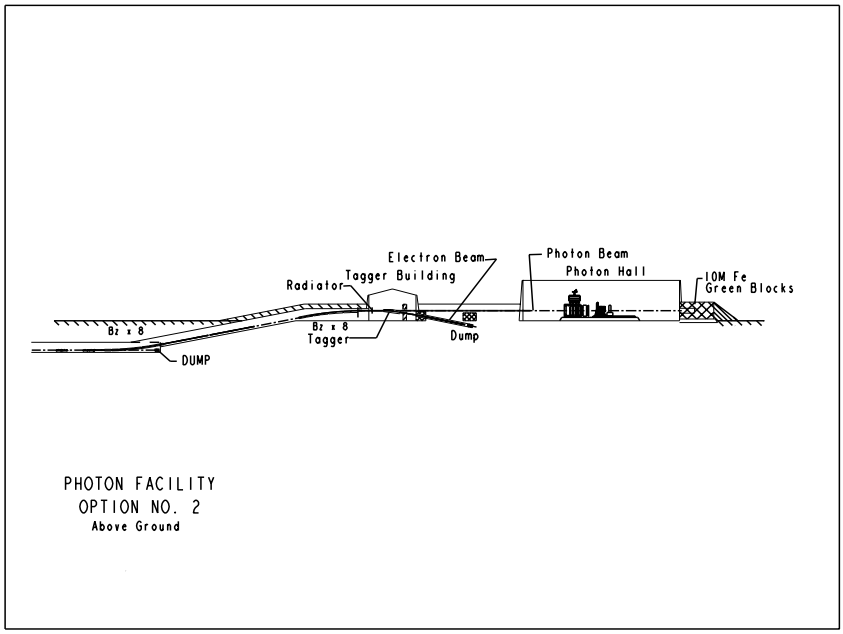

Figure 6.2: A elevation view of the modifications.

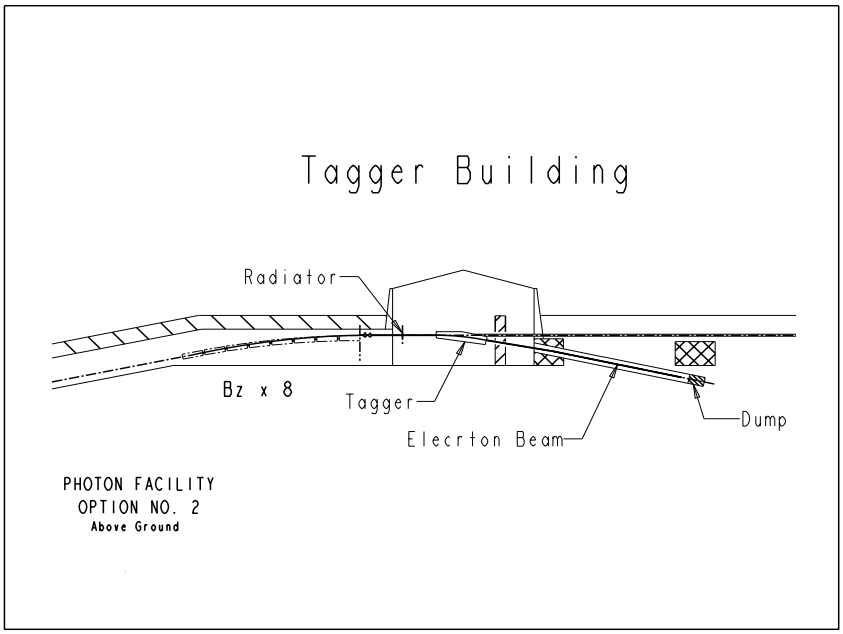

Figure 6.3: A detailed elevation view of the tagger buliding

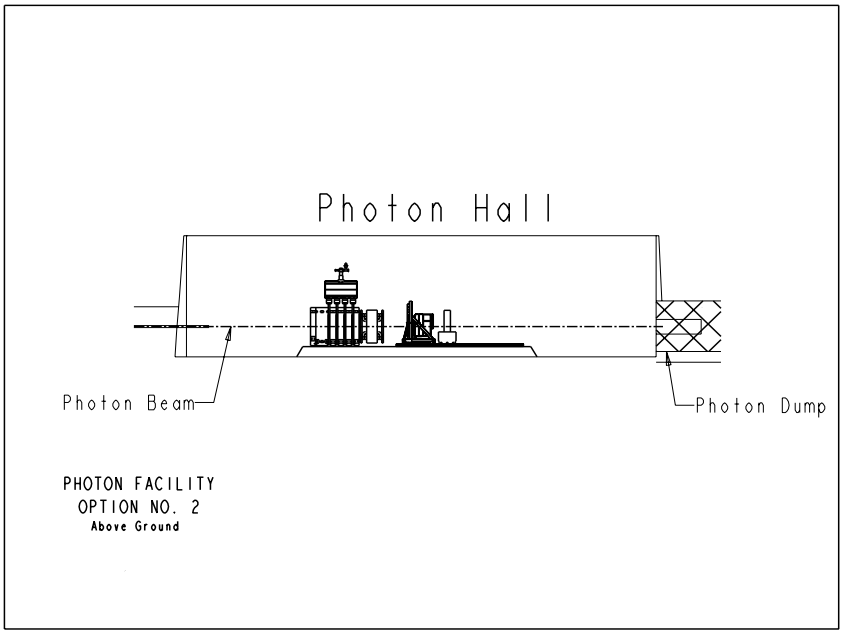

Figure 6.4: A detailed elevation view of HALL D .

Chapter 7

Rates, Trigger and Data Acquisition

7.1 Expected Rates

7.1.1 Overview

We estimate trigger and background rates in HALL D using measurements of the hadronic cross section combined with the CLAS experience. The hadronic rate between any two photon energies E_1 and E_2 can be written as

$$R = \int_{E_1}^{E_2} n\sigma(E)\frac{dN}{dE}dE$$

where n is the number of target protons per unit area, $\sigma(E)$ is the hadronic cross section as a function of energy, and dN/dE is the photon energy spectrum. We normalize the spectrum to the number of photons tagged between two energies E_{LO} and E_{HI}, and we take the spectrum shape to be simply proportional to $1/E$. Therefore, the tagged photon rate Φ is given by

$$\Phi = \int_{E_{LO}}^{E_{HI}} \frac{dN}{dE}dE$$

in which case $dN/dE = \Phi/\left[E\log(E_{HI}/E_{LO})\right]$.

The total hadronic γp cross section[1]at is plotted in Fig. 7.1. We assume an 8 GeV electron beam, and integrate from π^+ threshold (150 MeV) to the endpoint. We take a tagging range between 50% and 95% of the endpoint,

[1]We use cross measured sections [121, 122] with actual data obtained from the Durham Data Base [123]

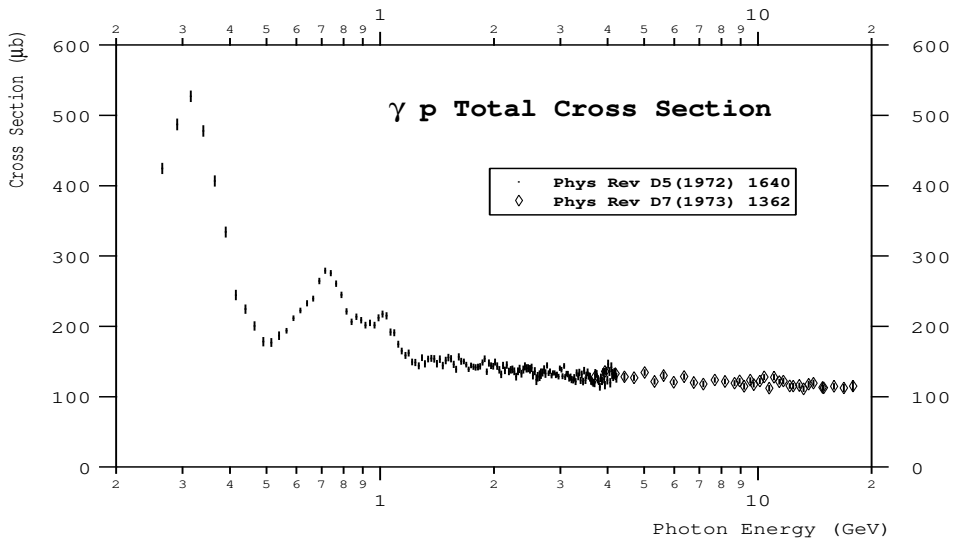

Figure 7.1: Total cross section for $\gamma p \rightarrow$ *hadrons* as a function of photon energy.

so $E_{LO} = 4$ GeV and $E_{HI} = 7.6$ GeV. The target is assumed to be 30 cm of hydrogen ($n = 1.27 \times 10^{24}/\mathrm{cm}^2$). This gives a total hadronic rate

$$R_0 = 1.56 \times 10^{-3}\Phi \tag{7.1}$$

and a tagged hadronic rate

$$R_T = 1.60 \times 10^{-4}\Phi \tag{7.2}$$

These relations are essentially unchanged for a 12 GeV electron beam, because the cross section is relatively flat at high energy.

7.1.2 Trigger Elements

We make some rudimentary assumptions about the trigger elements in order to estimate various rates. These assumptions are discussed further in the Trigger section of this document.

The trigger consists of coincidences between several counter elements of the detector, and it must select the tagged hadronic rate in the presence of accidentally coincident backgrounds. The first trigger element is the **photon tagger**, essentially a segmented scintillation counter. The total rate Φ in this counter is determined by the electron beam current and the thickness of

the radiator, both controllable (within limits) by the experiment. For design purposes, we consider tagged rates of 10^7 and 10^8 per second.

The second trigger element is the **start counter**. A start counter similar in design to that used in CLAS would suffice for tagged fluxes $\Phi = 10^7$/sec, although modifications will likely be needed to handle fluxes of 10^8/sec. One possible design might use several layers of scintillating fibers. Such a counter would also provide position information with sufficient resolution for offline track reconstruction. In comparing the demands of the HALL D start counter to the CLAS experience, it is useful to note that the HALL D target is inside a solenoidal magnetic field which will protect the start counter from the flux of low-energy Compton scattered electrons emerging from the target. The CLAS start counter does not enjoy this protection.

The tagger and start counters are small, and are therefore the best candidates for determining the precise event timing. For this discussion, we will assume that coincidences between them can be identified within a time window $\Delta T_1 = 15$ ns.

Interesting events will have particles in the final state other than the one that satisfied the start counter requirement. These particles may by energetic, forward going charged particles, forward or large angle photons and/or charged particles with sufficient transverse momentum to reach the bore of the solenoid. Any particles of this type will be registered in other elements of the detector and these signals can be used as further requirements in the trigger, and this refines the loose interaction definition given above. We refer to this collection of signals as the **global level one** trigger. As its elements are counters of extended size, we take a coincidence time window $\Delta T_2 = 100$ ns when the global level one trigger is required.

7.1.3 Accidental Rates

The "true" rate of interesting events is given by Eq. 7.2 and is 1600/sec at 10^7 photons/sec, and 16 kHz at 10^8. However, various other processes will form accidental coincidences at the different trigger stages, and we need to recognize these. It is most important that these do not form the bottleneck for the data acquisition system, regardless of our ability to reject them offline. Furthermore, these accidental rates are *quadratic* in the photon flux, so the accidental-to-true ratio grows as we increase the beam intensity.

We consider two sources of accidental background. Although they are not entirely mutually exclusive, we add them together to get a conservative estimate of the problem. The first (A_1) of these comes from purely random time coincidences between the trigger elements, in which case we compute

the time overlap based on the various counter singles rates. The second (A_2) is more "physical", considering hadronic photoproduction that is outside the tagging range, but in accidental coincidence with the tagging system.

First consider purely random coincidence events. A coincidence between the tagger and start counter loosely defines an interaction in the target. The rate A_0 of this coincidence is given by

$$A_0 = S\Phi\Delta T_1 \tag{7.3}$$

where S is the total rate in the start counter. Based on the experience in CLAS, we take $S = 0.46\Phi$, although this is most certainly an upper limit because of the solenoidal shielding effect. (In CLAS, $\approx 7\%$ of this rate is generated by tagged photons.) For $\Phi = 10^7$/sec we find $A_0 = 6.9 \times 10^5$/sec, considerably larger than the tagged hadronic rate $R_T = 1600$/sec. Further refinements are achieved by the global level one trigger.

The rate of the global Level one trigger is taken to be the total hadronic rate R_0 plus a rate C associated with cosmic rays, so the accidental rate using both the interaction and global level one triggers is

$$\begin{aligned} A_1 &= A_0(C + R_0)\Delta T_2 & (7.4)\\ &= S\Phi(C + 1.56 \times 10^{-3}\Phi)\Delta T_1\Delta T_2 & (7.5) \end{aligned}$$

where we have substituted from Eqs. 7.1 and 7.3. Note that *this expression is quadratic in the beam rate* (not including the overall factor of Φ in S which also scales the "true" events).

Let us examine these expressions numerically. The cosmic ray rate can be estimated from the surface area of the detectors and the flux at ground level which is, to a good approximation[124] given by $1/\text{min}\cdot\text{cm}^2$. For a detector cross section about 4m$\times$1m, we have $C = 4 \times 10^4/\text{min} \approx 1$ kHz, independent of the beam rate. Evaluating expression 7.5 yields $A_1 = 1145$/sec for $\Phi = 10^7$/sec, for which the tagged hadronic rate is $R_T = 1600$/sec. However, for $\Phi = 10^8$/sec, $A_1 = 1.1$ MHz and $R_T = 16$ kHz, and the situation is much more severe. The rate is plotted as a function of tagging rate in Fig. 7.2.

The second accidental background comes from true hadronic events, and therefore would pass the global level one trigger. They are out of time with the precise RF signal, but that is much smaller than the online resolving time ΔT_1 of the interaction coincidence Ignoring the "true" events that are part of this rate, one calculates

$$A_2 = R_0\Phi\Delta T_1 = (1.56 \times 10^{-3})\Phi^2\Delta T_1$$

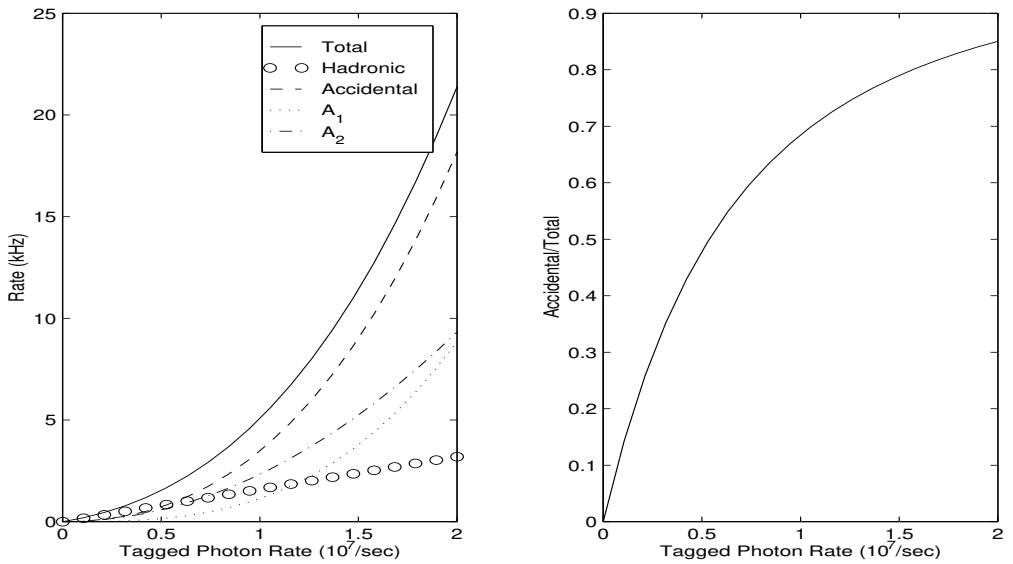

Figure 7.2: Rates for true hadronic triggers and accidental coincidences.

Once again, this is quadratic in the beam rate. We find $A_2 = 2.3$ kHz (230 kHz) for 10^7 (10^8) photons/sec. This is also plotted in Fig. 7.2, along with the ratio of accidental to true coincidences, as a function of tagging rate.

In summary, for a tagging rate of 10^7/sec, we expect a true, tagged hadronic rate of about 1600/sec, compared with an accidental rate $A = A_1 + A_2 = 3.5$ kHz. Although the signal to noise (~ 0.5) is less than ideal, this total rate should be quite manageable in the Stage I data acquisition system. However, the situation changes dramatically as we approach 10^8/sec, and a more sophisticated DAQ system will be required.

7.2 HALL D Trigger

7.2.1 Overview

Figure 7.3 shows a schematic of the implementation of the HALL D trigger. An essential feature of the HALL D trigger design is to build pipelining into the the front-end of the trigger at the outset. This has the virtue of allowing us to upgrade from initial photon fluxes of 10^7 photons/sec to eventual fluxes of 10^8 photons/sec.

A pipeline is basically a delay for which the timing resolution at the output is the same as the timing resolution at the input. An example is a clocked

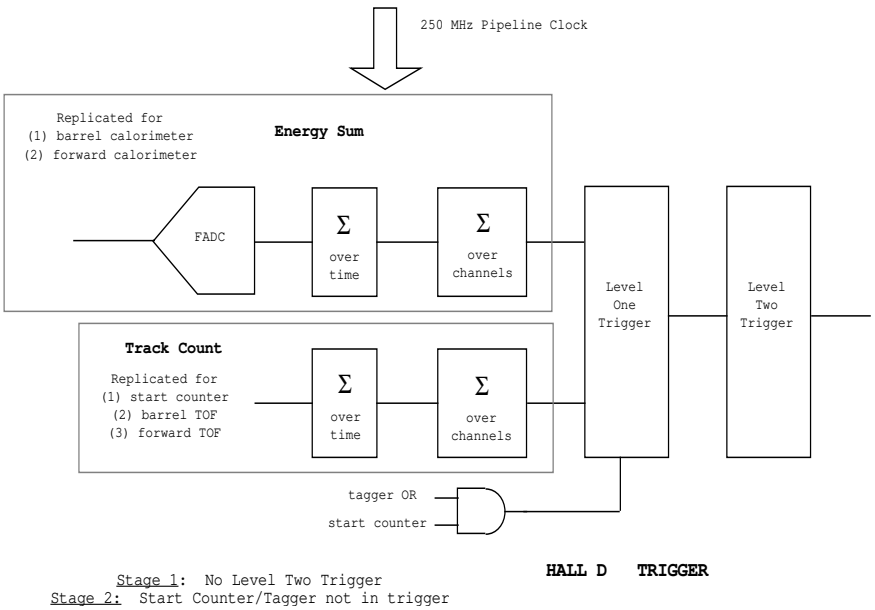

Figure 7.3: A schematic diagram of the HALL D trigger.

shift register. For each clock cycle, the data advance one step; the timing resolution is the same as the clock period, while the overall delay is the clock period times the number of stages.

Detectors which measure charge (calorimeters, dE/dX) are digitized by 8 bit, 250 MHz flash ADCs (FADC). The data pass through a shift register thus making available a time window. Successive samples within this time window are added together. This is analogous to the gate width in a conventional charge sensitive ADC. Multiple channels are added together to form an energy sum. These adders are pipelined at the same 250 MHz rate, giving an energy measurement every 4 nS for use in the *Level 1 Trigger*.

The *Level 1 Trigger* makes a decision based on detector elements which measure hadronic multiplicities (track counts) and energies. In the schematic shown, the start counter and barrel and forward TOF detectors provide the track count while the barrel and forward calorimeters determine the energy. A tight tagger OR/start counter coincidence also is used as input to the *Level 1 Trigger* for Stage 1 (photon fluxes of 10^7 photons/sec).

For Stage 2 (photon fluxes of 10^8 photons/sec), the tagger OR/start counter coincidence is not a useful requirement. It will then be necessary to impose a *Level 2 Trigger* which uses input from detectors in a more sophisticated fashion.

7.2.2 Level 1 Trigger

The *Level 1* trigger has the following 5 components:

1. **A track count** - obtained from the start counter. The start counter discriminator signals are used to create the prompt OR for coincidence with the tagger, but are also sent into a *track count pipeline* to determine the number of tracks. The sample rate for the pipeline would be 20 ns (50 MHz).

2. **A track count** - obtained from the barrel TOF. The discriminator signals from the central TOF are sent into another *track count pipeline* which determines the number of tracks. This pipeline runs synchronously with the start counter track count pipeline.

3. **An energy sum** - obtained from the barrel calorimeter. Continuous (in the same manner as in the CLAS detector) energy sums are computed for sections within the calorimeter. These sections will be complete azimuthal slices so that each sum will correspond to a fixed range in scattering angle. These sums are then sampled at the same 250 MHz rate by a flash ADC, and selectively added together to form a global digital energy sum. The inclusion of the interesting regions of the calorimeter in the energy sum will be programmable. These energy sums may also be used in the Level 2 trigger.

4. **A track count** - obtained from the forward TOF. Discriminator signals from the forward TOF are sent into a *track count pipeline* which determines the number of tracks. This pipeline runs synchronously with all the other Level 1 pipelines.

5. **An energy sum** - obtained from the forward calorimeter. The sum is programmable in the same manner as for the central calorimeter. The precise definition of the regions to be included in the sum can be defined at a later stage. These also will be used in the Level 2 trigger.

The *Level 1 Trigger* runs at the same 250 MHz rate, and has inputs from the 5 subsystems named above. Programming a single trigger means selection of

1. Either a minimum, maximum, or exact number of tracks in the start counter

2. A minimum, maximum, or exact number of tracks in the central TOF.

3. A minimum, maximum, or exact number of tracks in the forward TOF.

4. A minimum or maximum for the global energy in the barrel calorimeter. The global energy is obtained by programmed selection to include (or eliminate) interesting regions of the calorimeter.

5. A minimum or maximum for the global energy in the forward calorimeter. As above, certain areas might be programmed out of the sum.

Finally the boolean function of these five elements is programmed. The trigger would have the capability to have several simultaneously defined triggers. This trigger is very flexible and can be programmed to be very loose (say one track in the start counter) or very tight (specific track counts and energy thresholds in each detector). Examples of triggers which can be programmed in this scheme include:

1. at least two tracks in the start counter AND at least one track in the downstream TOF.

2. at least one track in the start counter AND a minimum energy in the downstream calorimeter.

3. at least two tracks in the start counter AND at least one track in the central TOF AND a minimum requirement of energy in the central calorimeter AND a minimum requirement in the downstream calorimeter.

All pipelines will run synchronously and will be timed so that the inputs from average momentum tracks ($\sim$ Ebeam/3) will hit the Level 1 global processor at the same time. Higher and lower momentum tracks will be slightly out of time, but this effect should be less than 20 ns. The synchronous output of the *Level 1 Trigger* will then be ANDed with the coincidence of the tagger OR and the start counter OR. This allows the timing to be determined by the tagger and start counter, and removes the synchronous nature of the trigger.

7.3 Data Acquisition

This section demonstrates the feasibility of constructing the HALL D data acquisition (DAQ) system with commercially available hardware and the CODA DAQ framework. Part of the attraction of this solution is that it is easily adaptable to the inevitable advances in computing technology, and would be

ready to take advantage of them without major restructuring. This adaptability will help make it possible to take our Stage 1 (10^7 tagged photons per second) DAQ solution, and move adiabatically into State 2 (10^8/sec). Furthermore, it builds on a framework which has a firm footing at Jefferson Lab already, in particular with multiparticle detection in Hall B.

At 10^7 tagged photons/sec the HALL D first level trigger rate will be about 5 kHz including the hadronic cross-section (1600/sec) and accidental backgrounds. This is a clearly solvable DAQ problem with currently available technology, as we show below. In stage two, with 10^8 photons/sec, the hadronic rate is an order of magnitude larger, but accidental backgrounds, which grow with higher powers of the photon flux, become prohibitive unless more sophisticated triggers are implemented. This, in fact, is an important R&D area for Stage 2, but we need to plan for a DAQ system that can handle at least the anticipated hadronic rate.

Below, we outline a DAQ system which satisfies a design goal of 15,000 events per second with $\approx 80\%$ live time. For a 50,000 element detector with occupancy similar to CLAS in Hall B, we expect an event size of about 5 kB and a resulting data rate of about 75 MB/sec. An event rate of 15 kHz means that on average we must process an event every 67 μs in each stage of the DAQ. To achieve this with 80% live time, either the conversion and readout must complete in less than 13 μs for every event, or there is buffering between conversion and readout processes. In fact, the trigger will use hardware that is able digitize and buffer the data, using "pipeline" architecture, and it becomes the job of the DAQ system to read out this data without introducing any additional dead-time.

7.3.1 Hardware, Data Volume, and Readout

The front-end electronics will be housed in a "VME for Physics" (VMEP) crate, with data read out across the backplane, checked, buffered, and sent to event builders. VMEP is a currently proposed standard based on the ANSI standard VME64x (VME Extensions). Advantages of this format include

- A high maximum throughput of 160 MB/sec.
- Direct bus access for commercial CPUs.
- A large range of commercially available products.

Nuclear and particle facilities at CERN, Fermilab, BNL, and many other labs are using or are planning to use VMEP compatible hardware.

A VMEP crate provides 21 slots in a 19 inch rack format. The system controller CPU will occupy one slot, and one or two others may be empty or not used. Assuming 96 channels per VMEP board, we will need a minimum of $50000/(18 \times 96) = 29$ crates. Experience with CLAS indicates that on average there are 3 hits per slot or 54 hits per crate. Adding another 2 words of CODA header totals 56 words per crate, or 224 bytes/crate/event which translates to 3.36 MB/sec per crate. Currently, the full Fast Ethernet data transfer rates of 11 MB/sec require about half of the CPU time on a Motorola VME computer (MVME 2306 at 300 MHz) so a 15 kHz HALL D event rate would require about 20 percent of this type of system.

The readout time R per event within the CODA DAQ framework can be approximated by the following formula:

$$R = a \ + \ b \ + \ c \times F \ + \ d \times H \tag{7.6}$$

where

- $a \approx 10$ μs is the operating system interrupt latency, although tailoring the system can reduce it to $5 - 8$ μs
- $b \approx 15$ μs is the CODA event processing overhead
- $c \approx 2$ μs is the VMEBUS cycle overhead including addressing and post cycle error checking
- $F = 3$ (buffered mode readout) is the minimum number of VMEBUS access calls required per crate
- $d \approx 0.1 - 0.2$ μs is the VMEBUS readout time per hit
- H is the number of hits to be readout per crate.

This works out to $R \leq 40$ μs per event, assuming that multiple crates are read out in parallel. As the data is buffered, random overlaps are avoided and this introduces no new dead time, so long as the event rate stays below 25 kHz.

7.3.2 Data Transport, Event Building and Archiving

Transport of the data from the front end to one or more event building platforms can be done using existing standardized network hardware. Inexpensive VME CPUs with 100 MBit/sec ethernet network interfaces can be used. These will be connected to an ethernet switch which is also connected to the event builder platforms. Multiple event building and recording components are not currently available in the CODA DAQ framework, but they can be easily implemented.

Tests of CODA on a 4-processor (250 MHz) Sun Ultra 450 computer show that the present event builder software can build 4 KB events at rates exceeding 10KHz, in a mode where the event is built and taken through the event transport system, but not written to disk. The event recorder generally writes to a fast staging disk system. Disk systems with sustained-write speeds of about 100 MB/sec are available today. We expect that by the time we implement this in HALL D , there will be more options commonly available and less expensive. Once on disk, the data will be archived using a Storage Tek Redwood tape system. Presently, individual drives in this system can write at 11 MB/sec and Storage Tek plans that, in less than two years, drives will be available with a capacity of 100 GB and writing at 20 MB/sec. Dedicated optical links will be needed between the hall and the computer center so that the disk system may be mounted by the DAQ computer, unmounted, and written to tape by the laboratory central computing facility. While the first disk is being written to tape, the DAQ system will mount another disk and write to it.

7.3.3 Monitoring and Control

Monitoring and control tasks include online event processing, hardware configuration and control ("slow controls"), bookkeeping, and alarm and messaging systems. These are less demanding tasks than data acquisition in HALL D , and should not present unusual challenges. We plan to follow some examples from Hall B, but to also make use of lessons learned there. In particular, we plan to integrate offline data analysis tools with the online monitoring at the outset. This not only avoids a large duplication of effort, but it also makes it seamless to take software developed on one data set and apply it directly to future runs.

The number of events that can be processed online is largely determined by the number of processors available. A reconstruction fraction between 10% and 100% is reasonable. The low end could be managed with a modest system. The high end would require a substantial online processing farm, but for most monitoring purposes it is not necessary to analyze every event. The choice of the type and number of processors can wait until soon before the system is installed, when prices are lower and performance is better known.

The framework for slow controls should be uniform for all sub-systems in HALL D , but the choice is not obvious. VME-based EPICS works in Hall B, but does not mesh well with the online requirements very well and has proven to be manpower intensive. In fact, a number of Hall B systems do not use EPICS or VME, but instead resort to CAMAC or other options. Other software

possibilities include message-based systems and hardware alternatives include PC or mixed hardware systems. We believe that an open, message-based system that implements a uniform interface to diverse hardware is probably best. Commercial products are currently available that implement this at moderate cost.

Bookkeeping tasks include all recordable activities of the experiment other than raw and calibration data. We expect this will be done using relational and/or object-oriented databases. Current commercial and public domain database technology should be adequate.

The alarm and messaging framework allows sub-systems to communicate their state to monitoring programs and operators. This system needs to be integrated across the entire online, DAQ, and database systems in a simple, uniform manner. The scale and performance requirements of this system are modest, and similar to other projects in progress or completed at Jefferson lab.

Chapter 8

Data handling plan

Given the rates at which we plan to collect data with the HALL D detector, it will be important to develop a plan for efficient data handling and and processing. The HALL D Collaboration is aware of the need for such a plan and will propose a plan in the coming months.

Chapter 9

Monte Carlo simulations

9.1 Introduction

Prelminary Monte Carlo work has been done to study the expected resolution of the charged particle detectors proposed for HALL D . Since significant experience in calorimetry exists from BNL E852 and TJNAF RADPHI actual results from those experiments have been used for this report and Monte Carlo development in this area is not as complete. The emphesis in the work done to date is on creation of a useful and flexible system of programs that will allow design work to proceed quickly. Realistic models of detectors and materials are used so that expected resolutions can be estimated. An overview is presented below.

9.2 Monte Carlo Framework

A Monte Carlo framework has been developed to understand the performance of key aspects of the HALL D detector systems. This framework is in general a collection of modules, each serving some particular function. These modules consist of individual programs and library routines which use common event I/O formats. Figure 9.2.1 illustrates this modular structure.

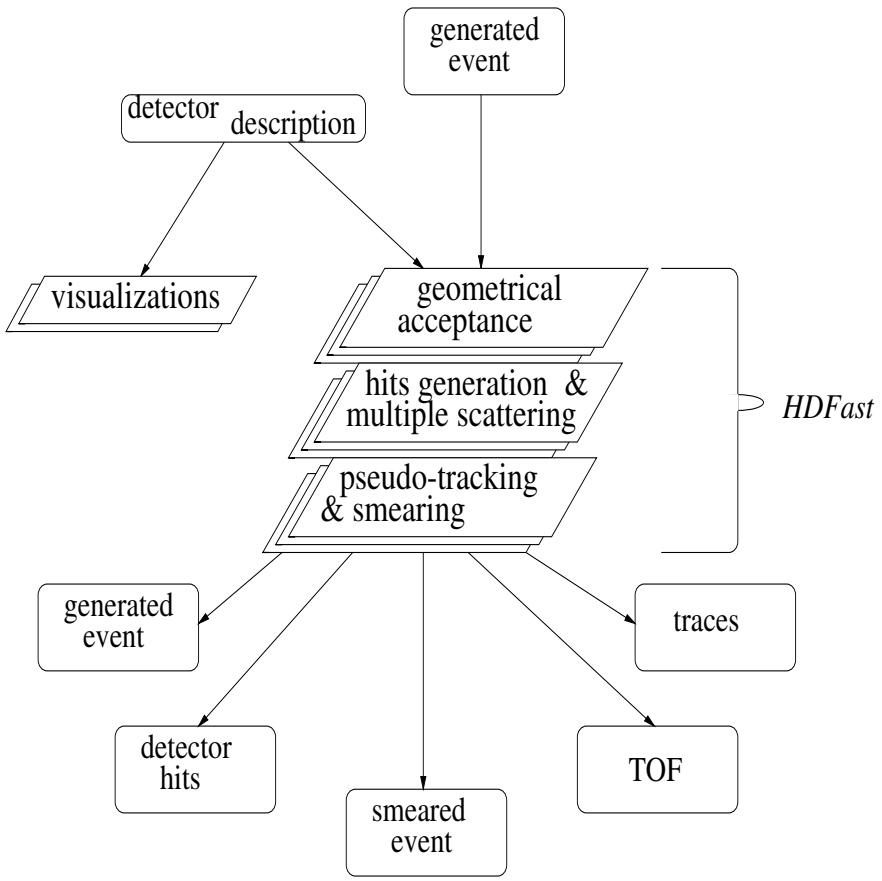

Figure 9.2.1 An illustration of the HALL D Monte Carlo modular pipelining

First, a Monte Carlo four-vector generator is used to create phase-space distributed events. Next is the detector simulation, HDFast, which is a fast and flexible simulation program based upon the MCFast framework developed by the simulation group at Fermilab. The Monte Carlo output includes (but is not limited to) the following data objects:

- generated event
- detector hits
- resolution modified (smeared) event
- time-of-flight information
- dE/dx information

- threshold Čerenkov information

- particle trajectory information

Monte Carlo events can be generated using the program *genr8*[125] or *cwrap*[126]. Both programs generate peripheral phase space Monte Carlo events where events can be produced which describe a complex decay chain of intermediate states. Both meson and baryon decay chains are allowed, but with a limiting assumption of a t-channel production process. The four-momentum transfer squared distribution follows that of

$$\frac{d\sigma}{dt} \propto e^{-b|t|}$$

where the user defines the t-channel slope or $d\sigma/dt$ can be specified by an input histogram.

HDFast is a fast and flexible simulation program based upon the MCFast framework developed by the simulation group at Fermilab[127]. MCFast consists of a set of modularized Monte Carlo library routines; it is designed to perform parameterized tracking by assembling a covariance matrix for each track that takes into account materials, efficiencies, and resolutions for all measurements planes, and use this matrix to smear the track parameters randomly. In principle, the distribution of smeared tracks produced by this method would be similar to the distribution of real tracks that were measured by a real detector(with the same parameters) and analyzed with an idealized track fitting procedure[127].

HDFast is controlled via a set of user routines which act as an interface to the MCFast framework. They control the tracking and smearing of the four-vectors, in addition to the booking and filling of monitoring ntuples and histograms. The detector geometry is controlled by an ascii file which is read in during program execution. This allows the user to quickly create or modify the detector geometry without the need to recompile the executable. In addition, a ROOT[128] macro was developed which reads in the ascii geometry file and displays a two-dimensional visualization (see Figure 9.2.2 below) of the detector configuration.

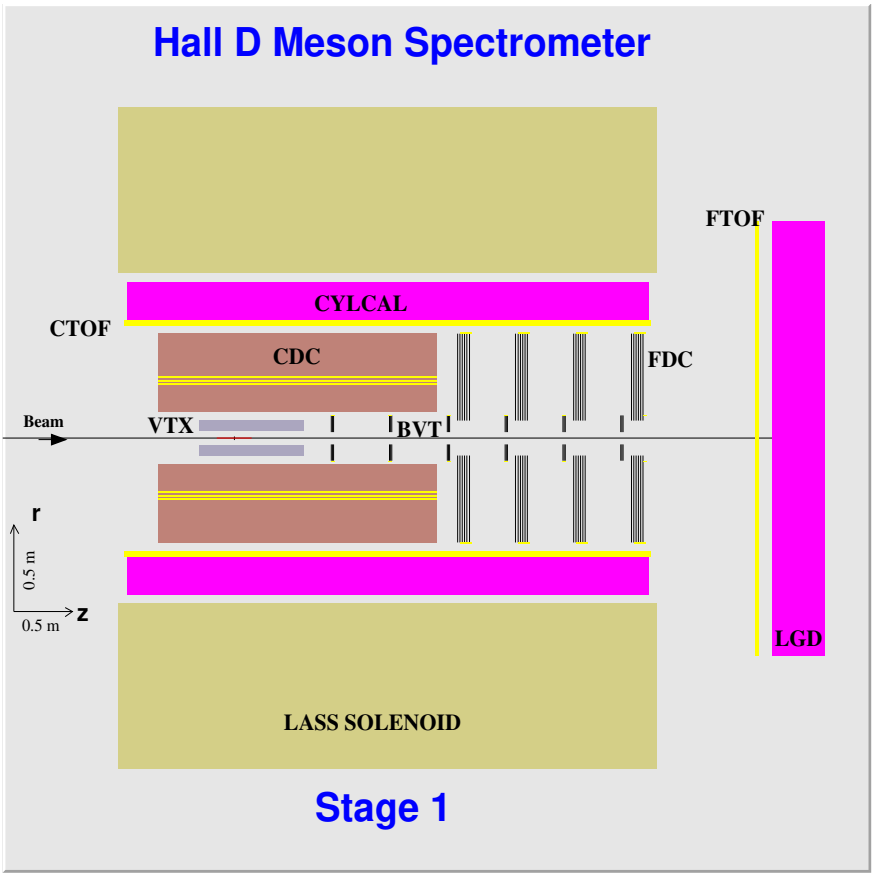

Figure 9.2.2 A schematic of a straw-man detector for HALL D Stage 1.

The motivation for using the MCFast framework is to facilitate the study of design changes and detector configurations. This does not exclude the use of a GEANT based simulation. MCFast provides routines for converting MCFast geometry to GEANT. Eventually, a GEANT4 based simulation will be incorporated into the HALL D Monte Carlo framework.

Chapter 10

Data Analysis

10.1 Introduction

In order to identify the J^{PC} quantum numbers of a meson, it is necessary to perform a *partial wave analysis*. In the simplest terms, a partial wave analysis is an attempt to determine production amplitudes by fitting decay angular distributions. The fit may include information on the polarization of the beam and target, the spin and parity of the resonance, the spin and parity of any daughter resonances and any relative orbital angular momenta. The analysis seeks to establish both the production strengths and the relative phase motion between various production amplitudes. Phase motion is critical in determining if resoanance production is present.

While the implementation of a partial wave analysis is in principle straightforward, there are both empirical and intrinsic difficulties. Empirically, instrumentation effects, such as detector acceptance and resolution, can conspire to make one distribution look like another. These similar distributions lead to *leakage* in the partial wave analysis. Here, cropping, smearing, or incorrect acceptance corrections of two physically different distributions may lead to distributions which are apparently indistinguishable. These difficulties can be minimized by properly designing the experiment. Full angular coverage in the distributions can be achieved by using a nearly 4π detector with excellent resolution. In addition, high statistics are critical to be able to accurately separate these partial waves. A thorough partial wave analysis requires nearly 4π coverage, excellent resolution, high statistics and a very good understanding of the detector.

The PWA method is subject to intrinsic mathematical ambiguities for certain final states. Two or more different choices of amplitudes lead to identical

observables. Here there are at least two approaches. The first assumes some a priori physics knowledge that allows one to choose one solution over another. The second, and cleaner approach is to simultaneously examine several final states to which the resonance can decay. While the distributions may be confused in one final state, such as $\eta\pi$, they are likely to be absent or different in a second such as $\rho\pi$. This latter approach assumes that the detector has been optimized for many different final states, and that relative normalizations between these are understood.

This latter approach of looking at multiple final states not only would allow one to separate different waves, but in itself yields key information about the relative decay rates of mesons. It is this latter information that is critical to understanding the underlying wave functions of the mesons — their content, and mixing with other states. This ability to accurately measure many final states, and perform a simultaneous partial wave analysis is a key feature of the Hall D spectrometer for doing excellent spectroscopy.

The use of photon polarization will also allow one to both simplify the analysis parameterization, as well as access additional information on the production of mesons. It will also provide key checks on the stability of the analysis itself. While circularly polarized light may yield some information in a few special cases, the true gain comes from linear polarization. Linear polarization defines a *new spatial direction* beyond the photon direction, while for circular polarization, the polarization and the momentum are in the same direction. Secondly, linearly polarized light is a coherent sum of circularly polarized light, which leads to new interference terms.

Finally, there is always a problem of background in a partial wave analysis. This limits one's ability to measure phase motion, and can be particularly severe in a region of dense overlapping resonances. Backgrounds involve a different final state accidently reconstructing as the channel under study. Either a particle is missed by the detector, or when putting the final state back together, multiple interpretations are possible. This can be minimized with a good 4π detector with high efficiency for detecting all final state particles with good resolution. One needs all particles to be reconstructed well enough to allow for a complete kinematical identificaiton of a specific final state.

10.2 Beam and final state normalizations

It will be necessary to show, in the first results from Hall D, that our experiment produces results that are consistent with previous investigations, albeit with much greater statistical precision. These will include total cross sections

(at various photon energies) for various inclusive multi–particle photoproduction reactions [129], invariant mass distributions and differential cross sections for exclusive reactions [130, 131] and density matrix element determinations in processes for which polarized beams have been available [132].

Each of the measurements cited above have been carried out with relatively low flux photon beams (for which the beam normalization is rather straightforward) and using bubble chambers for particle detection (which therefore provide excellent, flat acceptance functions). Moving to high intensity beams and sophisticated electronic detectors, while leading to enormous gains in statistical precision, makes it more difficult to accurately determine normalizations. Since one of our main goals is to determine such things as relative branching ratios and production cross sections of new states, it is important to establish consistent connections with these previous measurements. Furthermore, it is likely that our experiment will run with different triggers for different running periods, and these data sets need to be merged as seamlessly as possible. All of these goals will need accurate controls of beam normalization and detector acceptance, as well as a clear determination of their inherent systematic uncertainty.

10.2.1 Photon beam flux

Beam normalization requires a two step process, each of which should be tied in with measurements in the detector itself. In the first step, a low flux photon beam is intercepted by a detector which absorbs the full beam. (It is not difficult to make a detector with essentially 100% detection efficiency for multi GeV photons, and whose losses can be accurately determined with well established simulation programs.) By measuring the fraction of tagged photons, as a function of energy, which are detected by the total absorption counter, we can determine the efficiency to transport these tagged photons through the various beam–line collimators and through the detector itself. This can be further correlated with the detection of real photoproduction reactions.

The second step requires a device which can live in the full beam flux, and which can be cross calibrated with the low flux measurement in the total absorption counter. The easiest way to accomplish this is with a device that uses some small radiation length foil to convert a tiny fraction of the beam to e^+e^- pairs. If these pairs are then detected, preferentially with some energy discrimination using a crude magnetic spectrometer system, then this rate will serve our purpose. In addition, such a pair spectrometer allows for a continuous online monitor of the beam flux during the course of a run. Such a monitor

would be very sensitive to, for example, an inadvertent collimator adjustment which changes the overall beam by a small, but important, amount.

We emphasize that coherent bremsstrahlung, which will be necessary for polarized photons as well as for optimizing the photon beam energy, will make the flux normalization more difficult than what has been done so far at Jefferson Laboratory. The energy spectrum is no longer smooth, and the detailed shape is very sensitive to collimation. The collimation in turn is sensitive to the beam steering, which is likely to fluctuate over the course of a data set. All of these fold into our knowledge of the photon beam polarization itself, which we will be determined in large part on the basis of calculations.

Some techniques are also available for monitoring the high flux photon beam polarization directly, although they are not particularly useful for accurately determining the *degree* of polarization. It may be possible to use some techniques designed for low flux beams, but these need to be investigated further.

10.2.2 Particle detection efficiency and acceptance

Monte Carlo simulation will be our primary tool for evaluating detector acceptance and for applying it to data analysis techniques, in particular for the partial wave analysis. However, we need to calibrate, and otherwise confirm, the simulation against real data samples, under usual running conditions.

Some simple reactions have both large cross sections (which are already well–measured) but that also provide a redundant way to check other aspects of the detector. For example, $\gamma p \to \pi^+\pi^- p$ is fully dominated by $\gamma p \to \rho^0 p$ at our energies and its density matrix elements with polarized beam are known [133, 132, 134, 135]. Any two of the three charged particles in this final state can be identified and detected, and one can ask for the probability that the third is also seen. Using the enormous statistical power of our expected sample, we will be able to check details of the acceptance function as determined by the Monte Carlo, using very small and directed phase space bins. Measuring the cross section and density matrix elements in all four topologies (i.e., any one of the three particles missing and all three of them detected) must yield consistent results with each other and with existing data.

Another well known benchmark is $\gamma p \to \pi^+\pi^-\pi^0 p$ which will be dominated by $\gamma p \to \omega p$ [136]. Detection of the three charged particles allows us to determine the direction and energy of the π^0, and therefore to check its detection efficiency and resolution in the electromagnetic calorimeter. It is easy to see how one can extend these arguments to more complicated systems. For example, a measurement of $\gamma p \to \eta p$ using the same topology as for ω

production must yield the same results as for $\eta \to \gamma\gamma$, using the well known relative branching ratios for η decay. Many other examples are obvious, and will be exploited.

We emphasize that all of these "calibration" measurements can be bootstrapped into new physics results, extending our present knowledge of some of the most basic photoproduction reactions. All of these new results will be important systematic checks on the more sophisticated analyses that will be possible given our increased statistical accuracy.

10.3 The Role of photon linear polarization

As discussed in section 4.3 the spin–1 nature of the photon allows one to probe helicity or spin structure of production amplitudes. The spin information has been crucial, for example in establishing the dominance of s–channel helicity conservation in ρ photoproduction, studies of violation thereof [133, 137], and in determining the importance of rescattering contribution, *i.e.* Drell–Söding processes [138, 139]. These latter rescattering contributions are important even at high energies [140, 141, 142] and through interference with the diffractive amplitude, they distort the mass distribution of the resonance from the Breit–Wigner shape and contribute to helicity–non–conservation [133, 137]. However, in order to take full advantage of the polarization information in the photon beam it is necessary to have access to linear polarization.

There are two main features that are enabled by linear polarization [93]. First, it allows one to access the largest set of spin–density matrix elements or partial wave amplitudes. This is important from the point of view of both, partial wave analysis, which as discussed earlier enables one to identify properties of the produced resonances, as well as for studies of production mechanisms of those resonances. Secondly, it allows one to identify naturality of the exchanged particle for t–channel dominated reactions. The former follows from considering transformation properties of the production amplitudes under parity. Symmetry under parity relates two production amplitudes with opposite helicities. If the production amplitude is dominated by a t–channel exchange, which at high energies is the case to leading order in t/s, then using parity one can further relate amplitudes with helicities flipped independently at the two, photon and nucleon vertices. With the intrinsic properties under parity, (determined by naturality) of all incoming and outgoing particles fixed, this relationship depends on the naturality of the exchanged particle. Thus by measuring appropriate spin–density matrix elements it is possible to discriminate between different exchanges. Conversely, if the properties of the t–channel are

known, which might be the case at low t with one-pion-exchange dominance, then linear polarization enables one to fix the naturality of the produced resonance. As discussed in section 4.3 photons polarized perpendicular to the production plane under one-pion-exchange will yield (un)natural resonances produced with polarization (perpendicular)parallel to the production plane.

These features of linear polarization and its impact on partial wave analysis are best illustrated using vector meson production as an example [93]. Consider the reaction $\gamma p \to Vp$ on an unpolarized target with the subsequent decay of a the vector mesons into two pseudoscalar mesons, $V \to PP$ as in $\rho^\circ \to \pi^+\pi^-$ or $\phi \to K^\circ\bar{K}^\circ(K^+K^-)$. There are typically three reference frames used to study such reactions, differing by the definition of the spin quantization axis: the *Gottfried–Jackson frame*, the *helicity system* and the *Adair system*. It is useful to study the angular distribution of the resonance's decay products in all three of these systems. Depending on the dynamics of the production process, production amplitudes, and in particular spin–density matrix elements the physics will appear in a characteristic form in one of the three systems. For example, if t–channel exchange dominates, the spin–density matrix is best analyzed in the Gottfried–Jackson frame. However, to study a dominantly s–channel helicity conserving reaction, one would use the helicity system.

In vector meson photoproduction, the angular dependence of the two pseudoscalars is fully determined in terms of 17, real spin density matrix elements, $\rho^\alpha_{m'_V,m_V}$, $\alpha = 0,\cdots 4$, $m'_V, m_V = \pm 1, 0$ which are defined as in equation 10.1.

$$\rho^\alpha_{m'_V,m_V} = \sum_{m'_N,m_N,m'_\gamma,m_\gamma} A^*(m'_N,m_N,m'_V,m'_\gamma)\sigma^\alpha_{m'_\gamma,m_\gamma}A(m'_N,m_N,m_V,m_\gamma) \tag{10.1}$$

Here m_N, m_V, m_γ refer to spin projections of the nucleon, vector meson and the photon respectively, and σ^α are the four Pauli matrices. Using the angular dependence of the vector meson decay products with unpolarized photons one only has access to ρ^0. Using circular polarization, one has access to ρ^0 and ρ^3, and finally with linear polarization to ρ^0, ρ^1 and ρ^2. It turns out that measurement of ρ^1 and ρ^2 simultaneously is necessary for identification of t–channel naturality thus implying the need for linear polarization. This can be inferred for example from the measurement of parity asymmetry, P_σ

$$P_\sigma \equiv 2\rho^1_{1,-1} - \rho^1_{0,0} = \frac{\sigma^N - \sigma^U}{\sigma^N + \sigma^U}, \tag{10.2}$$

where $\sigma^{(U)N}$ are the cross sections corresponding to the (un)natural parity t–channel exchanges. Another common observable is the Σ–asymmetry, defined

in terms of the cross sections for a symmetric decay ($\theta = \frac{\pi}{2}, \phi = \frac{\pi}{2}$) with the two pseudoscalars emerging in the plane of the photon polarization, $\sigma_{||}$, and perpendicular to it $\sigma_{\perp}$,

$$\Sigma = \frac{\sigma_{||} - \sigma_{\perp}}{\sigma_{||} + \sigma_{\perp}} = \frac{\rho^1_{1,1} - \rho^1_{1,-1}}{\rho^0_{1,1} - \rho^0_{1,-1}}. \tag{10.3}$$

It turns out that the difference between P_σ and Σ asymmetries is also a measure of the helicity–non–conservation.

10.4 Description of the partial wave analysis

Parital Wave Analysis is the technique used in hadron spectroscopy to extract spin–parity and decay properties of resonances produced in high energy interactions. The general concept is to parameterize the observed angular distributions in terms of resonance production amplitudes which span the appropriate space. Although many such parameterizations are possible, we choose an expansion in terms of resonances and their appropriate decay couplings. This method also allows the direct assertion of relevant conservation laws, and also permits the direct interpretation of results in terms of resonance production and decay strengths.

The program which is currently being developed to analyze electroproduction and photoproduction data at CEBAF, was originally developed for the analysis of hadroproduction data at Brookhaven National Laboratory [143]. This program uses the extended maximum likelihood method [124] to fit the production amplitudes to the observed intensity distribution.

10.4.1 General description

The program is based on the partial wave formalism described above. The angular distribution is a squared sum of amplitudes taking in account initial and final state spin states as given in 10.4.

$$I(\tau) \propto \sum_{\alpha} \left| \sum_{\beta} {}^{\alpha}\psi_{\beta}(\tau) \right|^2 \tag{10.4}$$

The variable τ represents the set of variables necessary to define a configuration of the final state being investigated, and generally includes the angles of decay products in various reference frames, and the masses of decay products. For example, for the final state $\pi^+\pi^-\pi^0$, the system is described by a set of decay

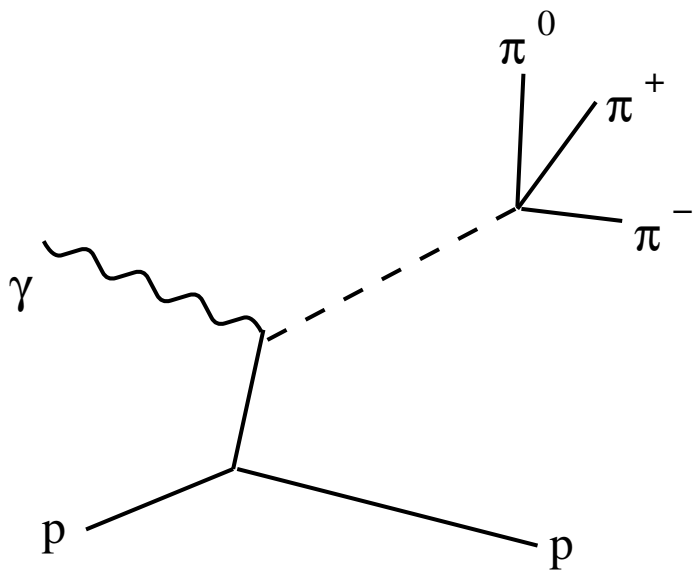

Figure 10.1: Photoproduction of a charged three pion system off a hydrogen target.

angles, θ and ϕ of the $\pi^+\pi^-$ system in the 3 π center–of–mass system, and the decay angle of the π^+ in the $\pi^+\pi^-$ center–of–mass, and the mass of the $\pi^+\pi^-$ pair, for a given 3–π mass. The subscript β represents the definition of a specific partial wave, and α specifies parameters that do not interfere, for example any external spins that are not measured.

In a peripheral production experiment, the amplitudes of the can be drawn as shown in Figure 10.1. A fundamental tenet of partial wave analysis is that the process factories, i.e. the resonance is produced, propagates for some time, and then decays. The decay amplitude depends only on the resonance parameters, up to a constant, and is thus calculable. The total amplitude ${}^{\alpha}\psi_{\beta}$ can be written as the product of the production amplitude V and the decay amplitude A:

$$ {}^{\alpha}\psi_{\beta} \;=\; {}^{\alpha}V_{\beta}\;{}^{\alpha}A_{\beta}(\tau)\;. \tag{10.5} $$

As as way of illustration, consider our example of the photoproduction of 3 pions from an unpolarized photon beam on an unpolarized hydrogen target, Figure 10.1. In this case, the non–interfering components of the process come from the external spins in the process, i.e. the incident photon spin, the target proton spin, and the recoil proton spin. The description of the partial waves includes the J^P of the produced resonance, the mass of the $\pi^+\pi^-$ pair, the

relative orbital angular momentum between the $\pi^+\pi^-$ pair and the bachelor π°, the orbital angular momentum between the π^+ and the π^-, and the J_z of the produced resonance. As the decay of the resonance is into only pseudo–scalar particles, the decay amplitude A is not labelled by the spin index α. The angular distribution can thus be written as in equation 10.6.

$$I(\tau) \;=\; \sum_{\lambda_\gamma,\,\lambda_n,\,\lambda_{n'}} \left| \sum_{\beta} {}^{\alpha}V_{\beta}\; A_{\beta}(\tau) \right|^2 \tag{10.6}$$

where the λ's are the helicities of the photon, target nucleon, and recoil nucleon, respectively.

The likelihood function for finding 'n' events in a given bin with a finite acceptance $\eta(\tau)$ is given by a product of probabilities:

$$\mathcal{L} \propto \frac{\bar{n}^n}{n!} \mathrm{e}^{-\bar{n}} \prod_i^n \frac{I(\tau_i)}{\int I(\tau)\eta(\tau)\, dLIPS} \tag{10.7}$$

where $dLIPS$ is the differential lorentz invariant phase space element. Neglecting factors which depend on n, the $\ln(\mathcal{L})$ may be written as:

$$\ln(\mathcal{L}) \propto \sum_i^n \ln I(\tau_i) - \int I(\tau)\, \eta(\tau)\, d\mathrm{LIPS}. \tag{10.8}$$

Since $I(\tau)$ is an expansion in terms of partial waves, the acceptance correction in the second term is done wave–by–wave *not* event–by–event. This allows the full statistics of the Monte–Carlo to used in the acceptance calculation, rather than just the events in a kinematic bin. In addition, the fit can be done even if there are holes in the acceptance, at the cost of possible ambiguities being introduced into the fit.

10.4.2 Decay amplitudes

The amplitude for the decay of a particle with spin J and $J_z \;= M$ into two particles with helicities λ_1 and λ_2 in the resonance center–of–mass system is given by [144]:

$$A = < \vec{p}\lambda_1; -\vec{p}\lambda_2 \mid \mathcal{M} \mid JM > = \; F^J_{\lambda_1\lambda_2} \mathcal{D}^{*\,J}_{M\,\lambda}(\phi, \theta, 0) \tag{10.9}$$

Calculation of the decay amplitudes for a resonance is done recursively within the isobar model, regarding the n–body final state as a result of a series of sequential, generally 2–body, decays through intermediate isobar states. The

total decay amplitude is the amplitude for the resonance to decay into its intermediate children times the amplitude for each of its children to decay.

The initial decay of the resonance is calculated in the Gottfried–Jackson frame. This frame is a rest frame of the resonance with the z axis along the incident beam axis, and the y–axis is defined by the production plane. Each subsequent decay is calculated in the helicity frame, that is the rest frame of the decaying particle with the z–axis in the direction of the parent particle from the previous frame.

10.4.3 Initial state polarization

The intensity distribution, as written in 10.6, shows the familiar sum over final states and average over initial states as the sums over external spins. These sums can be handled explicitly as shown or as constraints on the structure of the spin density matrix of the intermediate state produced in the reaction. Imposing additional constraints that are known *a priori*, such as hermiticity and parity conservation, leads to a minimal number of independent fit parameters.

The spin density matrix of this state is written in terms of the production amplitudes as:

$$^{\alpha}\rho_{\beta\beta'} = V_{\beta}V^{*}_{\beta'} \tag{10.10}$$

meaning that when the physical constraints mentioned above are taken into account, ρ is block diagonal with α blocks.

The intensity distribution can then be written as

$$I(\tau) = \sum_{\alpha} A_{\beta}(\tau)\ {}^{\alpha}\rho_{\beta\beta'}\ A^{*}_{\beta'}(\tau)\,, \tag{10.11}$$

where the sums over spins have thus been absorbed into the density matrix. If none of the exterior spins are known, the density matrix must be symmetric in those spin indices. Polarization of the initial state spins, however, impose additional constraints on the structure of the density matrix and will allow us to take advantage of asymmetries produced.

10.4.4 Joint production of excited baryons and mesons

In the kinematic region of HALL D it is probable that baryon resonances will be produced in addition to the meson states we have been discussing. Processes such as the two shown in Figure 10.2 will interfere wiht each other and they must be taken into account in the analysis.

In general this could lead to ambiguities, since the baryon states can be described as an infinite sum over meson states. In practice, however, the sum

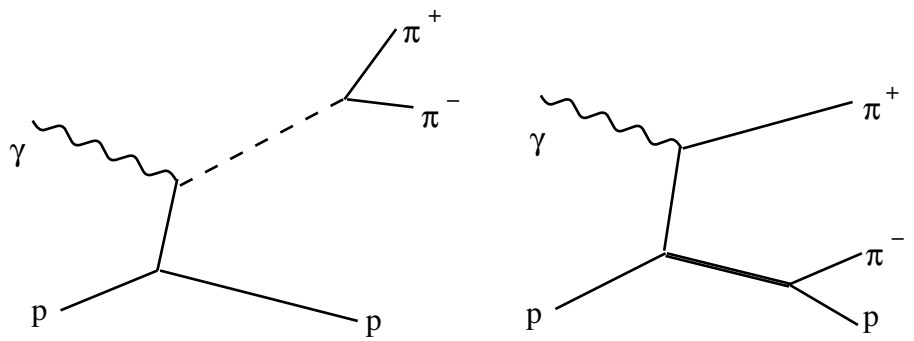

Figure 10.2: Example of interfering baryon and meson processes.

over meson states is truncated to a finite number of resonances, and will not well describe the distribution due to the baryon resonance. Hence, in order to get a good description of the intensity distribution, the baryon resonances must be included explicitly. Effects of ambiguities are mitigated at the cost of requiring an physically motivated *ansatz*, *i.e.* truncating the set of waves to the minimal set required by the fit. The impact of any ambiguities created will vary with the reaction being studied, but can be well determined using Monte–Carlo methods.

Chapter 11

Milestones

The HALL D Collaboration recognizes the need to develop milestones and these will be developed after consultation with and guidance from the Jefferson Lab management and PAC.

Chapter 12

Costs

The following tables summarize the cost estimates for the various subsystems of the STAGE 1 HALL D detector and some of the civil construction associated with the HALL D project. All costs are given in thousands of dollars.

Subsystems listed below include the barrel calorimeter (BCAL), the data acquisition (DAQ), time-of-flight (TOF), Cerenkov counter, central drift chamber (CDC), forward drift chamber (FDC), and the barrel vertex tracker (BVT - also referred to as the start counter in the text).

It is important to note that these esimates are very preliminary and partial. These tables are presented in the spirit of a 'snap shot' of where we are to date in costing this STAGE 1 detector. More reliable extimates will be developed in the coming months.

In addition, the HALL D Collaboration is working with the Jefferson Lab civil construction group to develop more detailed and realistic cost estimates for the beamline tunnel, tagger building, and the HALL D building by mid-February, 1999.

With the above caveats in mind about the preliminary and partial nature of these estimates, the STAGE 1 detector costs total to approximately $ 12M and the beam and building costs total to approximately $ 6M.

BCAL item	Cost
Scintillating fiber	750
Lead	65
Rolling labor	40
Glue and supplies	10
Tooling	100
Weaving labor	250
Mechanical support	100
Lightguides	60
PM's	180
Bases	90
Magnetic shielding	30
High voltage	60
Discriminators	90
ADC's	90
TDC's	90
Cables	90
Crates	48
Calibration system	100
Subtotal	2243

Table 12.1: Barrel Calorimeter (BCAL) cost estimates.

DAQ Item	Quantity	Unit Cost	Total
SBC CPU	35	3	105
Ethernet switch	2	20	40
DAQ SMP	2	50	100
DAQ Raid disk	4	40	160
CC Raid disk	4	40	160
Silo upgrades			1000
Analysis Farm PC's	250	2	500
Tape media	15000	0.1K/Tb	1500
Subtotal			3565

Table 12.2: Cost estimates for data acquisition (DAQ) and related items.

TOF Item	Cost
Scintillator	20
PM's	100
Bases	20
Magnetic shields	10
ADC's	20
TDC's	20
Support frame	100
Subtotal	290

Table 12.3: Cost estimates for the time of flight (TOF) system and related items.

Cerenkov Item	Cost
Primary Mirrors	18
Mirror setup	50
Secondary optics	7
PM's	36
Bases	4
Magnetic shields	2
ADC's	4
Housing/support	200
Subtotal	321

Table 12.4: Cost estimates for the Cerenkov counter and related items.

CDC item	Cost
Support end/shells	50
5200 straws	250
Cathode strip prints	15
Connectors	bg10
Cabling	50
Assembly	150
Subtotal	525

Table 12.5: Central drift chamber (CDC) cost estimates.

FDC item	Cost
Support systems	50
Wire	25
Cathode strip prints	50
Connectors	30
Cabling	50
Assembly	100
Subtotal	305

Table 12.6: Forward drift chamber (FDC) cost estimates.

BVT item	Cost
Support systems	20
Wire	5
Cathode strip prints	10
Connectors	10
Cabling	25
Assembly	50
Subtotal	120

Table 12.7: Barrel vertex tracker (BVT) cost estimates.

Component	Cost
CDC	525
FDC	305
BVT	120
VTX	100
TDC's (8056)	800
ADC's (12000)	1200
High voltage	250
Total	3300

Table 12.8: Summary of tracking subsystem costs.

Subsystem	Cost
Solenoid move	750
Target	100
BCAL	2243
Tracking	3300
Forward Calorimeter	1300
TOF	290
Cerenkov counter	321
DAQ	3565
Trigger	300
Total	12,169

Table 12.9: Total detector cost estimates.

Item	Cost
Beamline tunnel	1700
Hall D	500
Control room	120
Beam elements	2000
Tagger system	1500
Detector	12,169
Total	17,989

Table 12.10: Summary of costs.

Chapter 13

Management plan

The HALL D Collaboration recognizes the need to develop a management plan as part of a WBS. There are models for such plans and in the coming months the HALL D Collaboration will develop a management plan.

List of Figures

3.1 A level diagram showing conventional nonets and expected masses of glueballs, hybrids and molecular thresholds. 11

4.1 Generic diagrams for hard photon production from a high energy electron beam. The symbol $\times$ represents either a static charge distribution, in the case of virtual photons in the initial state (i.e. bremsstrahlung) or an optical cavity, in the case of real photons in the initial state (i.e. Compton scattering) The + denotes the fact that this leading order amplitude is actually the sum of two diagrams, one with the initial state photons attached to the incoming electron leg and one with it attached to the outgoing electron. 30

4.2 Kinematic limits on production properties for several choices of beam energy. (left) Maximum mass for particle X as a function of incident photon energy in the reaction $\gamma p \to Xp$. (right) The minimum value of $|t|$ as a function of the mass of particle X in the reaction $\gamma p \to Xp$ for various values of incident photon energies. 31

4.3 Dalitz plot boundaries for the reaction $\gamma p \to \pi\pi p$ (left) and $\gamma p \to \eta\eta p$ (right) for incident photon energies of 4, 8 and 12 GeV. 32

4.4 Plots of the mass distribution of 4 produced resonances in the reaction $\gamma p \to Xp$ taking into account the t_{min} effect for an incident photon energy of 6 GeV (upper left), 8 GeV (upper right), 10 GeV (lower left) and 12 GeV (lower right). (see the text for details). 33

4.5 Schematic plan view of the photon beam line, shown in the horizontal plane as viewed from above. The objects in this figure are not drawn to scale. 40

5.1 An overview of the STAGE 1 HALL D detector. The major subsystems are labeled and are discussed individually in the text. 64
5.2 Sketch of Barrel Calorimeter made from bars of Pb/SciFi material. (a) perspective view; (b) closeup of end with suggested readout segmentation for one of 48 bars; (c) side view showing approximate locations of PMTs. 75
5.3 The Stage 1 tracking elements. CDC is a cylindrical drift chamber, VTX is a vertex chamber with fast trigger capabilities, BVT are cylindrical drift chambers close to the beam line, and FDC are forward planar drift chambers. 77
5.4 Momentum versus polar angle for all charged particles in $\gamma p \to K^+K^-\pi^+\pi^-p$ data sets. Figures **a** and **b** are the distributions for all particles for E_γ = 6 GeV and E_γ=10 GeV respectively. Plots **c** and **d** show momentum versus angle for the most forward particle in both cases. 79
5.5 This figure shows the number of full circles made by charged particles in the magnetic field. The limit line corresponds to $p_\perp = 0.3$ GeV/c tracks. The approximately horizontal lines indicate when the particle can make the indicated number of turns without leaving the magnet. 80
5.6 The resolution as a function of angle plotted for several total momentums. The four plots correspond to the four detector designs shown in Fig. 5.3. The large spike at about 35° in **a** that moves forward in **b** and **c** corresponds to the transition region between the central cylindrical chamber and the forward planar chambers. 82
5.7 Missing mass from the reaction $\gamma p \to K^+K^-\pi^+\pi^-\pi^\circ$ where the π° is assumed missing. **a** is for 0.1% beam energy resolution, while **b** is a plot of the missing mass resolution as a function of the beam energy resolution. 83
5.8 Tracking resolution as a function of angle and momentum. The left–hand figure has $200\mu m$ resolution in the CVC, while the right-hand one has $1000\mu m$ resolution. 84
5.9 Effective mass distribution for multi-photon cluster events in the Radphi experiment test run. Plot **a** is for $\pi^0\gamma$ events. Plot **b** is for $\eta\gamma$ events. Plot **c** is for $2\pi^0$ events. Plot **d** is for $3\pi^0$ events. 101

6.1 An overall view of the site modifications. 110
6.2 A elevation view of the modifications. 110

6.3 A detailed elevation view of the tagger buliding 111
6.4 A detailed elevation view of HALL D 111

7.1 Total cross section for $\gamma p \rightarrow$ *hadrons* as a function of photon energy. 114
7.2 Rates for true hadronic triggers and accidental coincidences. . 117
7.3 A schematic diagram of the HALL D trigger. 118

10.1 Photoproduction of a charged three pion system off a hydrogen target. 138
10.2 Example of interfering baryon and meson processes. 141

List of Tables

3.1 Predicted partial widths of the 1^{-+} exotic hybrid at 1.6 GeV/c^2 decaying into $b_1\pi$. The three sets of numbers in the second column show the sensitivity to different model parameters. . 16

3.2 Predicted and observed partial widths (in MeV/c^2) of the two 1^{--} $s\bar{s}$ states $2^3S_1(1680)$ and $^3D_1(1850)$. 23

4.1 Figure of merit of various materials that might be used as a coherent bremsstrahlung radiator. This table is reproduced from Table 2 in H. Bilokon *et al.* 48

5.1 Summary of characteristics of the solenoid in the LASS configuration 65

5.2 A summary of the tracking chamber parameters. The z values under *Length* give the smallest and largest z of the combined system. The z resolution for the *cdc* comes from $500\mu m$ cathode strips on the inner and outer shell, and $\pm 6^\circ$ stereo layers. The VTX chamber is expected to have z resolution through stereo layers. The z resolution of the planar chambers is assumed to be given by there orientation in space. 76

5.3 Maximum total momentum as a function of angle for both E_γ of 6 and 10 GeV. 78

5.4 A summary of the electronic channels in the detector components. 85

12.1 Barrel Calorimeter (BCAL) cost estimates. 146

12.2 Cost estimates for data acquisition (DAQ) and related items. . 146

12.3 Cost estimates for the time of flight (TOF) system and related items. 147

12.4 Cost estimates for the Cerenkov counter and related items. . . 147

12.5 Central drift chamber (CDC) cost estimates. 147

12.6 Forward drift chamber (FDC) cost estimates. 148

12.7 Barrel vertex tracker (BVT) cost estimates. 148

12.8 Summary of tracking subsystem costs. 148
12.9 Total detector cost estimates. 149
12.10Summary of costs. 149

Bibliography

[1] Stephen Godfrey and Jim Napolitano. Light meson spectroscopy. hep-ph/9811410; submitted to Rev. Mod. Phys.

[2] Peter Minkowski and Wolfgang Ochs. Identification of the glueballs and the scalar meson nonet. hep-ph/9811518.

[3] T.Barnes, F.E.Close, P.R.Page, and E.S.Swanson. *Phys. Rev.*, D**55**:4157, 1997.

[4] H. Nielson and P. Oleson. *Nucl. Phys.*, **B61**:45, 1973.

[5] Y. Nambu. *Phys. Rev.*, D**10**:4262, 1974.

[6] N. Isgur and J. Paton. *Phys. Rev.*, D**31**:2910, 1985.

[7] T. Barnes. PhD thesis, Caltech, 1977.

[8] P. Hasenfratz, R.R. Horgan, J. Kuti, and J.M. Richard. *Phys. Lett.*, **95B**:299, 1981.

[9] D. Horn and J. Mandula. *Phys. Rev.*, D **17**:898, 1978.

[10] T. Barnes. *Z. Phys.*, C**10**:275, 1981.

[11] J. Cornwall and A. Soni. *Phys. Lett.*, **120B**:431, 1983.

[12] G.S. Bali, K. Schilling, and C. Schlichter. *Phys. Rev.*, D **51**:5165, 1995.

[13] A.P. Szczepaniak and E.S. Swanson. *Phys. Rev.*, D **55**:3987, 1997.

[14] T. Barnes, F.E. Close, and F. De Viron. *Nucl. Phys.*, **B224**:241, 1983.

[15] M. Chanowitz and S. Sharpe. *Nucl. Phys.*, **B222**:211, 1983.

[16] P.Lacock *et al.* (UKQCD Collaboration). *Phys. Lett.*, **401B**:308, 1997.

[17] C.Bernard *et al.* (MILC Collaboration). hep-lat/9707008.

[18] S. Perantonis and C. Michael. *Nucl. Phys.*, **B347**:854, 1990.

[19] K. Juge, J. Kuti, and C.J. Morningstar. hep-lat/9709131.

[20] T. Manke *et al.* (UKQCD Collaboration). hep-lat/9709001.

[21] C.J. Morningstar and M. Peardon. hep-lat/9704011.

[22] G.S. Bali *et al. Phys. Lett.*, **309B**:378, 1993.

[23] J.Sexton *et al.* (IBM Collaboration). *Phys. Rev. Lett.*, **75**:4563, 1995.

[24] G. Bali *et al.* (SESAM Collaboration). hep-lat/9710012.

[25] K.J. Juge, J. Kuti, and C.J. Morningstar. hep-lat/9709132.

[26] K.J. Juge, J. Kuti, and C.J. Morningstar. hep-lat/9809098.

[27] T.J. Allen, M.G. Olsson, and S. Veseli. hep-ph/9804452.

[28] E.S. Swanson and A.P. Szczepaniak. to appear in *Phys. Rev.* D.

[29] M. Tanimoto. *Phys. Lett.*, **116B**:198, 1982.

[30] A. Le Yaouanc, L. Oliver, O. Pene, J.-C. Raynal, and S. Ono. *Z. Phys.*, C **28**:309, 1985.

[31] F. Iddir, A. Le Yaouanc, L. Oliver, O. Pene, and J.-C. Raynal. *Phys. Lett.*, **207B**:325, 1988.

[32] N. Isgur, R. Kokoski, and J. Paton. *Phys. Rev. Lett.*, **54**:869, 1985.

[33] F.E. Close and P. Page. *Nucl. Phys.*, **B443**:233, 1995.

[34] E.S. Swanson and A.P. Szczepaniak. Decays of hybrid mesons. *Phys. Rev.*, D**56**:5692, 1997.

[35] P. Page, E.S. Swanson, and A.P. Szczepaniak. to appear in *Phys. Rev.* D.

[36] H.G.Dosch and D.Gromes. *Phys. Rev.*, D**33**:1378, 1986.

[37] S.Godfrey and N.Isgur. *Phys. Rev.*, D**32**:189, 1985.

[38] F. Iachello, N.C. Mukhopadhyay, and L. Zhang. Spectrum generating algebra for string-like hadrons: mass formula for mesons. *Phys. Lett.*, **256B**:"295–300", 1991.

[39] F. Iachello, Nimai C. Mukhopadhyay, and L. Zhang. Spectrum generating algebra for string-like mesons. 1. mass formula for $q\bar{q}$ mesons. *Phys. Rev.*, D **44**:"898–914", 1991.

[40] H.G.Blundell and S.Godfrey. *Phys. Rev.*, Dbf 53:3700, 1996.

[41] H.G.Blundell, S.Godfrey, and B.Phelps. *Phys. Rev.*, D**53**:3712, 1996.

[42] C. Amsler *et al.* High-statistics study of $f_0(1500)$ decay into $\pi^0\pi^0$. *Phys. Lett.*, **342B**:433–439, 1995.

[43] C. Amsler et al. Coupled channel analysis of $\bar{p}p$ annihilation into $\pi^0\pi^0\pi^0$, $\pi^0\eta\eta$, and $\pi^0\pi^0\eta$. *Phys. Lett.*, **355B**:425–432, 1995.

[44] P.Lacock *et al.* (UKQCD Collaboration). hep-lat/9611011.

[45] Carl E. Carlson and Nimai C. Mukhopadhyay. Perturbative QCD signatures of hybrid hadrons in electroproduction at high $q**2$. *Phys. Rev. Lett.*, **67** :"3745–3748", 1991.

[46] J.Weinstein and N.Isgur. *Phys. Rev.*, D**27**:588, 1983.

[47] J.Weinstein and N.Isgur. *Phys. Rev.*, D**41**:2236, 1990.

[48] N.N.Achasov and V.Ivanchenko. *Nucl. Phys.*, **B315**:465, 1989.

[49] F.E. Close, N. Isgur, and S. Kumano. Scalar mesons in ϕ radiative decay: Their implications for spectroscopy and studies of CP violation at ϕ factories. *Nucl. Phys.*, **B389**:513, 1993.

[50] V.Ivanchenko *et al.* hep-ex/9710017 and contribution to HADRON97.

[51] H.G.Blundell and S.Godfrey. *Phys. Rev.*, D**53**:3700, 1996.

[52] T.Barnes and N.Black. in preparation.

[53] D.Aston *et al. Phys. Lett.*, **215B**:199, 1988.

[54] A.Abele *et al.* (Crystal Barrel Collaboration). High-mass ρ-meson states from $\bar{p}d$-annihilation at rest into $\pi^-\pi^o\pi^o p_{\rm spectator}$. contribution to HADRON97.

[55] U.Thoma *et al.* (Crystal Barrel Collaboration). contribution to HADRON97.

[56] D.Weingarten. *Nucl. Phys.*, **B** (Proc. Suppl.) **34**:29, 1994.

[57] C.Michael. Liverpool report LTH 370, hep-ph/9605243 (May 1996).

[58] F.E.Close and M.J.Teper. On the lightest scalar glueball. RAL-96-040 / OUTP-96-35P (July 1996).

[59] C.Amsler and F.E.Close. *Phys. Lett.*, **353B**:385, 1995.

[60] C.Amsler and F.E.Close. *Phys. Rev.*, D**53**:295, 1996.

[61] J.Adomeit *et al.* (Crystal Barrel Collaboration). *Z. Phys.*, C **71**:227, 1996.

[62] K. L. Au, D. Morgan, and M. R. Pennington. Meson dynamics beyond the quark model: Study of final-state interactions. *Phys. Rev.*, D**35**:"1633–1664", 1987.

[63] F.E.Close, G.R.Farrar, and Z.Li. *Phys. Rev.*, D**55**:5749, 1997.

[64] R.Kaminski, L.Lesniak, and K.Rybicki. *Z. Phys.*, C**74**:79, 1997.

[65] J.A.Oller and E.Oset. *Nucl. Phys.*, **A620**:438, 1997.

[66] N.A.Tornqvist and M.Roos. *Phys. Rev. Lett.*, **76**:1575, 1997.

[67] G. Janssen, B.C. Pearce, K. Holinde, and J. Speth. *Phys. Rev.*, D**52**:2690, 1995.

[68] J.A. Oller, E. Oset, and J.R. Pelaez. *Phys. Rev. Lett.*, **80**:3452, 1998.

[69] W.W. Weitzel *et al. Nucl. Phys.*, **B115**:208, 1976.

[70] A. Dzierba. Photoproduction opportunities at cebaf: Meson spectroscopy and the physics of flying phi's. In N. Isgur and P. Stoler, editors, *Proceedings of the Workshop on CEBAF at Higher Energies*, page 13, 1994.

[71] A. Dzierba. Measuring rare radiative decays of the phi at cebaf. In R. Baldini, editor, *Workshop on Physics and Detectors for DAPHNE*, page 99, 1995.

[72] A. Dzierba. Scalar mesons and rare radiative decays of the phi. *Nucl. Phys.*, **A623**:142c, 1997. Proceedings on the First Workshop on Hadron Dynamics, Frascati.

[73] D.C. Fries *et al.* S-p wave interference in k^+k^- production near threshold. *Nucl. Phys.*, **B143**:408, 1978.

[74] D.P.Barber *et al.* A study of elastic photoproduciton of low mass k^+k^- pairs. *Z. Phys.*, **C12**:1, 1982.

[75] J.Lee-Franzini, W.Kim, and P.J.Franzini. *Phys. Lett.*, **287B**:259, 1992.

[76] E.P. Solodov (CMD-2 Collaboration.). In S.-U. Chung and H.J. Willutzki, editors, *7th International Conference on Hadron Spectroscopy, Hadron'97'*. AIP, 1998.

[77] M. Burkardt *et al.*, editor. *International Workshop on the Structure of the Eta' Meson*. World Scientific, 1996.

[78] J. Bijnens, A. Bramon, and F. Cornet. *Phys. Lett.*, **237B**:488, 1990.

[79] G.D'Ambrosio, G. Ecker, G. Isidori, and H. Neufeld. In *The Second DAΦNE Physics Handbook*.

[80] See, for example, R.G. Sachs, The Physics of Time Reversal (University of Chicago Press, Chicago, 1987).

[81] See, for example, R.M. Barnett et al., Review of Particle Properties, *Phys.Rev.* D **54**, 1 (1996).

[82] B. Schwingenheuer *et al. Phys. Rev. Lett.*, **74**:4376, 1995.

[83] V.A. Kostelecky and R. Potting. *Nucl. Phys.*, **B359**:545, 1991.

[84] V.A. Kostelecky and R. Potting. *Phys. Lett.*, **381B**:89, 1996.

[85] V.A. Kostelecky and S. Samuel. *Phys. Rev. Lett.*, **63**:224, 1989.

[86] V.A. Kostelecky and S. Samuel. *Phys. Rev. Lett.*, **66**:1811, 1991.

[87] V.A. Kostelecky and S. Samuel. *Phys. Rev.*, D**39**:683, 1989.

[88] V.A. Kostelecky and S. Samuel. *Phys. Rev.*, D**40**:1886, 1989.

[89] V.A. Kostelecky and R. Potting. *Phys. Rev.*, D **51**:3923, 1995. also in D.B. Cline, ed., Gamma Ray–Neutrino Cosmology and Planck Scale Physics (World Scientific, Singapore, 1993) (hepth/9211116).

[90] V.A. Kostelecky. *Phys. Rev. Lett.*, **80**:1818, 1998.

[91] N. Isgur, V.A. Kostelecky, and A.P. Szczepaniak. in preparation.

[92] T. Barnes. In *Physics with 8+ GeV Photons Workshop*. Workshop in Bloomington IN, July 14-16 1997, proceedings available from Jefferson lab.

[93] K. Schilling, P. Seyboth, and G. Wolf. On the analysis of vector meson production. *Nucl. Phys.*, **B15**:398, 1970.

[94] P. R. Page A. Afanasev. Photoproduction and electroproduction of $j^{PC} = 1^{-+}$ exotics. *Phys. Rev.*, D **57**:6771, 1998.

[95] A. Afanasev and A.P. Szczepaniak. in preparation.

[96] G.S. Adams *et al. Phys. Rev. Lett.*, **81**:5760, 1998.

[97] C. Keppel. Development of a Compton-backscattered photon source for Hall B at Jefferson Lab. In *Physics with 8+ GeV Photons Workshop*. Workshop in Bloomington IN, July 14-16 1997, proceedings available from Jefferson lab.

[98] W. Kaune, G. Miller, W. Oliver, R.W. Williams, and K.K. Young. Inclusive cross sections for pion and proton production by photons using collimated coherent bremsstrahlung. *Phys. Rev.*, D **11**(3):478–494.

[99] H. Bilokon, G. Bologna, F. Celani, B. D'Ettorre Piazzoli, R. Falcioni, G. Mannocchi, and P. Picchi. Coherent bremsstrahlung in crystals as a tool for producing high energy photon beams to be used in photoproduction experiments at CERN SPS. *Nuclear Inst. and Meth.*, **204**:299–310.

[100] D. Aston *et al.* The lass spectrometer. Technical report, 1987. SLAC-Report-298 Copies available from the SLAC publications office, at http://www.slac.stanford.edu/pubs/.

[101] J. S. Alcorn, H.O. Peterson, and S. St. Lorent. In *Applied Superconductivity Conference - 1972*, page 273.

[102] D.W. Hertzog *et al. Nuclear Inst. and Meth.*, **A294**:446, 1990.

[103] K.F. Johnson *et al. Nuclear Inst. and Meth.*, **A317**:506, 1992.

[104] A. Antonelli *et al. Nuclear Inst. and Meth.*, **A370**:367, 1996.

[105] A. Antonelli *et al. Nuclear Inst. and Meth.*, **A354**:352, 1995.

[106] T. Bienz. PhD thesis, Stanford University, 1990. SLAC Report 369.

[107] P. Rensing. PhD thesis, Stanford University, 1993. SLAC Report 421.

[108] *et al.* D.P. Barber. *Z. Phys.*, **C4**:169, 1980.

[109] M. Moszynski and B. Bengston. *Nuclear Inst. and Meth.*, **158**:1, 1979.

[110] B. Bengston and M. Moszynksi. *Nuclear Inst. and Meth.*, **204**:129, 1982.

[111] E. Chen, M. Saulnier, W. Sun, and H. Yamamoto. Tests of a high resolution time-of-flight system based on long and narrow scintillator. hep-ex/9606007.

[112] E. Cisbani *et al.* Proposal for a dual radiator rich for hermes. available through the HERMES home page at http://dxhra1.desy.de/.

[113] *et al.* G.B̃raun. Tdc chip and readout driver developments for compass and lhc-experiments. hep-ex/9810048.

[114] D. von Harrach. *Nucl. Phys.*, **A629**:245c, 1998.

[115] M. Hauschild. Progress in de/dx techniques used for particle identification. *Nuclear Inst. and Meth.*, **A379**:436, 1996.

[116] *et al.* A. Andryakov. de/dx measurement in a he-based gas mixture. *Nuclear Inst. and Meth.*, **A409**:390, 1998.

[117] B.B. Brabson *et al. Nuclear Inst. and Meth.*, **A332**:419–443, 1993.

[118] A. Brunner *et al. Nuclear Inst. and Meth.*, **A414**:466–476, 1998.

[119] R. R. Crittenden *et al. Nuclear Inst. and Meth.*, **387**:377, 1998.

[120] S. Teige. In Howard A. Gordon and Doris Rueger, editors, *Proceedings of the Fifth International Conference on Calorimetry in High Energy Physics*, pages 161–166. World Scientific, 1995.

[121] Armstrong *et al. Phys. Rev.*, D**5**:1640, 1972.

[122] Caldwell *et al. Phys. Rev.*, D**7**:1362, 1973.

[123] The Durham online database is located on the WWW at http://durpdg.dur.ac.uk/HEPDATA.

[124] Caso *et al.* (Particle Data Group). *Eur.Phys.*, **J3**:1, 1998.

[125] P. Eugenio. *Genr8*: A general monte carlo event generator. Carnegie Mellon University, 1998.

[126] S. Teige. A monte-carlo user guide. Indiana University, 1998.

[127] Information on MCFast may be optained via the WWW at http://fnpspa.fnal.gov.

[128] Information on ROOT may be optained via the WWW at http://root.cern.ch.

[129] ABBHHM Collaboration. *Phys. Rev.*, **175**:1669, 1968.

[130] G. Condo *et al. Phys. Rev.*, D**41**:3317, 1990.

[131] G. Condo *et al. Phys. Rev.*, D**48**:3045, 1993.

[132] J. Ballam *et al.* Bubble-chamber study of photoproduction by polarized photons. *Phys. Rev.*, D**6**:454, 1972.

[133] J. Ballam *et al.* Conservation of s-channel helicity conservation in ρ photoproduction. *Phys. Rev. Lett.*, **24**:960, 1970.

[134] J. Ballam *et al.* Vector-meson production by polarized photons from 2.8, 4.7, and 9.3 gev. *Phys. Rev.*, D**7**:"3150–3177", 1973.

[135] J. Ballam *et al. Phys. Rev.*, D**5**:"545–589", 1972.

[136] J. Ballam *et al.* Study of $\gamma p \to p\omega$ with linearly polarized photons. *Phys. Rev. Lett.*, **24**:1364, 1970.

[137] J. Ballam *et al.* A search for B and $\rho^-(1250)$ production in the reaction $\gamma p \to p\pi^+\pi^-+$ neutrals at 2.8, 4.7, and 9.3 gev. *Nucl. Phys.*, **B76**:"375–399", 1974.

[138] S.D. Drell. *Rev. Mod. Phys.*, **33**:459, 1961.

[139] P. Söding. *Phys. Lett.*, **19B**:702, 1965.

[140] M. Derrick *et al.* (ZEUS Collaboration). *Z. Phys.*, **C69**:39, 1995.

[141] S. Aid *et al* (H1 Collaboration). *Nucl. Phys.*, **B463**:3, 1996.

[142] M.G. Ryskin and Yu.M. Shabelski. hep-ph/9712437.

[143] J.P. Cummings and D.P. Weygand. Brookhaven National Laboratory Report BNL-64637.

[144] S.U. Chung. Spin formalisms. CERN Report 71-8, March 1971, Lectures given in the Academic Training Program of CERN 1969-1970.